The proton charge radius

H. Gao[*]

Department of Physics, Duke University and the Triangle Universities Nuclear Laboratory, Science Drive, Durham, North Carolina 27708, USA

M. Vanderhaeghen[†]

Institut für Kernphysik and PRISMA⁺ Cluster of Excellence, Johannes Gutenberg Universität, D-55099 Mainz, Germany

(published 21 January 2022)

Nucleons (protons and neutrons) are the building blocks of atomic nuclei and are responsible for more than 99% of the visible matter in the Universe. Despite decades of efforts in studying its internal structure, there are still a number of puzzles surrounding the proton such as its spin and charge radius. Accurate knowledge about the proton charge radius is not only essential for understanding how QCD works in the nonperturbative region but also important for bound state QED calculations of atomic energy levels. It also has an impact on the Rydberg constant, one of the most precisely measured fundamental constants in nature. This review examines the latest situation concerning the proton charge radius in light of the new experimental results from both atomic hydrogen spectroscopy and electron-scattering measurements, with particular focus on the latter. Theoretical backgrounds and recent developments concerning the determination of the proton charge radius using different experimental techniques are also presented. Upcoming experiments are discussed, and the deuteron charge radius puzzle is mentioned at the end.

CONTENTS

I. INTRODUCTION

Nucleons (protons and neutrons) are the building blocks of atomic nuclei and are responsible for more than 99% of the visible matter in the Universe. The force that is responsible for binding nucleons into nuclei (and responsible for the composite nature of nucleons) is the strong force, one of the four fundamental forces in nature. The ultimate goal of modern nuclear physics is to predict properties of nucleons, atomic nuclei, and nuclear reactions from the first principles of quantum chromodynamics (QCD), the theory of the strong interaction with quarks and gluons as the fundamental degrees of freedom. While QCD has been well tested experimentally at high energies, where perturbative calculations can be carried out, how QCD works in the low-energy region still requires a much better understanding. Nucleons therefore become important QCD laboratories through studies of their rich internal structure.

Despite decades of efforts studying the internal structure of the proton, there are still a number of puzzles and open questions surrounding the proton, such as its spin and charge radius. The so-called proton spin crisis was triggered by the European Muon Collaboration experiment (Ashman *et al.*,

*hgao@duke.edu
†vandma00@uni-mainz.de

1988) in which polarized muons were scattered off polarized nucleons, discovering that quarks' spins contribute little to the proton spin. After more than three decades of polarization experiments worldwide, the emerging picture about the proton spin is that the quark spin contributes about a third to the proton spin, with a comparable contribution likely from the spins of the gluons, and the remaining portion from the orbital angular momenta of the quarks and gluons inside. For a recent review of the proton spin, see Kuhn, Chen, and Leader (2009) and Ji, Yuan, and Zhao (2020).

The proton mass decomposition has been a topic of increasing interest in recent years motivated by the experimental capability offered by the energy upgraded 12-GeV CEBAF at Jefferson Lab (Dudek et al., 2012), and the future Electron-Ion Collider (EIC) (Accardi et al., 2016) to be built at the Brookhaven National Laboratory. There are various approaches to the proton mass decomposition (Shifman, Vainshtein, and Zakharov, 1978; Ji, 1995; Lorcé, 2018; Metz, Pasquini, and Rodini, 2020). Following Ji's decomposition, the quark mass contribution to the proton mass is found to be ∼11%, trace anomaly is about 22%, and the rest is due to the quark and gluon energy (Gao et al., 2015). Near-threshold electroproduction and photoproduction cross sections of J/Ψ and Υ particles (Kharzeev et al., 1999; Gryniuk and Vanderhaeghen, 2016; Hatta and Yang, 2018; Gryniuk et al., 2020) from the proton have been proposed as effective ways to access the trace anomaly contribution, and experiments (Hafidi et al., 2012; Gryniuk et al., 2020) are being planned at Jefferson Lab and at the future EIC.

The proton root-mean-square (rms) charge radius (also known as the proton charge radius) is a quantity that is of importance not only to QCD but also to bound state QED calculations of atomic energy levels. It additionally has a direct impact on the determination of the Rydberg constant, one of the most well-known fundamental quantities in nature. Conventionally, the proton charge radius can be determined from electron-proton elastic scattering, a method pioneered by Hofstadter, and atomic spectroscopic measurements using ordinary hydrogen atoms. In the former case, one determines the proton electric form factor from scattering cross sections, from which one then extracts the proton charge radius. In the latter case, experimentally measured atomic transitions combined with state-of-the-art QED calculations allow for an extraction of the proton charge radius.

The proton charge radius puzzle originated in 2010 following a new ultraprecise determination of the proton charge radius from muonic hydrogen Lamb shift measurements (Pohl et al., 2010), which reported a radius value of 0.841 84(67) fm. This new result is 4% smaller than the recommended value of 0.8775(51) fm given by the Committee on Data for Science and Technology (CODATA-2010) (Mohr, Taylor, and Newell, 2012) based on results from electron-proton scattering and ordinary hydrogen spectroscopy measurements and represents a 7σ difference. In the last ten years, major progress has been made in resolving this puzzle, which is the focus of this review. While we cover the latest progress in atomic spectroscopy concerning the proton charge radius, special emphasis will be placed in this review on the progress from lepton scattering and its associated challenges. The rest of the review is organized as follows. We set the stage and

introduce the proton charge radius puzzle in Sec. II. In Sec. III we describe how the charge radius is defined, how it can be properly understood in terms of a quark charge distribution, and how it is connected to the quark structure of the proton. We subsequently describe the experimental techniques in determining the proton charge radius from elastic electron-proton scattering in Sec. III and from atomic hydrogen spectroscopy in Sec. IV. Sections V and VI review the results from the recent lepton-scattering and spectroscopy measurements, respectively. In Sec. VII we review ongoing and planned lepton-scattering experiments. Section VIII provides an introduction of another charge radius puzzle that concerns the deuteron before we conclude in Sec. IX.

II. THE PROTON CHARGE RADIUS PUZZLE

The proton charge radius puzzle developed and quickly became widely known in 2010 when the CREMA Collaboration (Pohl et al., 2010) reported the first determination of the proton charge radius from a muonic hydrogen spectroscopic method ever, giving a value of 0.841 84(67) fm by measuring the transition between the $2S_{1/2}(F = 1)$ and $2P_{3/2}(F = 2)$ energy levels. It was the most precise measurement at the time, but it was 7σ smaller than the 2010 CODATA recommended value of 0.8775(51) fm (Mohr, Taylor, and Newell, 2012). In 2013, the CREMA Collaboration reported (Antognini et al., 2013) a value of 0.840 87(39) fm from combined analyses of the original transition they reported in 2010 together with a different transition between the $2S_{1/2}(F = 0)$ and $2P_{3/2}(F = 1)$ levels. See Pohl et al. (2013) and Carlson (2015) for some early reviews. From the electron-scattering community, two values of the proton charge radius were reported at around the same time, and they are 0.8791(79) fm by Bernauer et al. (2010) and 0.875 (10) fm by Zhan et al. (2011):both were included in the 2010 CODATA compilation and are in excellent agreement with its recommended value. The muonic hydrogen results (Pohl et al., 2010; Antognini et al., 2013) were not included in the CODATA compilation until its most recent release (Tiesinga et al., 2021).

The release of the proton charge radius result from a muonic hydrogen spectroscopic measurement by the CREMA Collaboration in 2010 (Pohl et al., 2010) resulted in a major proton charge radius puzzle. However, there was a puzzle even before that, perhaps known only to a much smaller community. An important motivation to improve the precision in determining the proton charge radius from electron-scattering experiments is for precision tests of QED through hydrogen Lamb shift measurements. The standard hydrogen Lamb shift measurement probes the 1057 MHz fine-structure transition between the $2S_{1/2}$ and $2P_{1/2}$ states and can be calculated to high precision with higher-order corrections in QED with the proton rms charge radius as an important input for finite size and other hadronic structure contributions. However, the two most precise values from electron-scattering experiments in the literature before 2010 [each with a relative uncertainty of less than 1.5% but differing by about 7% (relative)] are $r_p = 0.805(11)$ fm (Hand, Miller, and Wilson, 1963) and $r_p = 0.862(12)$ fm (Simon et al., 1980). The result of Hand, Miller,

and Wilson (1963) included data from several experiments. In the late 1990s, several groups published high-precision results from hydrogen spectroscopic measurements (Hagley and Pipkin, 1994; Weitz et al., 1994; Berkeland, Hinds, and Boshier, 1995; Bourzeix et al., 1996; van Wijngaarden, Holuj, and Drake, 1998), and these results supported a larger value of the proton charge radius (0.862 fm) than QED predictions including the two-loop binding effects. Melnikov and van Ritbergen (2000) calculated the three-loop slope of the Dirac form factor (the last known contribution to the hydrogen energy levels at order $m\alpha^7$) and extracted a proton charge radius value of 0.883(14) fm combining the QED calculation of the $1S$ Lamb shift and the experimental measurement (Schwob et al., 1999).

III. ELASTIC ELECTRON-PROTON SCATTERING

Electron scattering has proved to be an effective and clean way to probe the internal structure of the nucleon (as the lepton vertex is well described by QED) and higher-order contributions are suppressed relative to the leading-order, one-photon-exchange contribution. This was demonstrated by the Nobel Prize–winning electron-proton elastic-scattering experiment carried out by Hofstadter and McAllister (1955) and McAllister and Hofstadter (1956) in the 1950s at Stanford University (), in which the root-mean-squared charge radius of the proton -0.74 ± 0.24 fm was determined for the first time. The success of lepton scattering was further demonstrated by another Nobel Prize awarded to Friedman, Kendall, and Taylor (Bloom et al., 1969; Breidenbach et al., 1969) for leading the deep-inelastic-scattering experiments with electron beams at SLAC between 1967 to 1973, which discovered for the first time the existence of pointlike particles (quarks inside the proton). For details on the discovery of quarks, see Riordan (1992).

A. Introduction to electron-proton scattering and proton electromagnetic form factors

To lowest order in QED, the dominant contribution to the electron-proton elastic scattering is the one-photon-exchange (OPE) Feynman diagram, as shown in Fig. 1. The four-momentum of the incoming (scattering) electron is labeled k (k'). The four-momentum of the target (recoil) proton is labeled by p (p'). A virtual photon exchanged between the
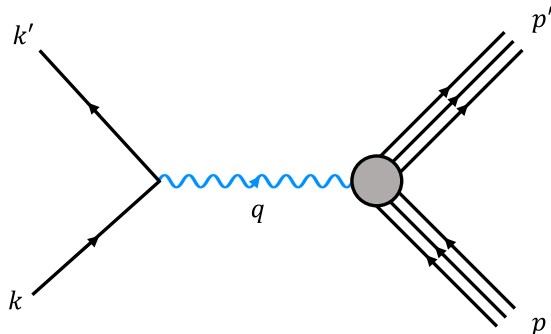

FIG. 1. One-photon-exchange diagram describing the elastic electron-proton scattering. From Jingyi Zhou.

electron and the proton carries a four-momentum q and the corresponding momentum transfer squared q^2 is a Lorentz invariant. In electron scattering, the opposite of the four-momentum transfer squared Q^2 ($Q^2 = -q^2 \geq 0$) is commonly used.

The scattering amplitude for the elastic electron scattering from a hadronic target in OPE based on QED can be written as

$$\mathcal{M} = i\frac{e^2}{Q^2} u(k', h)\gamma_\mu u(k, h)\langle p', \lambda'|J^\mu_{\text{em}}(0)|p, \lambda\rangle, \quad (1)$$

in which u denotes the electron Dirac spinors, with h the conserved helicity of the electrons, λ (λ') denotes the helicity of the initial (final) hadrons, and $\langle p', \lambda'|J^\mu_{\text{em}}(0)|p, \lambda\rangle$ is the hadron matrix element of the local electromagnetic current operator (taken at space-time point $x = 0$).

For a spin-$1/2$ extended object such as a nucleon, its electromagnetic transition current (following the requirements of current and parity conservation and covariance under the improper Lorentz group) can be written as

$$\langle p', \lambda'|J^\mu_{\text{em}}(0)|p, \lambda\rangle = \bar{N}(p', \lambda')\Gamma^\mu N(p, \lambda), \quad (2)$$

in which N denote the nucleon spinors and Γ^μ is the following virtual photon-proton vertex:

$$\Gamma^\mu \equiv F_1(q^2)\gamma^\mu + F_2(q^2)\frac{i\sigma^{\mu\nu}q_\nu}{2M}. \quad (3)$$

The functions F_1 and F_2, two independent quantities that depend on $q^2(Q^2)$ only, are called the Dirac and Pauli form factors (FFs), respectively, and M is the mass of the nucleon.

The electric (G_E) and magnetic (G_M) form factors of the nucleon, also called the Sachs form factors, are two independent linear combinations of F_1 and F_2 that were originally proposed by Ernst, Sachs, and Wali (1960) as

$$G_E = F_1 - \frac{Q^2}{4M^2}F_2, \quad (4)$$

$$G_M = F_1 + F_2. \quad (5)$$

In the limit of $Q^2 = 0$, $G_{Ep}(0) = 1$, $G_{En}(0) = 0$, which are simply the charges of the proton and neutron respectively, while $G_{Mp}(0) = \mu_p$, $G_{Mn}(0) = \mu_n$ are the proton and neutron magnetic moments, respectively. The Pauli FF at $Q^2 = 0$ is given by the anomalous magnetic moment $F_2(0) \equiv \kappa$, with $\mu_p = 1 + \kappa_p$ and $\mu_n = \kappa_n$. In comparison to the F_1 and F_2 form factors, G_E and G_M were proposed to have a more intuitive physical interpretation, although $G_E(0) = F_1(0)$. Sachs (1962) showed that in the Breit frame G_E and G_M can be interpreted as Fourier transforms of spatial distributions of charge and magnetization when the nucleon is treated as a nonrelativistic static system. In the Breit frame the incoming electron has a momentum of $\vec{q}/2$ and the nucleon initial momentum is $-\vec{q}/2$; the scattered electron has a momentum of $-\vec{q}/2$ and the recoil proton has a momentum of $\vec{q}/2$. Thus, it is a special Lorentz frame in which $q^2 = -\vec{q}^2$; i.e., no energy transfer is involved in this particular reference frame. For each

Q^2 value, there is the corresponding Breit frame, in which the form factors are represented as $G_{E,M}(q^2) = G_{E,M}(-\vec{q}^2)$. For nonrelativistic (n-rel) static systems, the analogy to a "classical" charge density distribution has then been introduced in the literature as follows through the three-dimensional (3D) Fourier transformation of the matrix element of the charge operator in the Breit (B) frame:

$$\rho_{3D,\text{n-rel}}(r) = \int \frac{d^3\vec{q}}{(2\pi)^3} e^{-i\vec{q}\cdot\vec{r}} \frac{\langle p', \lambda | J_{\text{em}}^0(0) | p, \lambda \rangle_B}{2M}$$
$$= \int \frac{d^3\vec{q}}{(2\pi)^3} e^{-i\vec{q}\cdot\vec{r}} G_E(-\vec{q}^2), \quad (6)$$

which depends on $r = |\vec{r}|$ only for a spherical symmetric system.

Lorcé (2020) pointed out that for a relativistic (rel) system a proper kinematical factor has to be introduced, leading to the following modified quantity:

$$\rho_{3D,\text{rel}}(r) = \int \frac{d^3\vec{q}}{(2\pi)^3} e^{-i\vec{q}\cdot\vec{r}} \frac{\langle p', \lambda | J_{\text{em}}^0(0) | p, \lambda \rangle_B}{2P_B^0}$$
$$= \int \frac{d^3\vec{q}}{(2\pi)^3} e^{-i\vec{q}\cdot\vec{r}} \frac{1}{\sqrt{1 + \vec{q}^2/4M^2}} G_E(-\vec{q}^2), \quad (7)$$

where P_B^0 is the nucleon energy in the Breit frame. It was furthermore argued by Lorcé (2020) from a phase-space perspective that the quantity $\rho_{3D,\text{rel}}(r)$ can be interpreted as an internal charge quasidensity of the target. One notices that such relativistic quasidensity is obtained by the Fourier transform of $G_E(q^2)$ multiplied by the relativistic factor $M/P_B^0 = 1/\sqrt{1 + Q^2/4M^2}$, as $Q^2 \equiv -q^2 = \vec{q}^2$ in the Breit frame.

To arrive at a strict density or probabilistic interpretation, the momentum transfer is required to remain small relative to the inertia of the system. The concept of a rest-frame density is therefore intrinsically limited by the Compton wavelength of the system. This limitation can, however, be avoided in the infinite-momentum frame (IMF), in which the magnitude of the nucleon's momentum $|\mathbf{p}| \gg M$; i.e., the nucleon is moving at infinite momentum. The IMF is advantageous in discussing the deep-inelastic-scattering process in which the virtual photon interacts with a parton (quark) inside the nucleon. In the IMF due to relativistic time dilation, the struck quark is essentially free from interacting with other partons inside the nucleon during the short time that the quark interacts with the virtual photon. Rinehimer, Jared and Miller (2009) studied the connection between the Breit frame and the IMF and showed that when the nucleon matrix element of the time component of the electromagnetic current, which gives $G_E/\sqrt{1 + Q^2/4M^2}$ in the Breit frame as previously discussed, is boosted to the IMF, one obtains the F_1 form factor. This was confirmed by the analysis of Lorcé (2020), as well as the earlier work of Chung et al. (1988).

Miller (2019) pointed out that the previously mentioned picture connecting the proton charge density distribution to the Fourier transform of the G_E form factor is not correct and showed that a three-dimensional charge density, in the strict sense of a probability interpretation, cannot be defined for a nucleon (as a relativistic system of quarks and gluons) because the initial- and final-state proton wave functions are not the same. Instead, a two-dimensional charge density can be defined, and determined by the Dirac form factor F_1, as a matrix element of a density operator between identical initial and final states that are localized in the plane transverse to the direction of the fast-moving nucleons.

Jaffe (2021) looked at this issue from a fundamental aspect (the interplay between relativity and the uncertainty principle) and pointed out that any attempt to extract spatial distributions of local properties of a hadronic system that is not much larger than its Compton wavelength would fail. In the case of the proton, its Compton wavelength is about 0.2 fm, which is not significantly smaller than its size of ~ 0.85 fm. Defining the expectation value of the spatial charge density distribution of the proton requires one to localize the proton, which introduces a localization dependence into the relationship between the form factor and the local charge density distribution. Only for systems such as atoms and heavy atomic nuclei (for which the intrinsic sizes of the systems are much larger than the corresponding Compton wavelength) is the connection between the three-dimensional Fourier transform of the charge form factor and the local charge density distribution meaningful. Belitsky, Ji, and Yuan (2004) discussed the proton form factors and charge distributions in their seminal paper on the development of the concept of quantum phase-space Wigner distributions for quarks and gluons in the proton.

In the last two or more decades, there have been major developments in three-dimensional imaging of the partonic structure of the nucleon, motivated to a large extent by the desire to solve the "proton spin crisis" or "puzzle." These developments also shed new light on the electromagnetic structure of the nucleon. It is important to discuss the proton charge distribution and electric and magnetic form factors in the context of these new developments. In Sec. III.B, we introduce the three-dimensional parton distributions before discussing the two-dimensional charge density.

B. Three-dimensional parton distributions

The general framework to describe the partonic structure of the proton is through the generalized transverse-momentum-dependent parton distributions (GTMDs) (Meissner, Metz, and Schlegel, 2009; Lorcé, Pasquini, and Vanderhaeghen, 2011), which are obtained by integrating the fully unintegrated generalized quark-quark correlation functions for a nucleon in momentum space over the light-cone energy component of the quark momentum (Meissner et al., 2008; Meissner, Metz, and Schlegel, 2009). The thus obtained GTMDs depend on x, $\mathbf{k}_\perp$, and Δ, where x is the longitudinal momentum fraction of the parton $\mathbf{k}_\perp$, the transverse momentum of the parton, and Δ is the four-momentum transfer to the nucleon. The GTMDs are related to the Wigner distributions (Ji, 2003; Belitsky, Ji, and Yuan, 2004; Lorcé and Pasquini, 2011) via a Fourier transformation between the transverse-momentum transfer $\mathbf{\Delta}_\perp$ and the quark's transverse position $\mathbf{b}$. The five-dimensional Wigner distributions $\rho(\mathbf{b}, \mathbf{k}_\perp, x, \vec{S})$ (Lorcé et al., 2012) for a nucleon with polarization $\vec{S}$ are
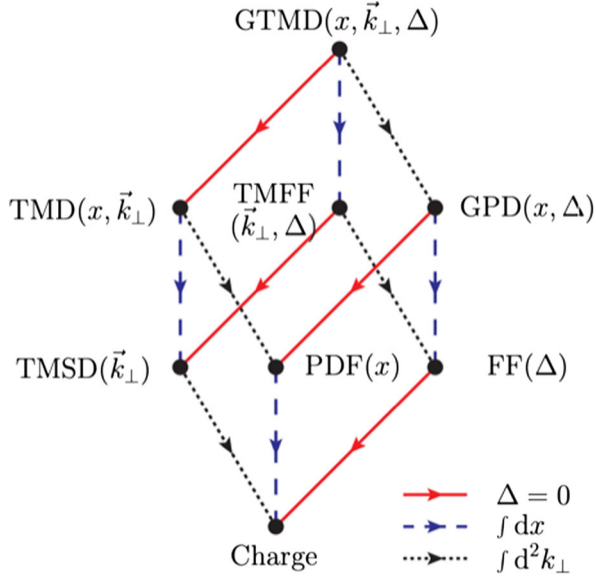
FIG. 2. Parton distribution family. From Lorcé, Pasquini, and Vanderhaeghen, 2011.

the quantum mechanical analogs of the classical phase-space distributions, with the five dimensions being x, $\mathbf{k}_\perp$, and the transverse coordinates $\mathbf{b}$.

As illustrated in Fig. 2, one can obtain the generalized parton distributions (GPDs) by integrating the GTMDs over the transverse momentum $\mathbf{k}_\perp$. The GPDs can be viewed as the generalization of the parton distribution functions (PDFs) and the form factors. On the other hand, one can obtain the transverse-momentum-dependent parton distributions (TMDs) by setting the momentum transfer Δ to zero or, equivalently, by integrating the Wigner distributions over the transverse coordinate $\mathbf{b}$. The TMDs will reduce to PDFs when the transverse momentum is integrated. In Fig. 2, TMFF and TMSD refer to transverse-momentum-dependent form factors and transverse-momentum-dependent spin densities, respectively. While the most general one-parton information is contained in the GTMDs, which are connected to the Wigner distributions through Fourier transformations, neither the GTMDs nor the Wigner distributions are measurable in experiments. However, there are ways to access GPDs, which we discuss next, and TMDs experimentally. For TMDs, we refer the interested reader to a recent review by Anselmino, Mukherjee, and Vossen (2020).

In 1997, deeply virtual Compton scattering (DVCS) (Ji, 1997a) was proposed as an experimental tool to probe GPDs. See Müller et al. (1994), Radyushkin (1996), and Ji (1997a, 1997b) for the original articles on GPDs and Goeke, Polyakov, and Vanderhaeghen (2001), Diehl (2003a), Belitsky and Radyushkin (2005), Boffi and Pasquini (2007), Guidal, Moutarde, and Vanderhaeghen (2013), and Kumericki, Liuti, and Moutarde (2016) for reviews of the field. In the Björken limit, the DVCS amplitude is described through the following four off-forward parton distributions (Ji, 1997a): H^q and $\tilde{H}^q$ (which conserve the nucleon helicity) for a quark of flavor q and E^q and $\tilde{E}^q$, which flip the nucleon helicity. These GPDs are functions of x, ξ, and Δ^2 [for example, $H^q(x, \xi, \Delta^2)$ and $E^q(x, \xi, \Delta^2)$], where x is the average fraction of quark

longitudinal momentum, ξ is the average fraction of the longitudinal momentum transfer Δ, and Δ^2 is the squared momentum transfer.

In the forward limit $\Delta^\mu \to 0$, H and $\tilde{H}$ are simply the quark momentum and helicity PDFs:

$$H^q(x, 0, 0) = q(x), \qquad \tilde{H}^q(x, 0, 0) = \Delta q(x). \qquad (8)$$

Furthermore, one can write the following sum rules relating these new distributions to the quark flavor components of the Dirac and Pauli form factors in a nucleon as

$$F_1^q(\Delta^2) = \int_{-1}^{+1} dx H^q(x, \xi, \Delta^2), \qquad (9)$$

$$F_2^q(\Delta^2) = \int_{-1}^{+1} dx E^q(x, \xi, \Delta^2), \qquad (10)$$

where the ξ independence of these sum rules is a consequence of Lorentz invariance.

C. The nucleon transverse charge densities

We next discuss in more detail how to define a charge density in a nucleon, and how such density is related to the previously discussed elastic form factors and generalized parton distributions. For relativistic quantum systems, such as hadrons composed of nearly massless quarks, a proper definition of a charge density requires care, as previously discussed. For such systems, the number of constituents is not constant, as a result of virtual pair production. Consider as an example a hadron such as the proton, which is probed by a spacelike virtual photon, as shown in Fig. 3. A sizable fraction of the proton's response when it is probed by a virtual photon with small (or even intermediate) virtuality comes from wave function components beyond the three valence quark state state (Sufian et al., 2017). In such a system, the wave function contains, besides the three valence quark Fock component $|qqq\rangle$, components where additional $q\bar{q}$ pairs, so-called sea quarks, or transverse gluons g are excited, leading to an infinite tower of $|qqqq\bar{q}\rangle, |qqqg\rangle, \dots$ components. When one

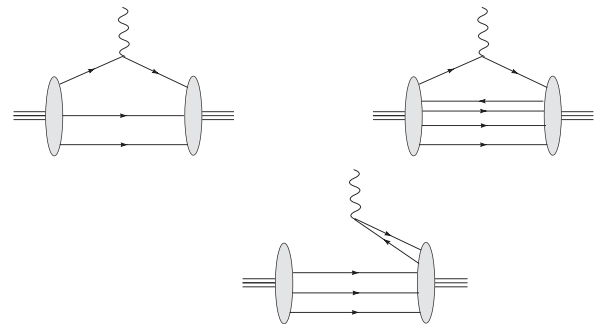FIG. 3. Coupling of a spacelike virtual photon to a relativistic many-body system such as a proton. Upper images: diagonal transition where the photon couples to a quark in the leading $3q$ Fock component (left image) or in a higher $5q$ Fock component (right image). Lower image: process where the photon creates a $q\bar{q}$ pair leading to a nondiagonal transition between an initial $3q$ state and a final $5q$ state in the proton.

probes such a system using electron scattering, the exchanged virtual photon will couple to any quark or antiquark in the proton, as shown in Fig. 3 (upper images). In addition, the virtual photon can produce a $q\bar{q}$ pair, giving rise to a transition from a $3q$ state in the initial wave function to a $5q$ state in the final wave function, as shown in Fig. 3 (lower image). Such processes, leading to nondiagonal overlaps between initial and final wave functions, are not positive definite and no longer allow for a simple probability interpretation of the density ρ. Only the processes shown in the upper images of Fig. 3 with the same initial and final wave function yield a positive definite particle density, allowing for a probability interpretation.

This relativistic dynamical effect of pair creation or annihilation fundamentally hampers the interpretation of density and any discussion of the size and shape of a relativistic quantum system. An interpretation in terms of the concept of a density requires one to suppress the contributions shown in the lower image of Fig. 3. This is possible when viewing the hadron from a light-front frame, which allows one to describe the hadron state using an infinite tower of light-front wave functions. Consider the electromagnetic (e.m.) transition from an initial hadron (with four-momentum p) to a final hadron (with four-momentum p') when viewed from a light-front moving toward the hadron. Equivalently, this corresponds with an IMF where the hadrons have a large momentum component along the z axis chosen along the direction of the hadrons' average momentum $P = (p + p')/2$. One then defines the light-front plus component as $P^+ \equiv (P^0 + P^3)/\sqrt{2}$, which is always a positive quantity for the quark or antiquark four-momenta in the hadron. When one views the hadron in a so-called Drell-Yan frame (Drell and Yan, 1970), where the virtual photon four-momentum $\Delta = p' - p$ is purely transverse, satisfying $\Delta^+ = 0$, energy-momentum conservation will forbid processes where this virtual photon splits into a $q\bar{q}$ pair. Such a choice is possible for a spacelike virtual photon, and its virtuality is then given by $t \equiv \Delta^2 = -\mathbf{\Delta}_\perp^2 < 0$, where $\mathbf{\Delta}_\perp$ is the transverse photon momentum, lying in the transverse spatial (x, y) plane. Here $-t$ or $\mathbf{\Delta}_\perp^2$ is the same as the virtuality Q^2 in elastic e-p scattering. In such a frame, the virtual photon couples only to forward-moving partons; i.e., only processes such as those shown in the upper part of Fig. 3 are allowed. We can then define a proper density operator through the $+$ component of the four current by $J^+ = (J^0 + J^3)/\sqrt{2}$. For one quark flavor q this is given by (Soper, 1977)

$$J_q^+(z^-, \mathbf{b}) = \bar{q}(0, z^-, \mathbf{b})\gamma^+ q(0, z^-, \mathbf{b})$$
$$= \sqrt{2}q_+^\dagger(0, z^-, \mathbf{b})q_+(0, z^-, \mathbf{b}), \quad (11)$$

where the q_+ fields are related to the quark fields q through a field redefinition involving the $\pm$ components of the Dirac γ matrices as $q_+ \equiv (1/2)\gamma^-\gamma^+ q$. In Eq. (11) light-cone coordinates are used with $a^\pm \equiv (a^0 \pm a^3)/\sqrt{2}$, and both quark fields are taken at the same light-cone time $z^+ = 0$. The transverse spatial coordinates are written as a two-dimensional vector $\mathbf{b}$. The relativistic density operator J_q^+ defined in Eq. (11) is a positive definite quantity. The electromagnetic

charge density operator J_{em}^+ is then obtained by a sum over quarks weighted by their electric charges e_q (in units of e) as

$$J_{\text{em}}^+(z^-, \mathbf{b}) = \sum_q e_q \bar{q}(0, z^-, \mathbf{b})\gamma^+ q(0, z^-, \mathbf{b}). \quad (12)$$

One can then examine the transverse structure of the nucleon due to the fact that transverse boosts are independent of interactions in the infinite-momentum frame (Kogut and Soper, 1970; Burkardt, 2006). Transversely localized nucleon states (Soper, 1977; Diehl, 2002, 2003b; Burkardt, 2003) with transverse center-of-mass position $\mathbf{R}$ set to 0 can be defined in terms of the linear superposition of states of transverse momentum as (Miller, 2019)

$$|p^+, \mathbf{R} = \mathbf{0}, \lambda\rangle \equiv N \int \frac{d^2\mathbf{p}_\perp}{(2\pi)^2\sqrt{2p^+}}|p^+, \mathbf{p}_\perp, \lambda\rangle, \quad (13)$$

with $|p^+, \mathbf{R} = \mathbf{0}, \lambda\rangle$ the light-cone helicity (λ) eigenstates (Soper, 1977) and N a normalization factor.

Using the density operator of Eq. (11), one can define transverse densities ρ_λ^q for a quark of flavor q in a transversely localized hadron as (Burkardt, 2000, 2003; Miller, 2007)

$$\rho_\lambda^q(b) \equiv \frac{1}{2P^+}\langle P^+, \mathbf{R} = \mathbf{0}, \lambda|J_q^+(0, \mathbf{b})|P^+, \mathbf{R} = \mathbf{0}, \lambda\rangle. \quad (14)$$

Using the translation operator in the transverse spatial direction, one can express $J_q^+(0, \mathbf{b}) = e^{-i\hat{\mathbf{P}}_\perp \cdot \mathbf{b}}J_q^+(0)e^{i\hat{\mathbf{P}}_\perp \cdot \mathbf{b}}$ in terms of the local current operator at the origin $J_q^+(0)$. Using Eq. (13) then allows one to express the quark transverse density of Eq. (14) as

$$\rho_\lambda^q(b) \equiv \int \frac{d^2\mathbf{\Delta}_\perp}{(2\pi)^2}e^{-i\mathbf{\Delta}_\perp \cdot \mathbf{b}}\frac{1}{2P^+}\left\langle P^+, \frac{\mathbf{\Delta}_\perp}{2}, \lambda\left|J_q^+(0)\right|P^+, -\frac{\mathbf{\Delta}_\perp}{2}, \lambda\right\rangle. \quad (15)$$

In the two-dimensional Fourier transform of Eq. (15), the vector $\mathbf{b}$ denotes the quark position (in the transverse plane) from the transverse center of momentum of the hadron. It is the position variable conjugate to the hadron relative transverse momentum $\mathbf{\Delta}_\perp$. The quantity $\rho_\lambda^q(b)$ has the interpretation of the two-dimensional transverse density to find a quark of flavor q at distance $b = |\mathbf{b}|$ from the transverse c.m. of the hadron with helicity λ.

For a quark of flavor q in the proton, the matrix element of the J_q^+ operator entering the two-dimensional Fourier transform in Eq. (15) can be expressed in terms of the quark flavor contribution F_1^q to the proton Dirac form factor as

$$\frac{1}{2P^+}\left\langle P^+, \frac{\mathbf{\Delta}_\perp}{2}, \lambda\left|J_q^+(0)\right|P^+, -\frac{\mathbf{\Delta}_\perp}{2}, \lambda\right\rangle = F_1^q(-\mathbf{\Delta}_\perp^2), \quad (16)$$

which allows one to express the density for a quark of flavor q in the proton, using Eq. (15), as

$$\rho^q(b) = \int \frac{d^2\mathbf{\Delta}_\perp}{(2\pi)^2} e^{-i\mathbf{\Delta}_\perp \cdot \mathbf{b}} F_1^q(-\mathbf{\Delta}_\perp^2)$$

$$= \int_0^\infty \frac{dQ}{2\pi} Q J_0(bQ) F_1^q(-Q^2), \qquad (17)$$

where on the second line the circular symmetry of the transverse density was used to convert the two-dimensional Fourier transform to a one-dimensional integral over $Q \equiv |\mathbf{\Delta}_\perp|$, with J_n denoting the cylindrical Bessel function of the order of n. Furthermore, the helicity subscript λ has been omitted since for a spin-1/2 system $\rho_{+1/2} = \rho_{-1/2}$.

The two-dimensional electric charge density in a proton is then obtained as follows as the sum over the quarks weighted by their electric charges:

$$\rho(b) = \sum_q e_q \rho^q(b). \qquad (18)$$

From the experimentally measured Dirac form factor F_1 of the proton

$$F_{1p} = \sum_q e_q F_1^q, \qquad (19)$$

one obtains

$$\rho_p(b) = \int_0^\infty \frac{dQ}{2\pi} Q J_0(bQ) F_{1p}(-Q^2). \qquad (20)$$

A similar formula holds for the neutron with the interchange $\rho^u \leftrightarrow \rho^d$ in Eq. (18) and $F_1^u \leftrightarrow F_1^d$ in Eq. (19). In this way, it was observed by Miller (2007) that the neutron transverse charge density reveals the well-known negative contribution at large distances, around 1.5 fm, due to the pion cloud, a positive contribution at intermediate b values, and a negative core at b values smaller than about 0.3 fm. One can understand the negative value of the neutron $\rho(b=0)$ from Eq. (20) and the observation that over the entire measured Q^2 range the neutron Dirac form factor F_{1n} is negative.

The quark charge densities in Eq. (20) do not fully describe the e.m. structure of the hadron. For a proton, the densities with $\lambda = \pm 1/2$ yield the same information, while a spin-1/2 system is described by two independent electromagnetic form factors. In general, a particle of spin S is described by $(2S+1)$ e.m. moments. To fully describe the structure of a hadron one also needs to consider the charge densities in a transversely polarized hadron state, with the transverse polarization direction denoted by $\mathbf{S}_\perp$. The transverse charge densities can be defined through matrix elements of the density operator J_q^+ in eigenstates of transverse spin (Carlson and Vanderhaeghen, 2008, 2009; Lorcé, 2009) as

$$\rho_{Ts_\perp}^q(\mathbf{b}) \equiv \int \frac{d^2\mathbf{\Delta}_\perp}{(2\pi)^2} e^{-i\mathbf{\Delta}_\perp \cdot \mathbf{b}}$$

$$\times \frac{1}{2P^+} \left\langle P^+, \frac{\mathbf{\Delta}_\perp}{2}, s_\perp \left| J_q^+(0) \right| P^+, \frac{-\mathbf{\Delta}_\perp}{2}, s_\perp \right\rangle, \qquad (21)$$

where $s_\perp$ is the hadron spin projection along the transverse spin direction $\mathbf{S}_\perp \equiv \cos\phi_S \mathbf{e_x} + \sin\phi_S \mathbf{e_y}$, with $\mathbf{e_x}$ and $\mathbf{e_y}$ the two unit vectors in the transverse plane.

If one expresses the transverse spin state in terms of the light-front helicity spinor states as

$$\left| s_\perp = +\frac{1}{2} \right\rangle = \frac{1}{\sqrt{2}} \left\{ \left| \lambda = +\frac{1}{2} \right\rangle + e^{i\phi_s} \left| \lambda = -\frac{1}{2} \right\rangle \right\}, \qquad (22)$$

the matrix element of the J_q^+ operator entering the two-dimensional Fourier transform in Eq. (21) can be expressed in terms of the quark flavor contribution to both the Dirac (F_1^q) and Pauli (F_2^q) form factors as

$$\frac{1}{2P^+} \left\langle P^+, \frac{\mathbf{\Delta}_\perp}{2}, s_\perp \left| J_q^+(0) \right| P^+, -\frac{\mathbf{\Delta}_\perp}{2}, s_\perp \right\rangle$$

$$= F_1^q(-\mathbf{\Delta}_\perp^2) + \frac{i}{2M}(\mathbf{S}_\perp \times \mathbf{\Delta}_\perp)_z F_2^q(-\mathbf{\Delta}_\perp^2). \qquad (23)$$

When one takes the weighted sum over the quark charges, the Fourier transform defined by Eq. (21) can then be worked out as (Carlson and Vanderhaeghen, 2008)

$$\rho_{Ts_\perp}(\mathbf{b}) = \rho(b) + \sin(\phi_b - \phi_S) \int_0^\infty \frac{dQ}{2\pi} \frac{Q^2}{2M} J_1(bQ) F_2(-Q^2), \qquad (24)$$

where the second term, which describes the deviation from the circular symmetric unpolarized charge density, depends on the quark position $\mathbf{b} = b(\cos\phi_b \mathbf{e_x} + \sin\phi_b \mathbf{e_y})$. While the density ρ_λ for a hadron in a state of definite helicity is circularly symmetric for all spins, the density $\rho_{Ts_\perp}$ also depends on the orientation of the position vector $\mathbf{b}$ relative to the transverse spin vector $\mathbf{S}_\perp$, as illustrated in Fig. 4. Therefore, it contains information on the hadron shape, projected on a plane perpendicular to the line of sight. Guo, Ji, and Shiells (2021) recently emphasized that, in order to define intrinsic quark densities in transverse space, one needs to remove the center-of-mass motion. This amounts to the replacement of F_2 with $F_1 + F_2$ in Eqs. (23) and (24).

As the density ρ_T is not circularly symmetric, one can calculate the dipole moment of its distribution as
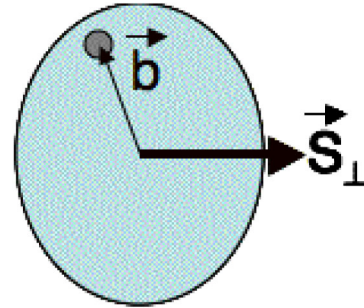

FIG. 4. Schematic view of the projection of the charge density along the line of sight (perpendicular to the image) for a hadron polarized along the direction of $\mathbf{S}_\perp$. The position of the quark charge inside the hadron is denoted by $\mathbf{b}$.
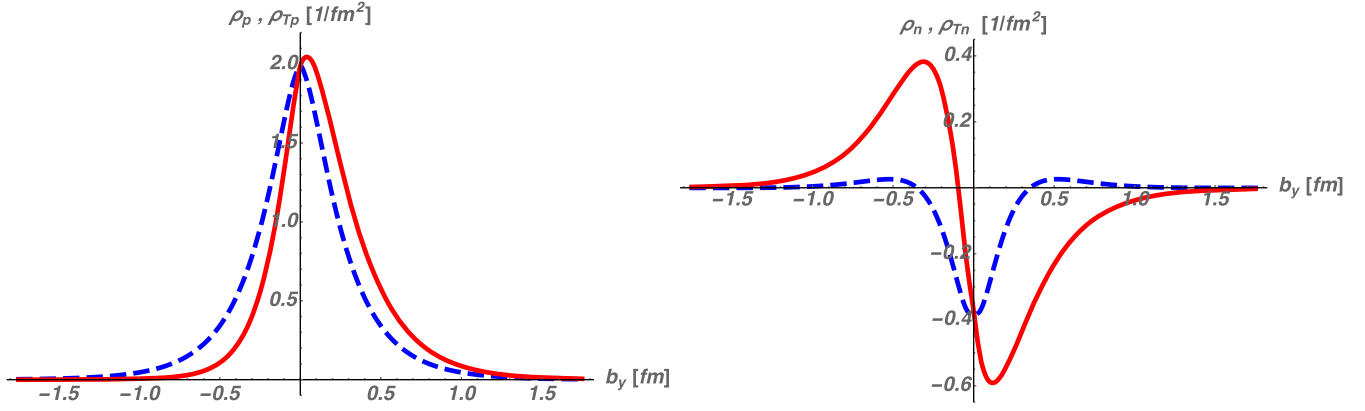
FIG. 5. Transverse charge densities for a proton (left panel) and neutron (right panel). The curves show the density along the y axis for an unpolarized nucleon (dashed blue curves), and for a nucleon polarized along the x axis (solid red curves). For the nucleon form factors, the empirical parametrization of Ye et al. (2018) was used.

$$\mathbf{d} \equiv e \int d^2\mathbf{b}\, \mathbf{b} \rho_{Ts_\perp}(\mathbf{b}) = -\frac{e}{2M} F_2(0)(\mathbf{S}_\perp \times \mathbf{e_z}). \quad (25)$$

Equation (25) implies that polarizing the proton along the x axis leads to an induced electric dipole moment along the y axis that is equal to the value of the anomalous magnetic moment, i.e., $F_2(0)$ (in units $e/2M$), as first noticed by Burkardt (2000). One can understand this induced electric dipole field pattern from special relativity, as the nucleon spin along the x axis is the source of a magnetic dipole field, denoted by $\vec{B}$. An observer moving toward the nucleon with velocity $\vec{v}$ will see an electric dipole field pattern with $\vec{E}' = -\gamma(\vec{v} \times \vec{B})$ giving rise to the observed effect.

We show the transverse charge densities in a proton and neutron in Fig. 5 based on the recent parametrization of Ye et al. (2018) for the proton and neutron form factors. One notices that for the proton the unpolarized charge density is positive everywhere. For a transversely polarized proton along the x axis, one notices a small displacement of the charge density along the y axis proportional to the proton's anomalous magnetic moment. For the neutron, the unpolarized density shows the negatively charged core, positive intermediate contribution, and negative pion cloud contribution at large distances, as previously described. The corresponding transverse charge density for a neutron polarized along the x axis gets significantly displaced due to the large negative value of the neutron anomalous magnetic moment.

The previously discussed light-front densities require us to develop some new intuition, as they are defined at the same light-front time ($z^+ = 0$) as their constituents. When constituents move nonrelativistically, it does not make a difference whether they are observed at the same time ($t = 0$) or the same light-front time ($z^+ = 0$), since the constituents can move only a negligibly small distance during the small time interval that a light ray needs to connect them. This is not the case, however, for bound systems of relativistic constituents such as hadrons (Jarvinen, 2005; Hoyer, 2009). For the latter, the transverse density at equal light-front times can be interpreted as a two-dimensional flash photograph of a three-dimensional object (Brodsky et al., 2015), thereby reflecting the position of

charged constituents at different times, which are causally connected by a light ray.

D. Radii of quark distributions in a proton

As previously discussed, to define and reconstruct a three-dimensional charge distribution from elastic electron-scattering measurements of the form factors of a system requires that one is able to localize the object and fix its center of mass, with respect to which one defines the charge distribution (Jaffe, 2021). This is possible for nonrelativistic static systems for which the typical size is much larger than its Compton wavelength, allowing the probe to localize the charges at distances between the two scales. For atomic nuclei, this condition is well satisfied, as their Compton wavelength (of the order of $0.2/A$ fm) is typically much smaller than their size (of the order of $1.2A^{1/3}$ fm). As an example, for the ^{12}C nucleus, its size of around 2.5 fm is much larger than its Compton wavelength of around 0.02 fm, which allows one to localize charges in between these length scales and reconstruct a charge distribution. For such systems, one can define a three-dimensional charge distribution as Fourier transform of the measured electric form factor G_E as given in Eq. (6). For such a charge distribution, one can define a radius through the following normalized moment:

$$\langle r_E^2 \rangle \equiv \frac{\int d^3\vec{r}\, r^2 \rho_{3D,\text{n-rel}}(r)}{\int d^3\vec{r}\, \rho_{3D,\text{n-rel}}(r)}. \quad (26)$$

Inserting the three-dimensional density defined in Eq. (6) allows one to express the charge radius as

$$\langle r_E^2 \rangle = -6 \frac{G_E'(0)}{G_E(0)}, \quad (27)$$

where $G_E'(0) \equiv (dG_E/dQ^2)|_{Q^2=0}$, with $Q^2 = \vec{q}^2$. One can therefore express the Taylor expansion of G_E at low values of Q^2 as

$$G_E(-Q^2) \equiv G_E(0)\{1 - \tfrac{1}{6}\langle r_E^2 \rangle Q^2 + \mathcal{O}(Q^4)\} \quad (28)$$

and access the charge radius experimentally from the electric form factor slope at the origin.

Applying the previous concepts to a nucleon becomes problematic since the nucleon's size (of the order of 0.85 fm) is not much larger than its Compton wavelength (of the order of 0.2 fm), making it impossible to localize the center of mass in three spatial dimensions. Besides, for light-quark systems we have discussed that an interpretation in terms of a positive definite quantity is spoiled in the rest frame due to pair creation processes. In Sec. III.C, we reviewed how to properly define density distributions for a nucleon, which is a relativistic bound state. Going to the infinite-momentum frame allows one to localize the hadron in a plane perpendicular to the direction of a fast-moving observer and define density distributions in that plane. For the resulting two-dimensional transverse distributions for a quark of flavor q in the proton, one can then define a mean-squared transverse radius as

$$\langle b^2 \rangle^q = \frac{\int d^2\mathbf{b}\, \mathbf{b}^2 \rho^q(b)}{\int d^2\mathbf{b}\, \rho^q(b)} = -4 \frac{F_1'^q(0)}{F_1^q(0)}, \qquad (29)$$

where $F_1'^q(0) \equiv (dF_1^q/dQ^2)|_{Q^2=0}$ denotes the slope at the origin of the corresponding Dirac form factor. Note that the radius definition of Eq. (29) for each quark flavor is properly normalized to the number of valence quarks in the proton $[F_1^u(0) = 2$ and $F_1^d(0) = 1]$, yielding

$$\langle b^2 \rangle^u = -2F_1'^u(0), \qquad \langle b^2 \rangle^d = -4F_1'^d(0). \qquad (30)$$

To determine the mean-squared transverse radii [Eq. (30)] for each quark flavor, we start by expressing the proton and neutron Dirac form factors, using isospin symmetry, as

$$\begin{aligned} F_{1p} &= e_u F_1^u + e_d F_1^d, \\ F_{1n} &= e_u F_1^d + e_d F_1^u, \end{aligned} \qquad (31)$$

which allows one to extract the Dirac form factors for the u- and d-quark flavors. These enter the corresponding transverse quark densities as

$$F_1^u = 2F_{1p} + F_{1n}, \qquad F_1^d = 2F_{1n} + F_{1p}. \qquad (32)$$

Combined with Eqs. (30) and (31), Eq. (32) allows one to express the proper mean-squared transverse radii for the u- and d-quark distributions in a proton as

$$\begin{aligned} \langle b^2 \rangle^u &= -2\{2F_{1p}'(0) + F_{1n}'(0)\}, \\ \langle b^2 \rangle^d &= -4\{F_{1p}'(0) + 2F_{1n}'(0)\}. \end{aligned} \qquad (33)$$

Equation (33) allows one to express the difference of the mean-squared radii for d- and u-quark distributions in a proton as

$$\langle b^2 \rangle^d - \langle b^2 \rangle^u = -6F_{1n}'(0). \qquad (34)$$

To empirically determine the mean-squared transverse radii of u- and d-quark distributions in a proton, we relate the derivative of the Dirac form factors to the conventional Sachs

form factors G_E and G_M, defined in Eqs. (4) and (5), which yields

$$F_1'(0) = G_E'(0) + \frac{\kappa}{4M^2}. \qquad (35)$$

Following the convention for nonrelativistic static systems, one can Taylor expand the proton and neutron Dirac form factors at low-momentum transfer Q^2 as

$$G_{Ep}(-Q^2) \equiv 1 - \tfrac{1}{6}\langle r_{Ep}^2 \rangle Q^2 + \mathcal{O}(Q^4), \qquad (36)$$

$$G_{En}(-Q^2) \equiv -\tfrac{1}{6}\langle r_{En}^2 \rangle Q^2 + \mathcal{O}(Q^4). \qquad (37)$$

We emphasize again that for relativistic bound states such as a nucleon where the concept of a three-dimensional charge distribution is not well defined, Eqs. (36) and (37) are used merely as operational definitions for the form factor slopes at the origin, even though we refer to these quantities for simplicity as "radii" in the remainder of this review. Equations (36) and (37) then allow one to express for the nucleon $(N = p, n)$

$$-6F_{1N}'(0) = \langle r_{EN}^2 \rangle - \frac{3\kappa_N}{2M^2}, \qquad (38)$$

where the anomalous magnetic moment contribution is known as the Foldy term.

The radius of the transverse charge distribution in a proton is then obtained as the following sum over the radii for the quark distributions weighted by their charges:

$$\langle b^2 \rangle_p = \tfrac{4}{3}\langle b^2 \rangle^u - \tfrac{1}{3}\langle b^2 \rangle^d = -4F_{1p}'(0). \qquad (39)$$

For the neutron, assuming isospin symmetry, we define a transverse charge radius as[1]

$$\langle b^2 \rangle_n = \tfrac{2}{3}\langle b^2 \rangle^d - \tfrac{2}{3}\langle b^2 \rangle^u = -4F_{1n}'(0). \qquad (40)$$

In Table I, we show the empirical values of proton and neutron radii $\langle r_E^2 \rangle$, the Foldy terms, the extracted Dirac slopes $F_1'(0)$, and the transverse charge radii $\langle b^2 \rangle$. For the proton values for $\langle r_{Ep}^2 \rangle$, we show both the recent analysis of Cui *et al.* (2021) based on e-p-scattering results, which are discussed in Sec. V [Eq. (73)], and the extracted value from the μH Lamb shift measurements, which are discussed in Sec. VI [Eq. (76)]. Anticipating the discussion in Sec. VI, the quantity entering the hydrogen spectroscopy Lamb shift experiments is also given by the slope $G_{Ep}'(0)$. Therefore, it is important and meaningful to compare the proton charge radius values obtained using these two experimental techniques. We see in Table I that the extracted mean-squared transverse radii $\langle b^2 \rangle$ are consistent between the two analyses, showing that the transverse charge distribution in a proton has a rms radius of around 0.63 fm, as seen by an observer moving with a light

---

[1]Note that for a neutron this follows the convention in defining a charge radius for a neutral system, as one cannot use the definition of Eq. (29), which is normalized to the total charge.

TABLE I. Empirical values of the proton and neutron radii $\langle r_E^2 \rangle$, Foldy terms, Dirac slopes $F_1'(0)$, and transverse charge radii $\langle b^2 \rangle$. For the proton, we show the values both using the e-p-scattering data analysis of Cui *et al.* (2021) and the values from μH Lamb shift measurements (Antognini *et al.*, 2013).

	$\langle r_E^2 \rangle$ (fm^2)	$-3\kappa_N/2M^2$ (fm^2)	$-6F_1'(0)$ (fm^2)	$\langle b^2 \rangle$ (fm^2)
Proton (e-p)	0.717 ± 0.014 (Cui *et al.*, 2021)	−0.1189	0.598 ± 0.014	0.399 ± 0.009
Proton (μH)	0.7071 ± 0.0007 (Antognini *et al.*, 2013)		0.5882 ± 0.0007	0.3921 ± 0.0005
Neutron (PDG)	−0.1161 ± 0.0022 (Zyla *et al.*, 2020)	0.1266	0.0105 ± 0.0022	0.0070 ± 0.0015

front. For the neutron, one notices that its Dirac slope value $F_{1n}'(0)$ is the result of a large cancellation between the $\langle r_{En}^2 \rangle$ term and the Foldy term, which have opposite signs, resulting in a value of $F_{1n}'(0)$ that is around 10% of the size of each contribution. As the Foldy term for the neutron is slightly larger in absolute value than the $\langle r_{En}^2 \rangle$ term, the positive value of $-6F_{1n}'(0)$ results from Eq. (34) in a slightly larger mean-squared radius for the d quarks in a proton relative to the u quarks in the proton, thereby confirming the observation of Cates *et al.* (2011) based on a flavor decomposition of proton and neutron form factors.

In Table II, we show the extracted values of the mean-squared transverse radii for u- and d-quark distributions in the proton, using the neutron PDG value for $\langle r_{En}^2 \rangle$, and both analyses for the proton as shown in Table I. For the more accurate values extracted from the μH Lamb shift measurements, one obtains a precision of 0.3% (0.7%) on the mean-squared transverse radii for the u-quark (d-quark) distributions. Using the values in Table I, we notice that the neutron $F_{1n}'(0)$ term contributes 1% (4%) to the mean-squared radii for the u-quark (d-quark) distributions, respectively, in Eq. (33). One also notices that the uncertainty on the neutron $F_{1n}'(0)$ value is at present the limiting uncertainty in the extraction of the mean-squared transverse radius value for the d-quark distribution.

Later we discuss unpolarized and polarized electron-proton elastic scatterings and the methods to extract the proton electric form factor and the proton charge radius value based on the definition of Eq. (36) as the slope of the form factor G_E at the origin. Likewise, one can define a magnetic radius as the slope at the origin of the form factor G_{MN} for the nucleon ($N = p, n$) as follows:

$$G_{MN}(-Q^2) \equiv \mu_N \{ 1 - \tfrac{1}{6} \langle r_{MN}^2 \rangle Q^2 + \mathcal{O}(Q^4) \}, \quad (41)$$

where μ_N is the nucleon magnetic moment, $\mu_p = 2.79$ and $\mu_n = -1.91$, in the units of the nucleon magneton.

TABLE II. Extracted values of the mean-squared transverse radii for u- and d-quark distributions in the proton, using the neutron PDG value for $\langle r_{En}^2 \rangle$ given in Table I, and for the proton values for $\langle r_{Ep}^2 \rangle$ from both the analysis of Cui *et al.*, 2021 based on e-p-scattering results and the extracted value from the μH Lamb shift measurements (Antognini *et al.*, 2013).

	$\langle b^2 \rangle^u$ (fm^2)	$\langle b^2 \rangle^d$ (fm^2)
Proton (e-p)	0.402 ± 0.009	0.413 ± 0.010
Proton (μH)	0.396 ± 0.001	0.406 ± 0.003

Ideally, to extract the proton charge radius value, one needs to extract the proton electric form factor G_E all the way down to $Q^2 = 0$ and then determine its slope. In practice, it is not possible to measure G_E at $Q^2 \sim 0$, which corresponds to near 0° scatterings. Therefore, some type of extrapolation is unavoidable, which may introduce systematic uncertainties associated with the determination of $\langle r_{Ep}^2 \rangle^{1/2}$, as discussed later.

A theoretical determination of the proton radius starting with QCD requires a nonperturbative framework. The only current *ab initio* tool is lattice QCD. The standard procedure in lattice QCD is to compute the electric form factor for finite values of the momentum transfer and then perform a fit to determine the slope at zero momentum transfer, such as through a popular dipole fit or a z-expansion fit. However, on a finite lattice the smallest nonzero momentum is $2\pi/L$, with L the spatial size of the lattice. Therefore, reaching small momentum transfers is challenging as it requires large lattices. Furthermore, although electromagnetic form factors have been studied within lattice QCD for many years, it is only recently that they have been extracted using simulations with physical values of the light-quark masses.

In Fig. 6, we show a compilation of recent lattice QCD results for both the isovector charge radius $(\langle r_{Ep}^2 \rangle - \langle r_{En}^2 \rangle)^{1/2}$ and the proton charge radius, obtained from ensembles at or near the physical pion mass. For the isovector radius, only the connected quark diagrams, in which the photon couples to the quarks connected to either the intial or final nucleon, contribute. The proton charge radius also requires a much harder calculation of the contribution from disconnected diagrams in which the photon couples to a $q\bar{q}$ loop, which interacts with the quarks in the initial and final protons through gluon exchanges. Although the disconnected contribution to the proton electric form factor at low-momentum transfer is found to be in the 1% range (Alexandrou *et al.*, 2019), its omission would result in an uncontrolled systematic error. Such systematics need to be under control for precision comparisons of the proton charge radius at the 1% level or better.

Improving on the precision of the lattice extractions of the proton charge radius also requires one to reduce the model error induced by a form factor fit, which has been done in most of the lattice results so far. To this end, a first step was taken in the lattice study of Alexandrou *et al.* (2020), which explored a direct method to extract the proton radius that does not depend on fitting the form factor, displayed as ETMC 20 in Fig. 6.

The lattice calculations have made important progress in recent years by controlling excited state contamination and by performing calculations at the physical point. One notices in
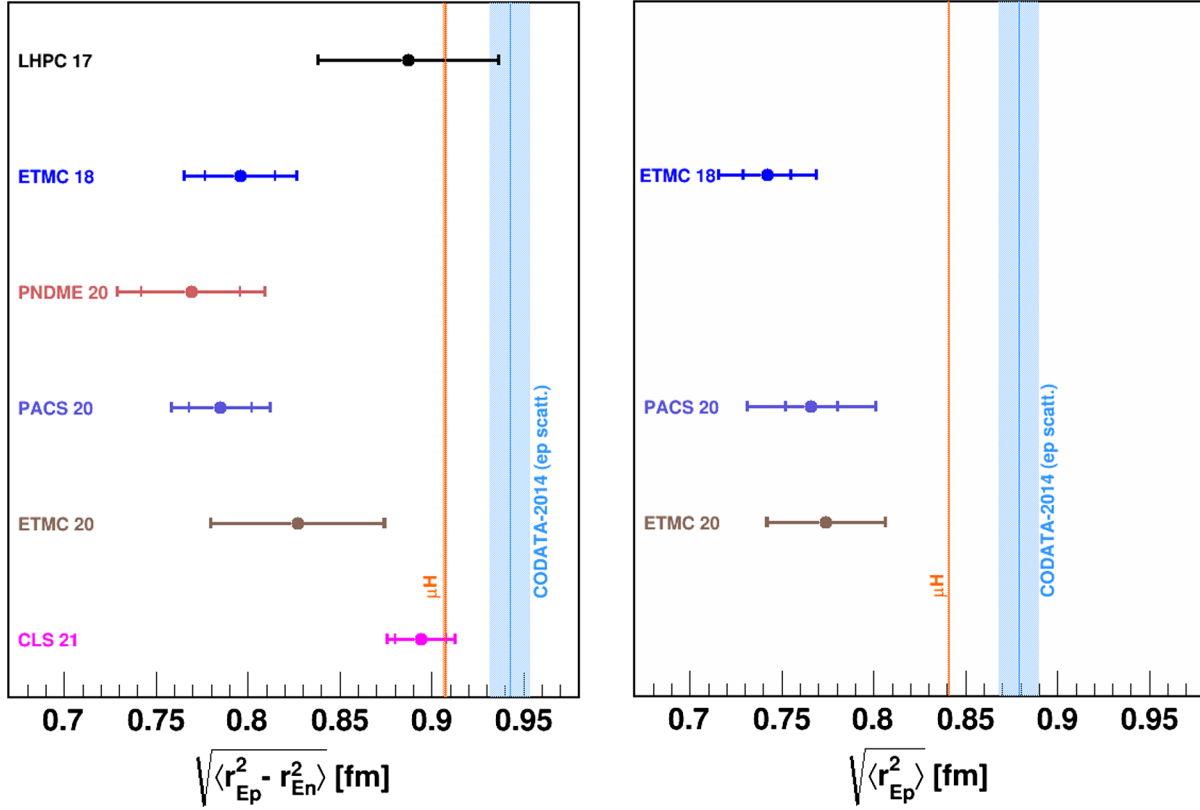
FIG. 6. Compilation of recent lattice QCD results for the isovector charge radius (left panel) and the proton charge radius (right panel) obtained from ensembles at the physical pion mass. Results shown are from LHPC (Hasan *et al.*, 2018) and ETMC, both using a form factor fit ETMC 18 (Alexandrou *et al.*, 2019), as well as the direct calculation of the radius ETMC 20, avoiding an extrapolation through a form factor fit (Alexandrou *et al.*, 2020); PNDME (Jang *et al.*, 2020); PACS (Shintani *et al.*, 2019); and CLS (Djukanovic *et al.*, 2021). Inner error bars display the statistical errors, whereas outer error bars display the full errors. The vertical bands show the empirical result extracted from muonic hydrogen spectroscopy and the CODATA-2014 recommended value, as discussed in Secs. V and VI. From Jingyi Zhou.

Fig. 6, however, that further improvements are called for to reach the precision level obtained in the empirical extractions.

E. The extraction of proton electromagnetic form factors

The differential cross section based on OPE for elastic electron-nucleon scattering can be written as

$$\frac{d\sigma}{d\Omega_{\text{lab}}} = \frac{\alpha^2}{4E^2 \sin^4(\theta/2)} \frac{E'}{E}$$
$$\times \left\{ \frac{G_E^2 + \tau G_M^2}{1+\tau} \cos^2\left(\frac{\theta}{2}\right) + 2\tau G_M^2 \sin^2\left(\frac{\theta}{2}\right) \right\}, \quad (42)$$

where E is the incident electron energy, E' is the energy of the scattered electron, θ is the electron-scattering angle, α is the fine-structure constant, $\tau \equiv Q^2/4M^2$, and the mass of the electron is neglected.

To separately determine the proton electric and magnetic form factor for each Q^2 value, ideally one would need to perform two measurements with independent combinations of G_E and G_M at the corresponding Q^2 value, with one of the measurements involving polarizations that we discuss later. However, polarization experiments have become possible only in recent decades. Historically, the Rosenbluth technique

(Rosenbluth, 1950) had been used extensively, which allows for the separation of these two form factors by performing unpolarized differential cross-section measurements only. To see how this works, one can rewrite Eq. (42) as

$$\frac{d\sigma}{d\Omega_{\text{lab}}} = \sigma_M \frac{1}{1+\tau} \left\{ G_E^2 + \frac{\tau}{\epsilon} G_M^2 \right\}, \quad (43)$$

where $\epsilon = [1 + 2(1+\tau)\tan^2(\theta/2)]^{-1}$ is the virtual photon longitudinal polarization and σ_M is the following Mott cross section describing the scattering from a pointlike spinless target (where we included the recoil factor E'/E):

$$\sigma_M = \frac{\alpha^2 \cos^2(\theta/2)}{4E^2 \sin^4(\theta/2)} \left(\frac{E'}{E}\right). \quad (44)$$

At a fixed Q^2 value, one can take a series of measurements by varying the incident electron beam energy and the scattering angle. According to Eq. (43), one can then fit the measured reduced cross section $G_M^2 + \epsilon/\tau G_E^2$ as a function of ϵ. From the slope and the intercept of the fit, one can then determine G_E^2 and G_M^2. There are limitations to the Rosenbluth method: at low Q^2, due to the kinematic suppression, the extraction of the proton magnetic form factor is problematic, while at high Q^2 the

magnetic contribution dominates the cross section and the extraction of the proton G_E becomes difficult.

To overcome the aforementioned limitations associated with the Rosenbluth technique, an independent combination of the proton electric and magnetic form factors can be obtained by a double-polarization measurement from electron-proton elastic scattering in addition to unpolarized differential cross-section measurements, thereby separating these two form factors. Double-polarization measurements in the context of electron-proton scattering refer to the following two cases: (i) longitudinally polarized electrons scattering from a polarized proton target, and (ii) longitudinally polarized electrons scattering from an unpolarized proton target with the recoil proton polarization measured by a polarimeter. In this review, we do not review the technical aspects of polarized electron beams, polarized proton targets, or the recoil proton polarimeters. We instead refer interested readers to review articles by Gao (2003) and Perdrisat, Punjabi, and Vanderhaeghen (2007).

The one-photon-exchange diagram for spin-dependent electron-nucleon scattering is shown in Fig. 7. In this picture the incident electron is longitudinally polarized with a helicity of $h = \pm 1$, corresponding to an electron's spin being parallel or antiparallel to its momentum direction, respectively. The target proton spin vector is shown by a thick arrow, with θ^* and ϕ^* as its polar and azimuthal angles defined with respect to the three-momentum transfer vector $\mathbf{q}$ of the virtual photon. The scattering plane is defined as the x, z plane with $\hat{z} = \mathbf{q}/|\mathbf{q}|$ and $\hat{y} = (\mathbf{k} \times \mathbf{k}')/(|\mathbf{k}||\mathbf{k}'|)$, with $\mathbf{k}$ and $\mathbf{k}'$ the incident and scattered electron three-momentum vector, respectively. The spin-dependent asymmetry A is defined as $A = (\sigma^{h+} - \sigma^{h-})/(\sigma^{h+} + \sigma^{h-})$, where $\sigma^{h\pm}$ denotes the differential cross sections for the two different helicities of the polarized electron beam.

For longitudinally polarized electrons scattering from a polarized proton target, the differential cross section can be written as (Donnelly and Raskin, 1986)

$$\frac{d\sigma}{d\Omega} = \Sigma + h\Delta, \tag{45}$$

where Σ is the unpolarized differential cross section given by Eq. (42) and Δ is the spin-dependent differential cross section given by

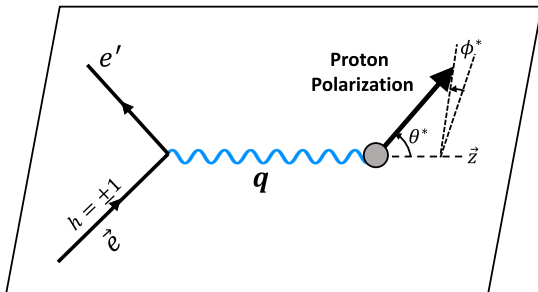$$\Delta = \sigma_{\text{Mott}}[v_z \cos\theta^* G_M^2 + v_x \sin\theta^* \cos\phi^* G_M G_E], \tag{46}$$

where

$$v_z = -2\tau \tan\left(\frac{\theta}{2}\right)\sqrt{\frac{1}{1+\tau} + \tan^2\left(\frac{\theta}{2}\right)}, \tag{47}$$

$$v_x = -2\tan\left(\frac{\theta}{2}\right)\sqrt{\frac{\tau}{1+\tau}} \tag{48}$$

are kinematic factors. The spin-dependent asymmetry A is defined in terms of the polarized and unpolarized cross sections as

$$A = \frac{\Delta}{\Sigma} = \frac{v_z \cos\theta^* G_M^2 + v_x \sin\theta^* \cos\phi^* G_M G_E}{(\epsilon G_E^2 + \tau G_M^2)/[\epsilon(1+\tau)]}. \tag{49}$$

The experimental asymmetry A_{exp} is related to the spin-dependent asymmetry of Eq. (49) by

$$A_{\text{exp}} = P_b P_t A, \tag{50}$$

where P_b and P_t are the beam and target polarizations, respectively. A determination of the ratio G_E/G_M, independent of the knowledge of the beam and target polarization, can be precisely obtained by measuring the so-called super ratio

$$R = \frac{A_1}{A_2} = \frac{v_z \cos\theta_1^* G_M^2 + v_x \sin\theta_1^* \cos\phi_1^* G_M G_E}{v_z \cos\theta_2^* G_M^2 + v_x \sin\theta_2^* \cos\phi_2^* G_M G_E}, \tag{51}$$

where A_1 and A_2 are elastic electron-proton-scattering asymmetries measured at an identical value of Q^2 simultaneously, but at two different proton spin orientations relative to $\mathbf{q}$, corresponding to (θ_1^*, ϕ_1^*) and (θ_2^*, ϕ_2^*), respectively. However, the proton spin direction is fixed in the laboratory frame; therefore, it is feasible if one has a symmetric detection system. For a symmetric detector configuration with respect to the incident electron momentum direction, A_1 and A_2 can be measured simultaneously by forming two independent asymmetries with respect to either the electron beam helicity or the target spin orientation in the beam-left and beam-right sector of the detector system, respectively. Thus, the proton form factor ratio can be determined with high systematic accuracy using this technique because it is insensitive to the uncertainties in determining the beam and the target polarizations.

FIG. 7. One-photon-exchange diagram for spin-dependent electron-proton scattering. From Jingyi Zhou.
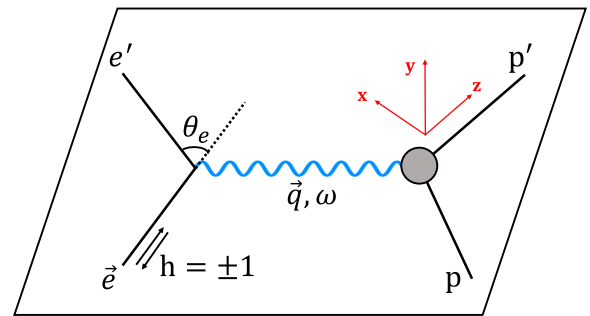

FIG. 8. The one-photon-exchange diagram for polarization transfer from longitudinally polarized electron to unpolarized proton. From Jingyi Zhou.

Such a technique was pioneered (Crawford *et al.*, 2007) in the BLAST experiment (Hasell *et al.*, 2011) at the former MIT-Bates linear accelerator center, where the proton electric to proton magnetic form factor ratio was extracted in the Q^2 range from 0.15 to 0.65 $(GeV/c)^2$.

In polarization transfer measurements (the polarization from the incident electron beam is transferred to the recoil protons) and the recoil proton polarization is measured using a recoil proton polarimeter, as illustrated in Fig. 8. Such a polarimeter relies on secondary scatterings (recoil protons from e-p scattering off an analyzer such as CH_2) and spin-orbital interactions of protons and nuclei and spin-dependent proton-proton interactions that give rise to azimuthal angular dependence in the distribution of the scattered protons. By analyzing such azimuthal angular dependence, one can determine the recoil proton polarization components in the reaction plane (the x-z plane in Fig. 8). Such secondary scatterings take place at the focal plane of the spectrometer, and the polarimeter is also called the focal-plane polarimeter (FPP). To determine the proton electric to magnetic form factor ratio at the target from the proton polarization components measured at the focal plane, an involved spin transport process is needed because the proton spin rotates as it goes through various magnetic components inside a magnetic spectrometer. The proton polarization measured by FPP ($\vec{P}_{FPP}$) and the proton polarization at the target ($\vec{P}$) are related through a three-dimensional spin rotation matrix. The elements of the spin rotation matrix can be calculated from a detailed modeling of the magnetic spectrometer including all spectrometer magnets (dipole, quadrupoles), fringe fields, dipole field gradient, etc. For details on such polarimeters, see the review by Perdrisat, Punjabi, and Vanderhaeghen (2007).

In the one-photon-exchange Born approximation, the scattering of longitudinally polarized electrons results in a transfer of polarization to the recoil proton with only two nonzero components: P_x, which is perpendicular to the proton momentum in the scattering plane, and P_z, which is parallel to the proton momentum in the scattering plane, as illustrated in Fig. 8 (Arnold, Carlson, and Gross, 1981). The form factor ratio can be determined from a simultaneous measurement of the two recoil polarization components in the scattering plane as

$$\frac{G_E}{G_M} = -\frac{P_x}{P_z}\frac{E + E'}{2M}\tan(\theta/2), \tag{52}$$

in terms of the incident and scattered electron energies E and E', respectively, and electron-scattering angle θ. The polarization transfer measurement was carried out by Zhan *et al.* (2011) and a proton charge radius value was extracted by combining unpolarized electron-proton-scattering data; see Sec. V.B.

F. Two-photon-exchange contribution to electron-proton scattering

Note that all our discussions thus far have been based on the dominant OPE Born diagram contribution in electron-proton scattering, as higher-order contributions are suppressed due to the smallness of the fine-structure constant ($\alpha \simeq 1/137$).
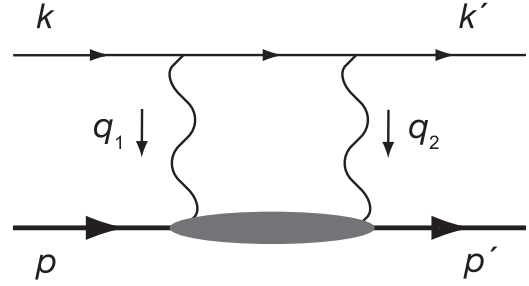

FIG. 9. Two-photon-exchange diagram for elastic electron-proton scattering. The blob denotes the doubly virtual Compton subprocess on the proton.

The next-to-leading-order contribution is the two-photon-exchange (TPE) contribution, as shown in Fig. 9, which is proportional to the doubly virtual Compton subprocess on the proton side.

The TPE contribution became of a strong interest after a drastic difference was reported on the proton G_E/G_M ratio measured directly using a recoil proton polarimeter (Jones *et al.*, 2000) from those using Rosenbluth separation. The data from Jones *et al.* (2000) and the subsequent recoil polarization experiments (Gayou *et al.*, 2002; Punjabi *et al.*, 2005; Puckett *et al.*, 2010) show interesting behavior at higher Q^2; i.e., G_{Ep} falls off much faster than G_{Mp} as a function of Q^2, while the two form factors extracted from unpolarized differential cross-section measurements using the Rosenbluth separation method show a similar Q^2 dependence. The near constant behavior of the proton G_{Ep}/G_{Mp} ratio extracted from unpolarized measurements was confirmed and extended to a higher Q^2 value near 5.5 $(GeV/c)^2$ by another experiment at Jefferson Lab (Christy *et al.*, 2004). The first explanations of such puzzling behavior pointed toward hard TPE processes between the electron and the proton, which become relevant once experiments aim to access terms that contribute at or below the percent level to the scattering cross section as is the case in the Rosenbluth method at larger Q^2 values (Blunden, Melnitchouk, and Tjon, 2003; Guichon and Vanderhaeghen, 2003). This unexpected behavior triggered intensive experimental and theoretical studies of the TPE effect in electron-proton scattering in the last two decades as its effect is expected to be different in unpolarized cross-section measurements than in recoil polarization experiments; see Carlson and Vanderhaeghen (2007) and Arrington, Blunden, and Melnitchouk (2011) for some early reviews of this field.

To account for two-photon and multiphoton exchange effects in a model-independent way requires one to generalize the amplitude of Eq. (1) by describing the elastic e-p scattering. Neglecting the electron mass, the elastic e-p-scattering amplitude, following the notations introduced in Sec. III.A, can be expressed through the following three independent structures (Guichon and Vanderhaeghen, 2003):

$$\mathcal{M}_{h,\lambda'\lambda} = i(e^2/Q^2)\bar{u}(k', h)\gamma_\mu u(k, h)$$
$$\times \bar{N}(p', \lambda')\left(\tilde{G}_M\gamma^\mu - \tilde{F}_2\frac{P^\mu}{M} + \tilde{F}_3\frac{\gamma \cdot KP^\mu}{M^2}\right)N(p, \lambda),$$
$$\tag{53}$$

in which $K \equiv (k + k')/2$ and where the functions $\tilde{G}_M$, $\tilde{F}_2$, and $\tilde{F}_3$ are complex functions of ϵ and Q^2. In the OPE approximation, the functions $\tilde{G}_M$ and $\tilde{F}_2$ reduce to the Q^2-dependent form factors G_M and F_2, respectively, while the function $\tilde{F}_3$ vanishes. When accounting for the small electron helicity flip effects, which are proportional to its mass, it was shown by Gorchtein, Guichon, and Vanderhaeghen (2004) that three more amplitudes are needed to fully describe the e-p-scattering amplitude. Based on such a general analysis, the TPE corrections to both unpolarized and polarization observables were expressed by Guichon and Vanderhaeghen (2003) in terms of the amplitudes $\tilde{G}_M$, $\tilde{F}_2$, and $\tilde{F}_3$. In that work it was shown that, by adding a TPE contribution of the size expected from perturbation theory, it is possible to simultaneously account for the relatively large correction to the unpolarized observable when extracting the G_{Ep}/G_{Mp} ratio at larger Q^2 while maintaining a small correction in the polarization observables.

To use electron scattering as a precision tool, it is indispensable to arrive at a better quantitative understanding of TPE processes, and a lot of activities have taken place over the past two decades or are planned for the near future. There are observables that provide us with clear indications of the size of TPE effects, as they would be exactly zero in the absence of two-photon-exchange or multiphoton-exchange contributions. Such observables are normal single-spin asymmetries (SSAs) of electron-nucleon scattering, where either the electron spin or the nucleon spin is polarized normal to the scattering plane. Because such SSAs are proportional to the imaginary part of a product of two amplitudes, they are zero for real (nonabsorptive) processes such as OPE. At leading order in the fine-structure constant, they result from the product of the OPE amplitude and the imaginary part of the TPE amplitude. For the target normal SSA, they were predicted to be in the percent or subpercent range some time ago (De Rujula, Kaplan, and De Rafael, 1971). A measurement of the normal SSA for the elastic electron-^{3}He scattering by the Jefferson Lab (JLab) Hall A Collaboration extracted a SSA for the elastic electron-neutron subprocess in the percent range (Zhang et al., 2015). For the experiments with polarized beams, the corresponding normal SSAs were predicted to be in the range of a few to hundred ppm for electron beam energies in the GeV range (Afanasev, Akushevich, and Merenkov, 2002; Gorchtein, Guichon, and Vanderhaeghen, 2004; Pasquini and Vanderhaeghen, 2004). Although such beam normal spin asymmetries are small, as they are proportional to the electron mass, the parity-violation programs at the major electron laboratories have reached precisions on asymmetries with longitudinal polarized electron beams well below the ppm level, and the next generations of such experiments are designed to reach precisions at the sub-ppb level (Kumar et al., 2013). The beam normal SSA, which is due to TPE and thus parity conserving, has been measured over the past two decades as a spin-off in the parity-violating electron-scattering programs at MIT-Bates (SAMPLE Collaboration) (Wells et al., 2001), MAMI (A4 Collaboration) (Maas et al., 2005; Balaguer Rios, 2012; Gou et al., 2020), and JLab [G0 Collaboration (Armstrong et al., 2007; Androić et al., 2011),

HAPPEX/PREX Collaboration (Abrahamyan et al., 2012), and Qweak Collaboration (Androić et al., 2020)]. The resulting beam normal SSA range from a few ppm in the forward angular range to around a hundred ppm in the backward angular range, in qualitative agreement with theoretical TPE expectations.

While the nonzero normal SSAs in elastic electron-nucleon scattering quantify the imaginary parts of the TPE amplitudes, measurements of their real parts have also been performed by several dedicated experiments over the past few years. In particular, the deviation from unity of the elastic-scattering cross-section ratio $R_{2\gamma} \equiv e^+ p/e^- p$ is proportional to the real part of the product of OPE and TPE amplitudes. Recent measurements of $R_{2\gamma}$ for Q^2 up to 2 GeV^2 were performed at VEPP-3 (Rachek et al., 2015), by the CLAS Collaboration at JLab (Adikaram et al., 2015; Rimal et al., 2017), and by the OLYMPUS Collaboration at DESY (Henderson et al., 2017). These experiments show that $R_{2\gamma}$ ranges, for the kinematic region corresponding to $Q^2 = 0.5$–1 GeV^2 and virtual photon polarization parameter $\epsilon = 0.8$–0.9, from a value $R_{2\gamma} \approx 0.99$ (Henderson et al., 2017), showing a deviation from unity within 2σ to 3σ (statistical and uncorrelated systematic errors), to a value $R_{2\gamma} = 1.02$–1.03 for $Q^2 \approx 1.5$ GeV^2 and $\epsilon \approx 0.45$ (Rachek et al., 2015; Rimal et al., 2017). Furthermore, the GEp2gamma Collaboration at JLab (Meziane et al., 2011) performed a pioneering measurement of the deviation from the OPE prediction for both double-polarization components (P_x and P_z) of the $\vec{e} p \to e \vec{p}$ process at $Q^2 = 2.5$ GeV^2. While for P_x the TPE corrections were found to be negligible, for P_z a deviation from the OPE result was found at the 4σ level at $\epsilon = 0.8$ (Meziane et al., 2011). In combination with the unpolarized data, these measurements of the ϵ dependence of both double-polarization observables in the $\vec{e} p \to e \vec{p}$ process at a fixed value of Q^2 were used by Guttmann et al. (2011) to provide a first disentanglement of the three TPE amplitudes describing elastic e-p scattering for massless electrons, as given by Eq. (53).

While the TPE effects have been shown by experiments to be of the size needed to bring the form factor ratio results from unpolarized measurements closer to those from the recoil polarization experiments, further quantitative studies are needed to reach a conclusive statement, especially in the larger Q^2 range. On the theoretical side, various dispersion theoretical approaches have been developed in recent years; see Borisyuk and Kobushkin (2015), Tomalak, Pasquini, and Vanderhaeghen (2017b), and Ahmed, Blunden, and Melnitchouk (2020) and older references therein, which relate the TPE amplitudes at intermediate Q^2 values to empirical input on the electromagnetic structure of the nucleon and its excitations. At large Q^2 approaches based on perturbative QCD have been proposed (Chen et al., 2004; Borisyuk and Kobushkin, 2009; Kivel and Vanderhaeghen, 2013, 2009). Further experiments investigating the TPE effect at larger values of Q^2 will be highly desirable to further test and constrain the TPE model descriptions.

In the low Q^2 region, the TPE effect can be predicted with less model dependence (Hill et al., 2013; Tomalak, Pasquini, and Vanderhaeghen, 2017a). Especially in the forward angular range relevant to the proton electric charge radius

determination from elastic e-p scattering, it is found to be understood at the level of precision of current experiments. The TPE effect increases for the backward angular range, where a better understanding is required for improving the extraction of the proton magnetic radius.

G. Radiative corrections in electron scattering

In addition to the TPE correction corresponding to two hard photons in Fig. 9, another important aspect associated with lepton scattering, especially with electron scattering, is the so-called radiative correction (RC) effect on the OPE picture. RC refers to effects from various types of radiation and soft-photon exchanges in electron scattering that need to be corrected before one can extract information such as the proton electric and magnetic form factors defined in the OPE picture. Examples include the initial-state electron radiating a photon prior to the scattering and the final-state electron radiating a photon before it is detected in the detector. Similar pictures can be applied to the proton side, although such radiative effects are suppressed because the proton mass is significantly larger than that of an electron. A different way to look at the proton side is that such a RC effect in principle can be included in the definition of the proton electric and magnetic form factors. Another important RC contribution is due to the QED vacuum polarization, which refers to the fact that a virtual photon can fluctuate into an electron-positron pair before it is absorbed, and the vertex correction on electron and proton sides. Furthermore, the radiative corrections conventionally also include a part of the TPE correction, in which one of the photons in the box diagram of Fig. 9 has a soft four-momentum. These are simply examples of leading-order RC contributions, which are at the next-to-leading order compared to the leading-order OPE in electron-proton scattering. Two classic review articles on this subject still widely used and cited are by Mo and Tsai (1969) and by Maximon (1969). In recent years, there has been renewed interest in performing and pushing the state-of-the-art calculations on RC for various lepton-nucleon-scattering processes due not only to the demand from the experimental side to improve precision but also the need for other processes such as semi-inclusive deep inelastic scattering to probe partonic three-dimensional momentum distributions and fragmentation functions. The effect of RC is also experiment specific; we refer the interested reader to specific experiments that are discussed in this review for further details.

H. The extraction of the proton charge radius from the proton electric form factor

The proton charge radius can be extracted from the experimentally determined proton electric form factor values. According to Eq. (36), the proton rms charge radius is directly related to the G_{Ep} Q^2 slope at $Q^2 = 0$. Experimentally this is not possible due to the requirement of conducting electron-proton elastic scattering at $0°$ scattering angle. Therefore, while it is important to reach as low a Q^2 value as possible, it is inevitable that one needs to extrapolate from the measured values of Q^2 down to zero. Furthermore, it is also important for any scattering experiment to cover a sufficient range of Q^2,

i.e., to have good leverage in Q^2 coverage. When Q^2 is sufficiently close to zero, the slope becomes rather flat because G_E would converge to 1, which is simply the net charge of the proton, as expected. Therefore, it is important to experimentally cover a Q^2 range in which one can capture whatever a Q^2-dependence nature calls for, and at the same time still be as close to $Q^2 = 0$ as practically possible.

Given the aforementioned limitations, it is important to develop ways that allow for a robust extraction of the proton charge radius. Such a study was carried out by Yan et al. (2018). We describe this study later. Pseudodatasets on the proton electric form factor are generated for a particular experiment or a planned measurement according to various proton electromagnetic form factor parametrizations and models in the literature. These parametrizations and models generally describe the existing data on the proton form factors well. One then smears the generated pseudodatasets according to the experimental resolutions and any other relevant experimental aspects, such as the statistical and systematic uncertainties. The method for taking into account the experimental systematic uncertainties is elaborate; we refer interested readers to the original paper by Yan et al. (2018) for more details. One then fits the smeared datasets to various functional forms and extracts for each functional form the corresponding proton charge radius value r_{Ep} and its uncertainty δr_{Ep}. The bias is defined as the difference between the input r_{Ep} value from the parametrization or model used to generate the pseudodataset in the first place and the r_{Ep} obtained from the fit. The goodness of a fit is to consider both the bias and the variance from the fit by using the root-mean-square error (RMSE) defined as RMSE $= \sqrt{\text{bias}^2 + \sigma^2}$.

The functional forms studied by Yan et al. (2018) include monopole, dipole, Gaussian, and multiparameter polynomial expansions of Q^2, the multiparameter rational function of Q^2, the continuous fractional (CF) expansion of Q^2, and also the multiparameter polynomial expansion of z, which is defined as

$$z = \frac{\sqrt{t_{\text{cut}} + Q^2} - \sqrt{t_{\text{cut}} - t_0}}{\sqrt{t_{\text{cut}} + Q^2} + \sqrt{t_{\text{cut}} - t_0}}, \tag{54}$$

where $t_{\text{cut}} = 4m_\pi^2$ corresponds to the threshold for the lowest 2π intermediate state in the timelike region, with m_π the mass of π^0 and t_0 a free parameter set to zero by Yan et al. (2018). Thus, the full functional form is expressed as

$$f_{\text{poly}z}(Q^2) = p_0 G_E(Q^2) = p_0 \left(1 + \sum_{i=1}^{N} p_i z^i \right). \tag{55}$$

The CF expansion form is expressed as

$$f_{\text{CF}}(Q^2) = p_0 G_E(Q^2)$$
$$= p_0 \frac{1}{1 + (p_1 Q^2 / \{1 + [p_2 Q^2/(1 + \cdots)]\})} \tag{56}$$

and was previously used by Hill and Paz (2010) and Griffioen, Carlson, and Maddox (2016) to extract the proton charge radius from proton electric form factor values.

The multiparameter rational function of Q^2 is written as

$$f_{\text{rational}}(Q^2) = p_0 G_E(Q^2) = p_0 \frac{1 + \sum_{i=1}^{N} p_i^{(a)} Q^{2i}}{1 + \sum_{j=1}^{M} p_j^{(b)} Q^{2j}}. \quad (57)$$

In all these functional forms of Eqs. (55)–(57), the p_0 is a floating normalization parameter. For the proton charge radius (PRad) experiment (Xiong *et al.*, 2019) in its entire data range, the study found that the $(N = M = 1) = (1, 1)$ rational function, the two-parameter continued fraction, and the second-order polynomial expansion in z can all extract the proton charge radius in a robust way with a small variance independent of the model or parametrization used for generating the pseudodata. The published r_{Ep} result (Xiong *et al.*, 2019) from the PRad experiment is based on fits to the rational $(1, 1)$ function. While Yan *et al.* (2018) presented the case study for the PRad experiment, the approach can be applied to any lepton-scattering experiment to extract the proton charge radius.

IV. ATOMIC HYDROGEN SPECTROSCOPY

The proton charge radius is an important input to QED calculations of bound states such as ordinary atomic hydrogen and muonic hydrogen. High-precision spectroscopic measurements, combined with state-of-the-art QED calculations, can determine the proton charge radius. In this section, we provide a discussion and focus on aspects most relevant to the finite size of the proton due to our interest in the determination of the proton charge radius. We closely follow the review by Eides, Grotch, and Shelyuto (2001), to which we refer for a comprehensive discussion of the QED calculations, including various higher-order effects.

The energy levels for one-lepton atoms can be obtained in the first approximation by solving the nonrelativistic Schrödinger equation for an electron in the field of an infinitely heavy Coulomb center with a charge Z in units of proton charge. The energy levels are written as

$$E_n = -\frac{m(Z\alpha)^2}{2n^2}, \quad (58)$$

where $n = 1, 2, 3, \ldots$ is the principal quantum number, α is the fine-structure constant, and m is the mass of the lepton. Considering the Coulomb source to still be infinitely heavy and solving the Dirac equation for a lepton in such a Coulomb field, one obtains the following Dirac spectrum:

$$E_{nj} = mf(n, j), \quad (59)$$

where

$$f(n, j) = \left[1 + \frac{(Z\alpha)^2}{[\sqrt{(j + 1/2)^2 - (Z\alpha)^2} + n - j - 1/2]^2}\right]^{-1/2}$$

$$\approx 1 - \frac{(Z\alpha)^2}{2n^2} - \frac{(Z\alpha)^4}{2n^3}\left(\frac{1}{j + 1/2} - \frac{3}{4n}\right) - \frac{(Z\alpha)^6}{8n^3}\left[\frac{1}{(j + 1/2)^3} + \frac{3}{n(j + 1/2)^2} + \frac{5}{2n^3} - \frac{6}{n^2(j + 1/2)}\right] + \cdots, \quad (60)$$

where $j = 1/2, 3/2, \ldots, n - 1/2$ is the total angular momentum of the state. Compared with the nonrelativistic Schrödinger spectrum, where all levels with the same n are degenerate, the energy levels in the Dirac spectrum with the same principal quantum number n but different j are no longer degenerate. However, energy levels with the same n and j but different $l = j \pm 1/2$ remain degenerate. Such degeneracy is lifted when one takes into account the finite size of the proton, recoil contributions, and most importantly the QED loop corrections, where the corresponding energy shifts are called the Lamb shifts. Details on calculating the QED radiative corrections, recoil, and radiative-recoil corrections were given by Eides, Grotch, and Shelyuto (2001).

To follow we review the leading relativistic corrections with exact mass dependence in the external field approximation following Eides, Grotch, and Shelyuto (2001). For a nonrelativistic system of two particles with Coulomb interaction such as a hydrogen atom, the Hamiltonian in its center-of-mass system can be written as

$$H_0 = \frac{\mathbf{p}^2}{2m} + \frac{\mathbf{p}^2}{2M} - \frac{Z\alpha}{r}, \quad (61)$$

where $\mathbf{p}$ is the momentum, in the case of hydrogen (muonic hydrogen) $Z = 1$, and m and M are the masses of the electron (muon) and the proton, respectively. In the remainder of this section, we focus on hydrogenlike atoms only. For a nonrelativistic loosely bound system such as a hydrogen atom, expansions over α^2 correspond to expansions over v^2/c^2. Therefore, an effective Hamiltonian including terms of the first order in v^2/c^2 would provide proper corrections of relative order α^2 to the nonrelativistic energy levels. Breit (1929, 1930, 1932) proposed such a potential realizing that all corrections to the nonrelativistic two-particle Hamiltonian of the first order in v^2/c^2 can be written as the sum of the free relativistic Hamiltonian of each of the particles and the relativistic one-photon exchange between the two. Barker and Glover (1955) derived the following Breit potential from the one-photon-exchange amplitude using the Foldy-Wouthuysen transformation (Foldy and Wouthuysen, 1950):

$$V_{\text{Br}} = \frac{\pi\alpha}{2}\left(\frac{1}{m^2} + \frac{1}{M^2}\right)\delta^3(\mathbf{r}) - \frac{\alpha}{2mMr}\left(\mathbf{p}^2 + \frac{\mathbf{r}(\mathbf{r} \cdot \mathbf{p}) \cdot \mathbf{p}}{r^2}\right)$$

$$+ \frac{\alpha}{r^3}\left(\frac{1}{4m^2} + \frac{1}{2mM}\right)[\mathbf{r} \times \mathbf{p}] \cdot \vec{\sigma}. \quad (62)$$

In Eq. (62), the hyperfine structure is not considered; i.e., terms that depend on the proton spin are omitted. Corrections

to the energy levels up to order α^4 can be calculated from the total Breit Hamiltonian of $H_{\rm Br} = H_0 + V_{\rm Br}$, where the interaction potential is the sum of the Coulomb and the Breit potential. These corrections are simply the first-order matrix elements of the Breit interaction between the eigenfunctions of the Coulomb Hamiltonian H_0, and the result is

$$E_{nj}^{\rm tot} = (m + M) - \frac{m_r \alpha^2}{2n^2} - \frac{m_r \alpha^4}{2n^3} \left(\frac{1}{j + 1/2} - \frac{3}{4n} + \frac{m_r}{4n(m + M)} \right) + \frac{\alpha^4 m_r^3}{2n^3 M^2} \left(\frac{1}{j + 1/2} - \frac{1}{l + 1/2} \right)(1 - \delta_{l0}),$$ (63)

where $m_r = mM/(m + M)$ is the reduced mass of the hydrogenlike atom. One can see that the last term in Eq. (63) breaks the degeneracy in the Dirac spectrum between states with the same j and $l = j \pm 1/2$ and contributes to the classical Lamb shift defined as $E(2P_{1/2}) - E(2S_{1/2})$. However, owing to the smallness of the electron-to-proton mass ratio, the contribution of this term is extremely small in the hydrogen case and the leading contribution to the Lamb shift is the QED radiative correction. Figure 10 shows the hydrogen $1S$, $2S$, and $2P$ energy levels.

In the discussion thus far, the proton has been treated as a pointlike charge. Equation (3) provides the photon-proton vertex operator involving the Dirac (F_1) and Pauli (F_2) form factors of the proton. Calculating the finite size contribution to the hydrogen atom energy levels amounts to evaluating the zero component of Eq. (3) between nucleon spinors, normalized as $N^\dagger N = 1$. An elementary calculation yields the spin-independent term at low-momentum transfer $\mathbf{q} \equiv \mathbf{p}' - \mathbf{p}$ as (Eides, Grotch, and Shelyuto, 2001) [see Miller (2019) for an explicit derivation]
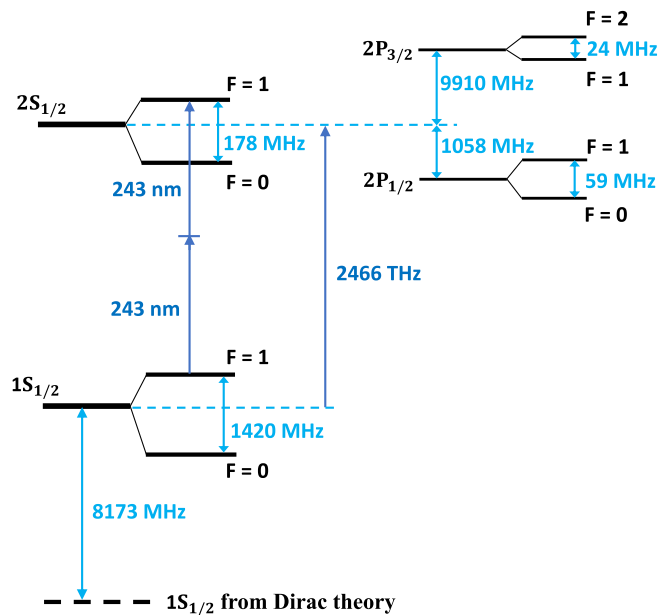

FIG. 10. Hydrogen $1S$, $2S$, and $2P$ energy levels. From Jingyi Zhou.

$$N(p', \lambda)\Gamma^0 N(p, \lambda) = \left(1 - \frac{\mathbf{q}^2}{8M^2} \right) G_E(-\mathbf{q}^2) + \mathcal{O}\left(\frac{1}{M^4} \right)$$

$$\approx 1 - \mathbf{q}^2 \left[\frac{1}{8M^2} + \frac{1}{6}\langle r_{Ep}^2 \rangle \right],$$ (64)

where on the last line we have used the low-momentum expansion of the proton electric form factor G_E in terms of the proton charge radius $\langle r_{Ep}^2 \rangle$ defined in Eq. (36). For a pointlike proton, the only term that survives in Eq. (64) is the first term in the square brackets, which leads to the well-known local Darwin term in the lepton-proton interaction (Barker and Glover, 1955) that gives rise to the term proportional to δ_{l0} in Eq. (63). Note that the leading relativistic correction factor in front of G_E in Eq. (64) is the same as the one appearing in Eq. (7). The established convention is to not include it in the definition of G_E but to instead include it separately. Therefore, the leading nuclear (proton) structure contribution to the energy shift is determined by the slope of the conventionally defined nuclear (proton) form factor G_E. The corresponding perturbative potential that corrects the Coulomb potential of a point charge to account for the finite proton size is therefore given by (Eides, Grotch, and Shelyuto, 2001)

$$\delta V_{\rm fin \, size} = \frac{2\pi\alpha}{3} \langle r_{Ep}^2 \rangle.$$ (65)

The associated energy level shift is then

$$\Delta E_{\rm fin \, size} = \frac{2\pi\alpha}{3} \langle r_{Ep}^2 \rangle |\psi_{nl}(0)|^2$$

$$= \frac{2\alpha^4}{3n^3} m_r^3 \langle r_{Ep}^2 \rangle \delta_{l0}.$$ (66)

One notices from Eq. (66) that the radius entering the finite size correction to the S levels of the hydrogen atom is the proton charge radius, obtained from the form factor G_E as measured in electron-proton-scattering experiments. This consistency between the proton charge radius determined from spectroscopic experiments of hydrogenlike atoms and electron-scattering experiments was also recently emphasized by Miller (2019).

While the Lamb shift of hydrogenlike atoms is dominated by the QED radiative effects of the lepton, the contribution from the proton charge radius is the leading term due to the finite size of the proton. By measuring Lamb shifts or other transitions between energy levels involving at least one S state of hydrogenlike atoms precisely and utilizing state-of-the-art QED calculations, one can determine the proton charge radius value. In the case of muonic hydrogen, the proton charge radius effect is 6.4×10^6 times larger than that of ordinary hydrogen atoms for the same nS level due to the m_r^3 dependence. For the $2P - 2S$ Lamb shift in muonic hydrogen, the term due to the proton charge radius amounts to around -3.7 meV and contributes about 2% of the overall Lamb shift (Eides, Grotch, and Shelyuto, 2001). This large relative contribution is an important reason why muonic hydrogen spectroscopic measurements are significantly more precise in

extracting the proton charge radius than those using ordinary hydrogen atoms.

To extract the proton radius from muonic hydrogen spectroscopic measurements accurately, it is important to also calculate the proton structure corrections of next order in α, i.e., $\mathcal{O}(\alpha^5)$. These proton structure corrections, which arise from the TPE diagram shown in Fig. 11, in which both photons in the loop carry the same four-momentum, are known as the polarizability correction. They have been evaluated using different approaches: chiral effective field theory [see Hagelstein, Miskimen, and Pascalutsa (2016) and references therein for a review of the ongoing activity in this field], within nonrelativistic QED (Pineda, 2003; Hill and Paz, 2011; Hill et al., 2013; Dye, Matthew Gonderinger, and Paz, 2016), or by connecting them model independently to other data through dispersive frameworks (Pachucki, 1999; Carlson and Vanderhaeghen, 2011; Birse and McGovern, 2012).

The nth S-level shift in the muonic hydrogen spectrum due to TPE is related to the spin-independent forward double virtual Compton amplitudes as

$$\Delta E_{\text{TPE}}(nS) = 8\pi e^2 m\phi_n^2 \frac{1}{i} \int_{-\infty}^{\infty} \frac{d\nu}{2\pi} \int \frac{d^3\mathbf{q}}{(2\pi)^3} \frac{(Q^2 - 2\nu^2)T_1(\nu,Q^2) - (Q^2 + \nu^2)T_2(\nu,Q^2)}{Q^4(Q^4 - 4m^2\nu^2)}, \tag{67}$$

where $\phi_n^2 = 1/\pi n^3 a^3$ is the wave function at the origin and $a^{-1} = \alpha m_r$ is the inverse Bohr radius. Furthermore, T_1 and T_2 are the forward double virtual Compton amplitudes that are complex functions of photon energy ν and photon virtuality Q^2. The optical theorem relates the imaginary parts of T_1 and T_2 to the two unpolarized structure functions of inclusive electron-nucleon scattering as

$$\text{Im}T_1(\nu, Q^2) = \frac{e^2}{4M} F_1(x, Q^2),$$

$$\text{Im}T_2(\nu, Q^2) = \frac{e^2}{4\nu} F_2(x, Q^2), \tag{68}$$

where $x \equiv Q^2/2M\nu$ and F_1, F_2 are the conventionally defined structure functions parametrizing inclusive electron-nucleon scattering.

The TPE contribution to the hydrogen spectrum can be separated into two distinct contributions. First, there is a Born contribution that corresponds to the nucleon intermediate state in Fig. 11 and depends solely on the elastic nucleon Dirac and Pauli form factors. Second, there is a polarizability contribution corresponding to all non-Born contributions to T_1 and T_2 that is denoted by $\bar{T}_i \equiv T_i - T_i^{\text{Born}}$, which depends on the excitation spectrum of the nucleon.

The polarizability effect on the hydrogen spectrum can be further split into the following contribution of the subtraction function $\bar{T}_1(0, Q^2)$ (Carlson and Vanderhaeghen, 2011):

$$\Delta E^{\text{subtr}}(nS) = \frac{2e^2 m\phi_n^2}{\pi} \int_0^{\infty} \frac{dQ}{Q^3} \frac{v_l + 2}{(1 + v_l)^2} \bar{T}_1(0, Q^2), \tag{69}$$

with $v_l = \sqrt{1 + 4m^2/Q^2}$ and the following contributions of the inelastic structure functions (Carlson and Vanderhaeghen, 2011; Hagelstein, Miskimen, and Pascalutsa, 2016):

$$\Delta E^{\text{inel}}(nS) = -32\alpha^2 M m\phi_n^2 \int_0^{\infty} \frac{dQ}{Q^5} \int_0^{x_0} dx \frac{1}{(1 + v_l)(1 + \sqrt{1 + x^2\tau^{-1}})}$$
$$\times \left\{ \left[1 + \frac{v_l\sqrt{1 + x^2\tau^{-1}}}{v_l + \sqrt{1 + x^2\tau^{-1}}} \right] F_2(x, Q^2) + \frac{2x}{(1 + v_l)(1 + \sqrt{1 + x^2\tau^{-1}})} \left[2 + \frac{3 + v_l\sqrt{1 + x^2\tau^{-1}}}{v_l + \sqrt{1 + x^2\tau^{-1}}} \right] F_1(x, Q^2) \right\}, \tag{70}$$

with τ the same as in Eq. (42) and x_0 the πN inelastic threshold in the hadronic blob in Fig. 11.

Table III shows the TPE corrections due to the inelastic structure functions estimate of Carlson and Vanderhaeghen
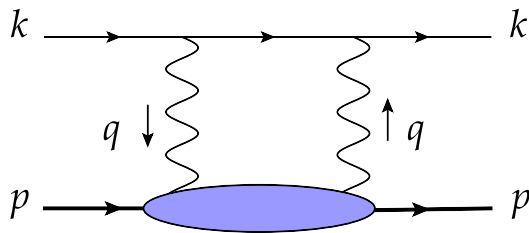

FIG. 11. The box diagram for the $\mathcal{O}(\alpha^5)$ corrections to $l = 0$ energy levels in muonic hydrogen. The blob denotes all possible hadronic intermediate states.

(2011) and resulting from the subtraction-function estimate of Birse and McGovern (2012), both of which are currently used in estimating the total polarizability contribution to the $2S$ level in muonic hydrogen analyses (Antognini, Kottmann et al., 2013). The estimate of Birse and McGovern (2012) assumes a dipole ansatz for $\bar{T}_1(0, Q^2)/Q^2$ and constrains the mass parameter by a heavy-baryon chiral perturbation theory (HBChPT) calculation to fourth order in the chiral expansion for the Q^4 term in $\bar{T}_1(0, Q^2)$. We compare these results with the leading-order (LO) BChPT analysis of Alarcón, Lensky, and Pascalutsa (2014), a next-to-leading-order (NLO) baryon chiral perturbation theory (BChPT) analysis that includes the Δ-pole contribution (Hagelstein, 2017; Lensky et al., 2018), and with the NLO HBChPT analysis of Peset and Pineda (2014). One notices that the BChPT result that includes the Δ pole is in good agreement with the dispersion relation (DR)

TABLE III. TPE corrections to the $2S$ level in muonic hydrogen. All values are given in μeV. The first two rows are the dispersive (ΔE^{inel}) and subtraction-function (ΔE^{subtr}) contributions. The sum of the two yields the total polarizability contribution ΔE^{pol}.

	DR + HBChPT	BChPT (LO) (Alarcón, Lensky, and Pascalutsa, 2014)	BChPT (LO + Δ) (Hagelstein, 2017; Lensky et al., 2018)	HBChPT (NLO) (Peset and Pineda, 2014)
ΔE^{inel}	-12.7 ± 0.5 (Carlson and Vanderhaeghen, 2011)	-5.2	-11.8	$\cdots$
ΔE^{subtr}	4.2 ± 1.0 (Birse and McGovern, 2012)	-3.0	4.6	$\cdots$
ΔE^{pol}	-8.5 ± 1.1 (Antognini, Kottmann et al., 2013)	$-8.2^{+1.2}_{-2.5}$	$-7.2^{+1.2}_{-2.5}$	-26.2 ± 10.0

estimate for the inelastic contribution and with the estimate of Birse and McGovern (2012) for the subtraction-function contribution. It is also interesting to note that, although the Δ pole contributes sizably to both terms, these contributions come with opposite signs, resulting in a small total polarizability contribution due to the Δ pole, and a total result close to the LO BChPT estimate. The NLO HBChPT estimate (Peset and Pineda, 2014), shown in the last column of Table III, comes with a larger error estimate, and its value is larger in magnitude, deviating by about 2σ from the BChPT and DR estimates. It was noticed, however (Peset and Pineda, 2014), that upon adding the nucleon Born term contributions it yields a total TPE result that is similar in size to the DR and BChPT results.

Recall that the Lamb shift is the difference between the shifts of the $2P$ and $2S$ levels; the TPE contribution to the former is negligible, and the TPE contribution to the Lamb shift is thus simply $-\Delta E_{\text{TPE}}(2S)$.

Using dispersion relations, with input from forward proton structure functions and a subtraction function, the value for the $\mathcal{O}(\alpha^5)$ TPE proton structure correction to the $2P - 2S$ Lamb shift that is presently used in the extraction of the proton charge radius from the muonic hydrogen Lamb shift measurements, as discussed in Sec. VI, is given by (Carlson and Vanderhaeghen, 2011; Birse and McGovern, 2012; Antognini, Kottmann et al., 2013)

$$\Delta E_{\text{TPE}}(2P - 2S) = 0.0332(20) \text{ meV}. \tag{71}$$

V. MODERN LEPTON-SCATTERING EXPERIMENTS

A. Mainz 2010

Bernauer et al. (2010) carried out an unpolarized electron-proton elastic-scattering experiment at the Mainz accelerator facility MAMI and extracted the proton charge and the magnetic radii. The experiment utilized electron beam energies up to 855 (180, 315, 450, 585, 720, and 855) MeV and three high-resolution magnetic spectrometers, with one serving as a relative luminosity monitor at a fixed laboratory angle. The other two spectrometers were moved as a function of the electron-scattering angle during the experiment to provide the kinematic coverage and also redundancy in the coverage. The targets used in this experiment were 2- and 5-cm-long cells filled with liquid hydrogen. The top image in Fig. 12 shows the schematics of the three-spectrometer setup for this experiment, and a photo of the setup is shown beneath, where the red, blue, and green apparatuses are spectrometers A, B, and C, respectively.

In total the experiment measured over 1400 differential cross sections covering a Q^2 range of 0.004 to 1 $(\text{GeV}/c)^2$ and achieved a statistical precision better than 0.2% for these cross-section measurements. To extract the proton electric and
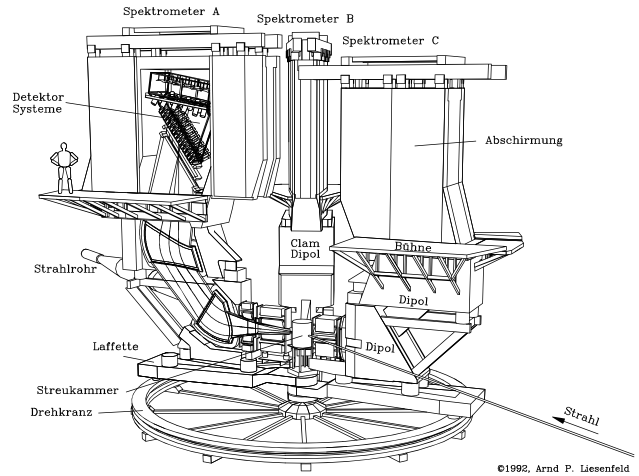

FIG. 12. Top image: schematics of the three-spectrometer setup of the A1 experiment at Mainz. From Blomqvist et al., 1998. Bottom: photo showing spectrometers A, B, and C in red, blue, and green, respectively. The electron beam progresses from right to left. From Weis, 2003.

magnetic form factors, least square fits to models of G_{Ep} and G_{Mp} were carried out on the 1400 cross-section data points, covering all Q^2 and scattering angles of the experiment. The proton form factors up to $Q^2 = 0.6$ $(\text{GeV}/c)^2$ were extracted from this approach. Bernauer *et al.* (2010) carried out detailed studies of model dependence in extracting the proton form factors using various form factor models and parametrizations. The experiment extracted the following for the proton charge and magnetic radii:

$$\langle r_{Ep}^2 \rangle^{1/2} = 0.879(5)_{\text{stat}}(4)_{\text{syst}}(2)_{\text{model}}(4)_{\text{group}} \text{ fm},$$
$$\langle r_{Mp}^2 \rangle^{1/2} = 0.777(13)_{\text{stat}}(9)_{\text{syst}}(5)_{\text{model}}(2)_{\text{group}} \text{ fm},$$

where the uncertainty labeled "group" is assigned to account for the difference between the radius values obtained using two groups of models for the form factors in the fits, namely, the spline and the polynomial groups. Details were given by Bernauer *et al.* (2010, 2014). The result on the proton charge radius from this electron-scattering experiment was consistent with the CODATA-2006 (Mohr, Taylor, and Newell, 2008) value at the time of publication but 5 standard deviations larger than the value from the muonic hydrogen Lamb shift measurement (Pohl *et al.*, 2010). The magnetic radius obtained is smaller than those from previous fits of electron-scattering data but consistent with the result of 0.778(29) fm (Volotka *et al.*, 2005) from hyperfine splitting in hydrogen.

B. JLab recoil polarization experiment

The Jefferson Lab experiment E08-007 (Zhan *et al.*, 2011) carried out a high-precision measurement of the polarization transfer from electron-proton elastic scattering using a recoil proton polarimeter covering a momentum transfer squared Q^2 region between 0.3 and 0.7 $(\text{GeV}/c)^2$. The experiment was performed in Hall A and utilized a longitudinally polarized electron beam with polarization higher than 80% at 1.2 GeV, beam currents between 4 and 15 μA, and a 6-cm-long unpolarized liquid hydrogen target. There were two high-resolution magnetic spectrometers (HRSs) in Hall A placed on each side of the electron beam line. In E08-007, the recoil proton was detected in the left HRS, with its polarization measured using a focal-plane polarimeter, in coincidence with the scattered electron that was measured in a large acceptance spectrometer ("BigBite"). The experiment extracted the proton electric to magnetic form factor ratio $\mu_p G_{Ep}/G_{Mp}$ with a total uncertainty of about 1%. When these results were put together with a few other proton form factor ratio measurements from Jefferson Lab (Paolone *et al.*, 2010; Puckett *et al.*, 2010; Ron *et al.*, 2011), a global fit of the proton form factors (Arrington, Melnitchouk, and Tjon, 2007) was updated. This updated global analysis did not include the Mainz data (Bernauer *et al.*, 2010) and gave the following values for the proton electric and the magnetic charge radii:

$$\langle r_{Ep}^2 \rangle^{1/2} = 0.875 \pm 0.010 \text{ fm},$$
$$\langle r_{Mp}^2 \rangle^{1/2} = 0.867 \pm 0.020 \text{ fm}.$$

The proton charge radius value from this updated global analysis is in excellent agreement with the value from the

Mainz electron-proton-scattering experiment (Bernauer *et al.*, 2010), and also with the CODATA-2006 value (Mohr, Taylor, and Newell, 2008), which is based mostly on ordinary hydrogen spectroscopic measurements. It is in disagreement with the muonic hydrogen result (Pohl *et al.*, 2010). The magnetic radius value from this global analysis is more than 5 standard deviations greater than the Mainz value (Bernauer *et al.*, 2010).

C. Mainz ISR measurements

Following the Mainz experiment by Bernauer *et al.* (2010), another electron-proton elastic-scattering experiment at Mainz was carried out using the same three-spectrometer setup, but lower values of Q^2 (0.001 to 0.004 GeV/c^2) were reached using the technique of initial-state radiation (ISR) (Mihovilovič *et al.*, 2017). For electron-scattering experiments, the lowest Q^2 value that is achievable is determined by the lowest electron beam energy the associated accelerator can deliver, and the most forward electron-scattering angle the corresponding detector can reach. The ISR technique overcomes such limits by utilizing the information within the radiative tail of the elastic peak. The technique works in the following way, as depicted by Fig. 13. The incoming electron can radiate a real photon before the scattering takes place. As a result, the corresponding Q^2 value for the *e-p* scattering would be lower than what is limited by the accelerator and the detector because the incident electron energy is lower than the original value delivered by the accelerator and before the initial-state radiation of the real photon caused by the incoming electron. This is the diagram labeled for Bethe and Heitler (BH-i) in Fig. 13. Such an ISR technique was proposed and used successfully in previous particle physics experiments (Arbuzov *et al.*, 1998; Aubert *et al.*, 2004). One of the challenges of such an ISR experiment is in separating
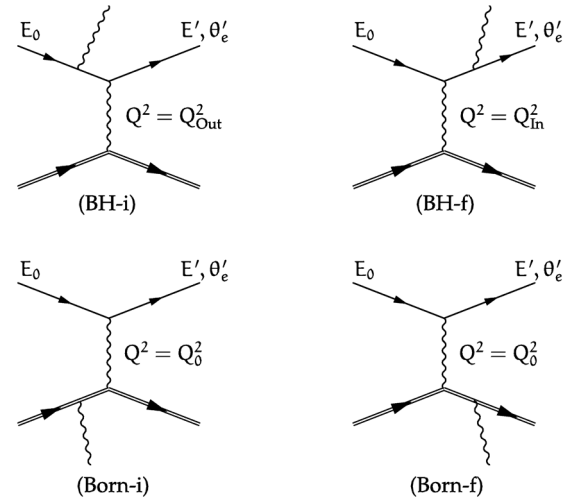

FIG. 13. Feynman diagrams showing electron-proton scattering with an electron or proton radiates a real photon in the initial state or final state. In the electron case, the two diagrams are labeled for Bethe and Heitler (BH-i and BH-f), while the diagrams for the proton are Born-i and Born-f, where i and f stand for the initial-state and final-state radiation, respectively. From Mihovilovič *et al.*, 2017.

the contribution from the diagram labeled (BH-f), where the scattered electron radiates a real photon, as only scattered electrons are measured (inclusive measurement). Furthermore, although contributions from diagrams involving the proton initial-state and final-state radiation are suppressed due to the proton mass, they need to be included, as they also contribute to the radiative tail of the elastic scattering, as well as to higher-order radiative effects. For details on how to account for these effects, see Mihovilovič *et al.* (2017), who extracted a proton charge radius value of $\langle r_{Ep}^2 \rangle^{1/2} = 0.810 \pm 0.035_{\text{stat}} \pm 0.074_{\text{syst}} \pm 0.003_{\text{model}}$ fm, with the last uncertainty accounting for higher moments in parametrizing the proton electric form factor. The A1 Collaboration reported a follow-up result through a comprehensive reinterpretation of the existing cross-section data from this first ISR e-p-scattering experiment by improving the description of the radiative tail. They obtained $\langle r_{Ep}^2 \rangle^{1/2} = 0.878 \pm 0.011_{\text{stat}} \pm 0.031_{\text{syst}} \pm 0.002_{\text{model}}$ fm with major improvements in both the statistical and systematic uncertainties; see Mihovilovič *et al.* (2021).

D. The PRad experiment at JLab

The PRad experiment (Xiong *et al.*, 2019) at Jefferson Lab was designed with a number of important points in mind: (i) the experiment differs from previous e-p-scattering experiments and therefore has different systematics, (ii) unprecedentedly low values of Q^2 are reached, (iii) emphasis is placed on the ability to precisely measure e-p elastic-scattering cross sections via accurate control of the integrated luminosity, and (iv) changes during the experiment and while taking data using a fixed experimental apparatus are minimized.

The PRad experiment innovated electron-scattering measurements in the following ways. Instead of using a magnetic spectrometer, which usually limits the forwardmost scattering angles due to its physical size, the PRad experiment used a two-dimensional large-area, granular, high-resolution electromagnetic calorimeter with a hole at the center for the electron beam to pass through. The novel design allows access to significantly smaller scattering angles ($\sim 0.7°$) than are found in experiments using magnetic spectrometers. To overcome major background issues associated with small-angle scattering, the PRad experiment used a window-less, cryogenically cooled, flowing hydrogen gas target. The internal target was a first for Jefferson Lab, giving the facility's electron beam unobstructed access to the window-less hydrogen target. To have excellent control of the integrated luminosity for the electron-proton elastic-scatter-ing cross-section measurements, Møller scattering, a well-known QED process, was used as a reference process and was measured simultaneously during the e-p scattering. Finally, to improve the scattering angle (Q^2) determination, a large plane of gas electron multiplier (GEM) detectors was used. The GEM detector used at PRad was the largest ever used in any experiment at the time.

The schematics of the PRad experiment are shown in Fig. 14, in which the electron beam progresses from left to right. PRad was the first experiment to complete its data taking in June 2016 after the Continuous Electron Beam Accelerator Facility (CEBAF) [consisting of a polarized electron source, an injector, and a pair of superconducting radio frequency (rf) linear accelerators] energy upgrade from 6 to 12 GeV at Jefferson Lab was completed. Two values of electron beam energies were used in the PRad experiment: 1.1 and 2.143 GeV. For the 1.1 GeV dataset, most of the data were obtained at a beam current of 15 nA, with the rest at 10 nA, while for the 2.143 GeV data the nominal beam current was 55 nA. To minimize the background from the air, the scattered electrons traveled through a two-stage vacuum chamber
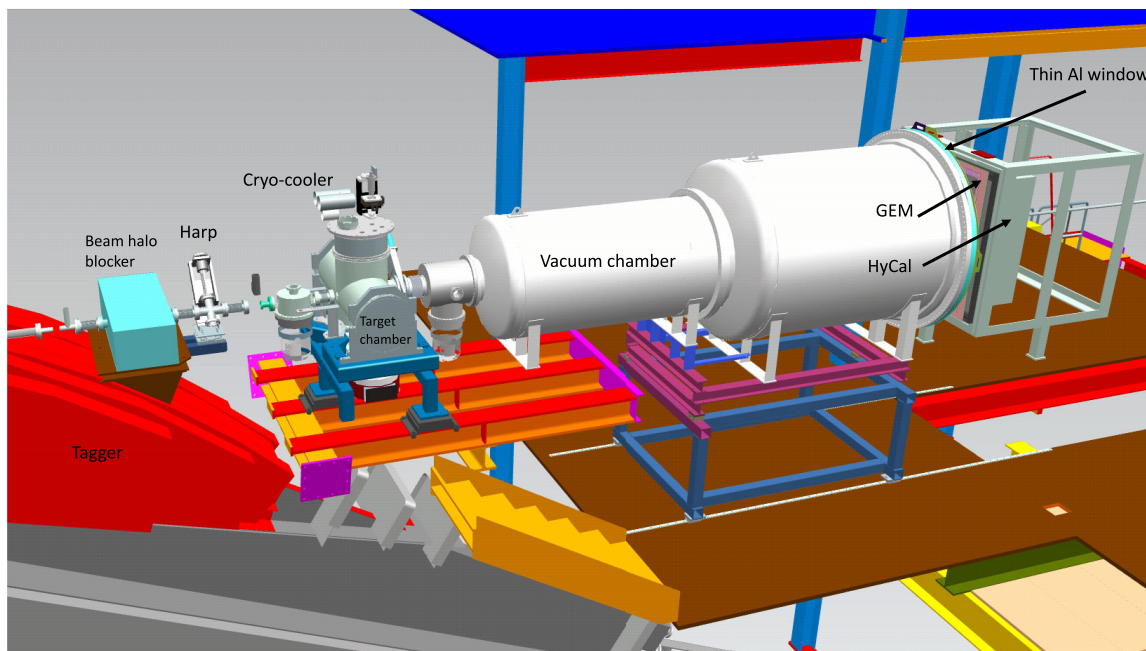

FIG. 14. Schematics of the PRad experiment in Hall B at Jefferson Lab. The electron beam progresses from left to right. From E. Pasyuk, J. Brock, K. Gnanvo, P. Hemler, D. Kashy, N. Liyanage, and G. Swift.
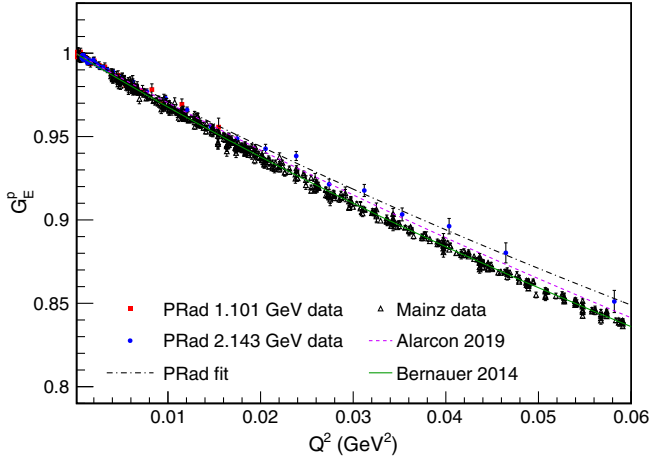
FIG. 15. The proton electric form factor G_E^p from the PRad experiment together with results from the Mainz experiment (Bernauer *et al.*, 2010; Bernauer, 2020) in the overlapping Q^2 region. Both datasets include statistical and systematic uncertainties; see the text. Two fits of the PRad data (Alarcón *et al.*, 2019; Xiong *et al.*, 2019) and a fit of the Mainz data (Bernauer *et al.*, 2014) are also shown. From Weizhi Xiong.

FIG. 16. The proton electric form factor G_E^p from the PRad experiment together with those from Hand, Miller, and Wilson (1963), Murphy, Shin, and Skopik (1974b), Simon *et al.* (1980), and Bernauer (2020) normalized to the standard dipole form in the overlapping Q^2 region, on linear scale. From Weizhi Xiong.

followed by the GEM detector and a hybrid electromagnetic calorimeter (HyCal), built originally for precision measurements of the neutral pion lifetime (Larin *et al.*, 2011, 2020). More details about the PRad target and the experimental setup were given by Xiong *et al.* (2019), Xiong (2020), and Pierce *et al.* (2021).

The proton electric form factor values in the Q^2 range of 2×10^{-4} to 0.06 (GeV/c)^2 have been extracted from the PRad experiment with statistical uncertainties of $\sim$0.2% at 1.1 GeV, and $\sim$0.15% at 2.143 GeV per data point, respectively. The systematic uncertainties range from $\sim$0.1% to 0.6% (relative) for the entire PRad dataset (Xiong, 2020). The PRad G_E^p results with statistical and systematic uncertainties combined in quadrature are presented in Fig. 15. The Mainz G_E^p results (Bernauer, 2020) extracted from the Mainz experiment (Bernauer *et al.*, 2010) including both the statistical and systematic uncertainties in the Q^2 overlapping region of these two experiments are shown in Fig. 15. Also shown are the fits of the PRad results (Alarcón *et al.*, 2019; Xiong *et al.*, 2019) and a fit of the Mainz data (Bernauer *et al.*, 2014). In Fig. 16, additional G_E^p data from Hand, Miller, and Wilson (1963), Murphy, Shin, and Skopik (1974b), and Simon *et al.* (1980) normalized to that of the standard dipole form are also shown. Other than the data from Hand, Miller, and Wilson (1963), which has rather larger uncertainties, the PRad results are systematically higher than other data in the higher end of the Q^2 range covered by the PRad experiment, specifically $\sim$0.03 (GeV/c)^2 and higher.

Yan *et al.* (2018) studied how to extract the proton charge radius in the low Q^2 region from the measured G_E^p values in a robust way and demonstrated that the rational $(1, 1)$ function defined in Eq. (57) is such a function and the best choice for the PRad data. Figure 17 shows fits using various rational functions of pseudodata generated with nine proton form factor models including the projected PRad statistical and systematic uncertainties. Apart from monopole, dipole, and
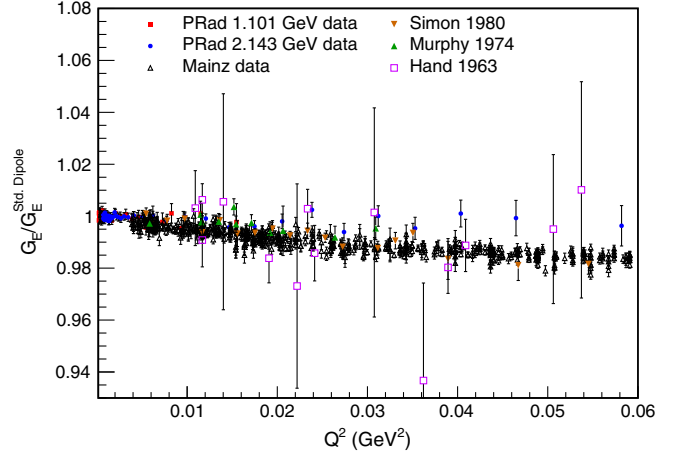
Gaussian functional forms, the proton form factor parametrizations and fits from Kelly (2004), Arrington, Melnitchouk, and Tjon (2007), Bernauer *et al.* (2014), Alarcón and Weiss (2018), and Ye *et al.* (2018) have been used. Additional details including fits of other functional forms were given by Yan *et al.* (2018). The PRad Collaboration adopted the rational $(1, 1)$ functional form to fit the data with two individual normalization parameters n_1 and n_2 corresponding to the two separate beam energy values for which the data were taken, while keeping the rest of the rational $(1, 1)$ parameters the same, i.e., $n_1[(1 + p_1 Q^2)/(1 + p_2 Q^2)]$ and $n_2[(1 + p_1 Q^2)/(1 + p_2 Q^2)]$. At $Q^2 = 0$, this normalization parameter is simply the proton charge, which should be 1. The results from the fit are given by

$$\langle r_{Ep}^2 \rangle^{1/2} = 0.831 \pm 0.007(\text{stat}) \pm 0.012(\text{syst}) \text{ fm},$$
$$n_1 = 1.0002 \pm 0.0002(\text{stat}) \pm 0.0020(\text{syst}),$$
$$n_2 = 0.9983 \pm 0.0002(\text{stat}) \pm 0.0013(\text{syst}), \quad (72)$$

showing that the two normalization values obtained are consistent with 1.

The PRad result for the proton charge radius is smaller than the two latest $\langle r_{Ep}^2 \rangle^{1/2}$ values extracted from electron-scattering experiments (Bernauer *et al.*, 2010; Zhan *et al.*, 2011) but consistent with the $\langle r_{Ep}^2 \rangle^{1/2}$ values from the muonic hydrogen spectroscopic measurements (Pohl *et al.*, 2010; Antognini *et al.*, 2013). While this result is also consistent with two recent hydrogen spectroscopic measurements (Beyer *et al.*, 2017; Bezginov *et al.*, 2019), it is not consistent with those of Fleurbaey *et al.* (2018). These most recent hydrogen spectroscopic measurements are discussed later.

Figure 18 shows the PRad result for the proton charge radius together with the recent results from the hydrogen spectroscopic measurements and the muonic hydrogen results. Also shown are the latest CODATA-2018 values (Tiesinga *et al.*, 2021), CODATA-2014 values (Mohr, Newell, and Taylor, 2016), results from Bernauer *et al.* (2010) and
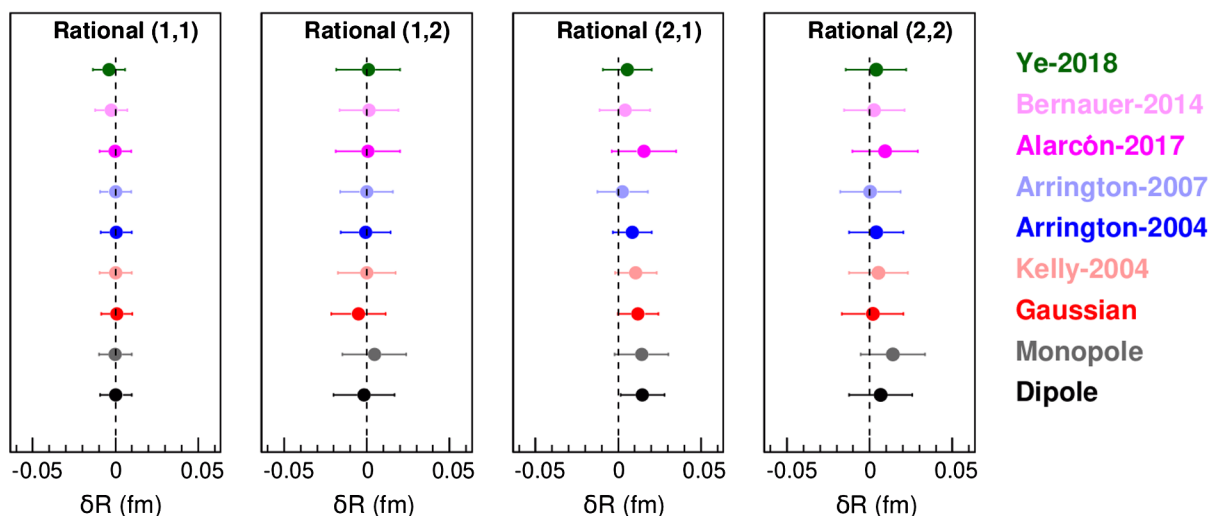
FIG. 17. Sample fits using rational functions of pseudodata generated with nine proton form factor models including the projected PRad statistical and systematic uncertainties. From Yan *et al.*, 2018.
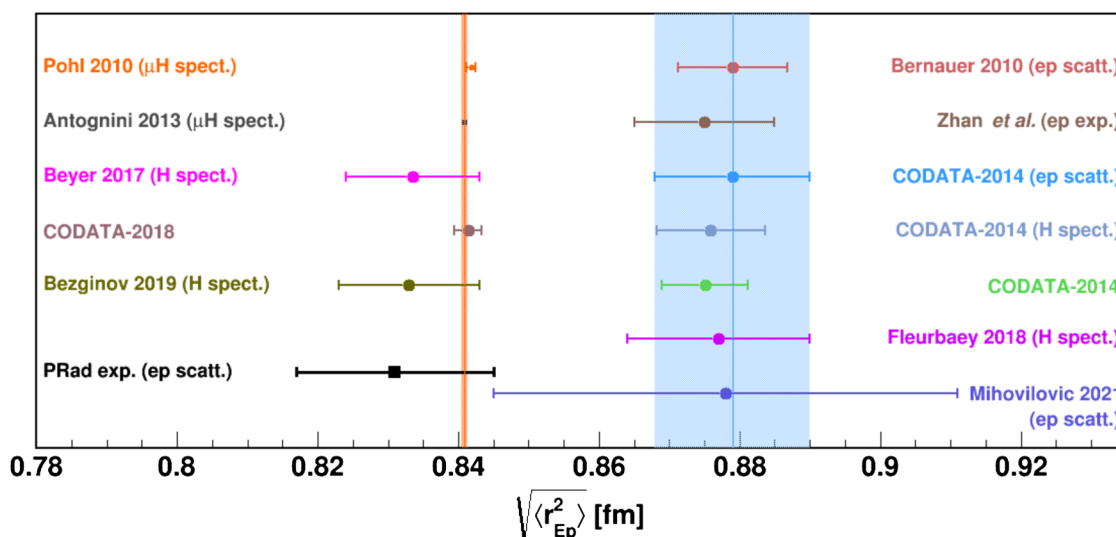

FIG. 18. The proton charge radius $\langle r_{Ep}^2 \rangle^{1/2}$ as extracted from electron-scattering and spectroscopic experiments since 2010 and before 2020 together with CODATA-2014 and CODATA-2018 recommended values. Note the reinterpreted result from the Mainz ISR experiment was scheduled for publication in 2021. From Jingyi Zhou.

Zhan *et al.* (2011), and also the result from the Mainz ISR experiment (Mihovilovič *et al.*, 2021). One interesting observation is that among the most precise measurements from hydrogen spectroscopic and electron-scattering measurements in recent years (Beyer *et al.*, 2017; Fleurbaey *et al.*, 2018; Bezginov *et al.*, 2019; Xiong *et al.*, 2019), three experiments reported a value that is smaller than the one from the muonic results, although they are all consistent within experimental uncertainties. Improving the precision of such measurements will be crucial to investigating whether there might be a substantiated difference between results from muonic versus electronic systems.

E. Proton charge radius from modern analyses of proton electric form factor data

In addition to new experiments, numerous analyses have been carried out in recent years in order to understand the

difference between the $\langle r_{Ep}^2 \rangle^{1/2}$ values determined from electron-scattering experiments, especially the modern precision electron-proton-scattering experiment at Mainz (Bernauer *et al.*, 2010), and the muonic hydrogen results (Pohl *et al.*, 2010; Antognini *et al.*, 2013). Some of these analyses obtain results consistent with the precise values from muonic hydrogen, while others are in agreement with larger values of r_{Ep}. We now describe some of these analyses.

Hill and Paz (2010) carried out a model-independent determination of the proton charge radius from electron scattering by first performing a conformal mapping of the domain of analyticity onto the unit circle in terms of $z(t, t_{\text{cut}}, t_0)$ defined in Eq. (54), where $t = q^2$, $t_{\text{cut}} = 4m_\pi^2$, and t_0 is a free parameter mapping onto $z = 0$. The form factor $G_E(q^2)$ can then be written as a function of z, where a z expansion can be carried out with the advantage that higher-order terms in z are suppressed. Using electron-proton

scattering datasets, a proton charge radius value of $\langle r_{Ep}^2 \rangle^{1/2} = 0.870 \pm 0.023 \pm 0.012$ fm is obtained; see Hill and Paz (2010) for details.

Lorenz, Hammer, and Meissner (2012) analyzed the 2010 Mainz data using a dispersive approach to ensure analyticity and unitarity in the description of the nucleon form factors. In their analysis they included the world data on the proton and also the neutron, obtaining a charge radius value of $\langle r_{Ep}^2 \rangle^{1/2} = 0.84 \pm 0.01$ fm consistent with the result from muonic hydrogen. Lorenz and Meissner (2014) later also reanalyzed the Mainz data using a fit function based on conformal mapping and showed that the extracted value for the proton charge radius [with a larger statistical uncertainty than that from Bernauer et al. (2010)] is in agreement with the value from muonic hydrogen spectroscopic measurements, and also their previous dispersive analysis. Lorenz et al. (2015) calculated the TPE corrections to the electron-proton scattering and applied these corrections to the Mainz data (Bernauer et al., 2010). They also investigated the impact on the extraction of the proton form factors from the inclusion of physical constraints and the extraction of $\langle r_{Ep}^2 \rangle^{1/2}$ due to the enforcement of a realistic spectral function, which dominates the latter. Recently a further improvement of the dispersive description was presented by Lin, Hammer, and Meißner (2021). It used an improved two-pion continuum based on a Roy-Steiner analysis of pion-nucleon scattering (Hoferichter, de Elvira et al., 2016; Hoferichter, Kubis et al., 2016), resulting in the value $\langle r_{Ep}^2 \rangle^{1/2} = 0.838 \pm 0.005 \pm 0.004$ fm, where the first error is due to the fitting procedure and the second is from the spectral function.

Adamuscin, Dubnicka, and Dubnickova (20120 analyzed all nucleon electromagnetic form factor data using their unitary and analytic ten-resonance model of the nucleon electromagnetic structure in order to find the corresponding behavior of the proton electric form factor in the extended spacelike region. The nondipole behavior of G_{Ep} is found to have a zero at around $Q^2 = 13$ $(\mathrm{GeV}/c)^2$. The extracted proton radius from this global analysis is $\langle r_{Ep}^2 \rangle^{1/2} = 0.84894 \pm 0.0069$ fm.

The first analysis of the electron-proton elastic-scattering data based on Bayesian statistical methods was carried out by Graczyk and Juszczak (2014) and the most probable proton charge radius value was found to be $\langle r_{Ep}^2 \rangle^{1/2} = 0.899 \pm 0.003$ fm. This analysis was done by accounting for the TPE effect using a box diagram model, including nucleon and $\Delta(1232)$ states.

The effect of TPE corrections in extracting the proton charge radius was also studied in an earlier analysis of the electron-proton scattering data (Borisyuk, 2010). Using a dispersive formalism for the TPE for the nucleon elastic contribution, Borisyuk (2010) reported the value $\langle r_{Ep}^2 \rangle^{1/2} = 0.912 \pm 0.009(\mathrm{stat}) \pm 0.007(\mathrm{syst})$ fm.

Lee, Arrington, and Hill (2015) carried out a comprehensive global analysis of the world electron-proton elastic-scattering data with a focus on the Mainz measurements (Bernauer et al., 2010). This study involves enforcing model-independent constraints from form factor analyticity and systematic studies of possible systematic effects. The extracted proton radius from this improved analysis of the

Mainz data is $\langle r_{Ep}^2 \rangle^{1/2} = 0.895(20)$ fm, while $\langle r_{Ep}^2 \rangle^{1/2} = 0.916(24)$ fm was extracted by analyzing the world data without including the Mainz data. Arrington and Sick (2015) carried out a global examination of the elastic electron-proton-scattering data and recommended a proton charge radius value of $0.879(11)$ fm.

Griffioen, Carlson, and Maddox (2016) analyzed the Mainz dataset (Bernauer et al., 2010) using a continued fraction functional form to map the G_E, assuming that it is monotonically falling and inflectionless. They obtained a proton charge radius value of $0.840(16)$ fm, which is consistent with the mounic hydrogen result after rescaling different datasets on a level that is smaller than the original normalization uncertainties and also inflates the point-to-point systematic uncertainty by 15%.

A proton charge radius value consistent with muonic hydrogen results was also obtained by Higinbotham et al. (2016) from data analysis in the low-momentum transfer region from Mainz in the 1980s (Simon et al., 1980) and Saskatoon in 1974 (Murphy, Shin, and Skopik, 1974a, 1974b) using a stepwise regression of Maclaurin series and applying the F test and the Akaike information criterion. When the Mainz results on G_{Ep} are included (Bernauer et al., 2014), the same analysis favors a radius that is consistent with the muonic hydrogen results, although their result is more sensitive to the range of the data included in the analysis.

Horbatsch and Hessels (2016a) also analyzed the Mainz data (Bernauer et al., 2010) and obtained $\langle r_{Ep}^2 \rangle^{1/2}$ values ranging at least from 0.84 to 0.89 fm using two single-parameter form factor models, with one being a dipole form and the other a linear fit to a conformal-mapping variable.

Sick and Trautmann (2017) argued that the smaller values of $\langle r_{Ep}^2 \rangle^{1/2}$ from Griffioen, Carlson, and Maddox (2016), Higinbotham et al. (2016), and Horbatsch and Hessels (2016a) are due to the neglect of higher moments in these analyses. Kraus et al. (2014) found that fits of the proton charge form factor with truncated polynomials give values that are too small for the proton charge radius. In a later paper by Horbatsch, Hessels, and Pineda (2017), a $\langle r_{Ep}^2 \rangle^{1/2}$ value of $0.855(11)$ fm was obtained with the higher moments fixed to the values based on chiral perturbation theory.

Alarcón et al. (2019) used a new theoretical framework that combines chiral effective field theory and dispersion analysis. The behavior of the spacelike form factor in the finite Q^2 region correlates with its derivative at $Q^2 = 0$ due to the analyticity in the momentum transfer. In this approach, predictions for spacelike form factors are made with the proton charge radius as a free parameter. By comparing the predictions for different values of the proton radius with a descriptive global fit (Lee, Arrington, and Hill, 2015) of the spacelike form factor data, Alarcón et al. (2019) extracted a proton radius value of $0.844(7)$ fm that is consistent with the muonic hydrogen results. A more recent analysis by Alarcón, Higinbotham, and Weiss (2020) using the aforementioned method to extract both the proton magnetic and charge radius from the Mainz A1 data (Bernauer et al., 2010) obtained $\langle r_{Mp}^2 \rangle^{1/2} = 0.850 \pm 0.001(\mathrm{fit}\, 68\%) \pm 0.010\,(\mathrm{theory\ full\ range})$ fm, and $\langle r_{Ep}^2 \rangle^{1/2} = 0.842 \pm 0.002(\mathrm{fit}) \pm 0.010(\mathrm{theory})$ fm. Including

the PRad data (Xiong *et al.*, 2019) into their fit, they found no change in the extracted radius values within uncertainties.

Sick (2018) carried out a detailed study to reduce the model dependence associated with the required extrapolation in determining $(dG_E/dQ^2)(Q^2 = 0)$ to extract $\langle r_{Ep}^2 \rangle^{1/2}$. The approach takes into account the fact that G_{Ep} in regions of lower than experimentally measured momentum transfer values is closely related to the charge density $\rho(r)$ at large values of r, which is constrained using form factor data at finite values of Q^2, thereby reducing the model dependence in extrapolation. While corrections for relativistic effects are applied in this analysis, it is not possible to rigorously define an accurate three-dimensional charge density for the proton, as previously discussed. Using different form factor parametrizations of the data prior to 2010, Sick obtained a $\langle r_{Ep}^2 \rangle^{1/2}$ value of 0.887(12) fm, which is consistent with the Mainz result (Bernauer *et al.*, 2010) but inconsistent with the muonic hydrogen results (Pohl *et al.*, 2010; Antognini *et al.*, 2013).

Zhou *et al.* (2019) adopted a flexible approach within a Bayesian paradigm that does not make any parametric assumptions for G_{Ep}, but with two physical constraints: a normalization constraint for $G_{Ep}(0)$, and the condition that G_{Ep} monotonically decreases as Q^2 increases. The value of the proton charge radius extracted from the Mainz data is found to be sensitive to the Q^2 range of the data used in this analysis.

Horbatsch (2020) analyzed the PRad data on the proton G_E following a proposal by Hagelstein and Pascalutsa (2019) by taking the logarithm to yield a Q^2-dependent radius function. This analysis shows that the PRad data are in agreement with theoretical predictions from dispersively improved chiral perturbation theory.

Atac *et al.* (2021) extracted both the proton and the neutron charge radius from a global analysis of the world proton and neutron form factor data by carrying out a flavor separation of the Dirac form factor F_1 while assuming isospin symmetry. The u- and d-quark root-mean-squared transverse radii are subsequently determined from a fit to the slope of the corresponding flavor-dependent Dirac form factors, from which both the proton and the neutron charge radii are reconstructed. In this analysis, a proton charge radius value of $0.852 \pm 0.002_{(stat)} \pm 0.009_{(syst)}$ fm is obtained, which is consistent with the muonic hydrogen results as well as the latest result from the PRad experiment (Xiong *et al.*, 2019). Excluding the PRad data, a $\langle r_{Ep}^2 \rangle^{1/2}$ value of 0.857(13) fm is extracted. This is consistent with the value including the PRad data but has a larger uncertainty.

Borisyuk and Kobushkin (2020) reanalyzed the Mainz data (Bernauer *et al.*, 2010) and found that the radius value obtained under certain conditions can be consistent with the muonic hydrogen results.

Cui *et al.* (2021) extracted values of $\langle r_{Ep}^2 \rangle^{1/2}$ using the electron-proton-scattering data from the PRad experiment at JLab (Xiong *et al.*, 2019) and the A1 experiment at Mainz (Bernauer *et al.*, 2010) using a statistical sampling approach based on the Schlessinger point method (SPM). The SPM, with an important feature that no specific functional form is assumed for the interpolation, is used in this analysis for the

interpolation and extrapolation of smooth functions to minimize biases associated with assumed forms. Cui *et al.* (2021) obtained a radius value of $\langle r_{Ep}^2 \rangle^{1/2} = 0.838 \pm 0.005_{stat}$ fm from the PRad experiment and a value of $\langle r_{Ep}^2 \rangle^{1/2} = 0.856 \pm 0.014_{stat}$ fm from the Mainz A1 experiment, including data up to a Q^2 value of 0.014 $(GeV/c)^2$. Combining these two values, Cui *et al.* found a proton charge radius value of

$$\langle r_{Ep}^2 \rangle^{1/2} = 0.847 \pm 0.008_{stat} \text{ fm} \qquad (73)$$

from the two most recent experiments (Bernauer *et al.*, 2010; Xiong *et al.*, 2019) by measuring the unpolarized electron-proton elastic-scattering cross sections. This is consistent with the muonic hydrogen results (Pohl *et al.*, 2010; Antognini *et al.*, 2013), as well as the most recent ordinary hydrogen spectroscopy results (Bezginov *et al.*, 2019; Grinin *et al.*, 2020) for the proton charge radius.

Most recently, Gramolin and Russell (2021) analyzed the entire Mainz dataset (Bernauer *et al.*, 2010) using the two-dimensional Fourier transform of the Dirac form factor $F_1(Q^2)$, i.e., the proton transverse charge density discussed in Sec. III.C. The proton charge radius is related to the second moment of this transverse charge density. With this approach, they obtained the radius value $\langle r_{Ep}^2 \rangle^{1/2} = 0.889(5)_{stat}(5)_{syst}(4)_{model}$ fm, which is consistent with the original Mainz result (Bernauer *et al.*, 2010).

Figure 19 shows the proton charge radius results from electron-proton-scattering experiments since 2010 and the extracted $\langle r_{Ep}^2 \rangle^{1/2}$ values from some of the various analyses described previously. Also included are the muonic hydrogen results as well as the CODATA-2014 recommended value. While the results of some of these analyses are consistent with muonic hydrogen results on the $\langle r_{Ep}^2 \rangle^{1/2}$, others are consistent with the CODATA-2014 recommended value based on electron-scattering data, and few are in between. There is no conclusive statement that one can draw regarding the proton charge radius puzzle from these analyses of electron-proton-scattering data. New and further improved measurements from lepton scattering are highly desirable, which we describe in Sec. VII.

VI. MODERN SPECTROSCOPIC MEASUREMENTS

A. Muonic hydrogen spectroscopic experiments

The first determination of the proton charge radius using muonic hydrogen atoms was carried out by Pohl *et al.* (2010) at the Paul Scherrer Institute (PSI) by measuring the transition frequency between the $2S_{1/2}^{F=1}$ and $2P_{3/2}^{F=2}$ states at wavelengths of around 6.01 μm using pulsed laser spectroscopy; see Fig. 20. The muonic hydrogen atoms were produced by stopping negative muons in a hydrogen gas target with a pressure of 1 hPa (1 mbar) at the $\pi E5$ beam line of the proton accelerator at PSI. The muonic atoms produced are in the $n \approx 14$ excited state, which then decay with about 1% probability to the $2S$ metastable state, while the majority (99%) decay to the $1S$ ground state. The lifetime of the long-lived $2S$ state at 1 hPa pressure is 1 μs. A 5-ns pulsed laser
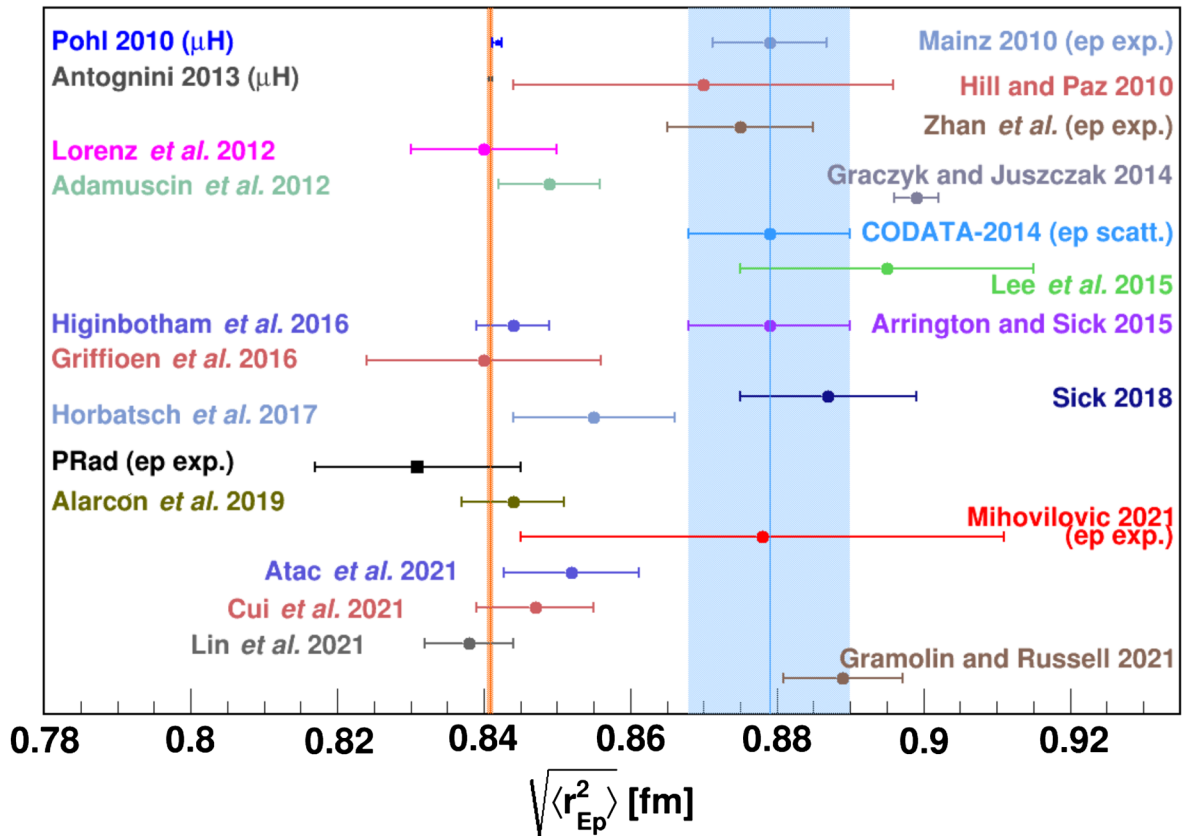
FIG. 19. The proton charge radius values determined from electron-scattering experiments since 2010 together with the results from various analyses of electron-proton scattering data (see the text). From Jingyi Zhou.

with a wavelength tunable at around 6 μm is incident upon and illuminates the target volume about 0.9 μs after the muons reach the target. The laser wavelength is scanned through the resonance of the $2S \to 2P$ transition. Upon the excitation, the

2P state with a lifetime of 8.5 ps will decay to the 1S state via emission of the 1.9-keV $K\alpha$ x ray. Therefore, in this pulsed muonic atom laser spectroscopic measurement, the resonance curve is recorded by the coincidence of the 1.9-keV x ray and
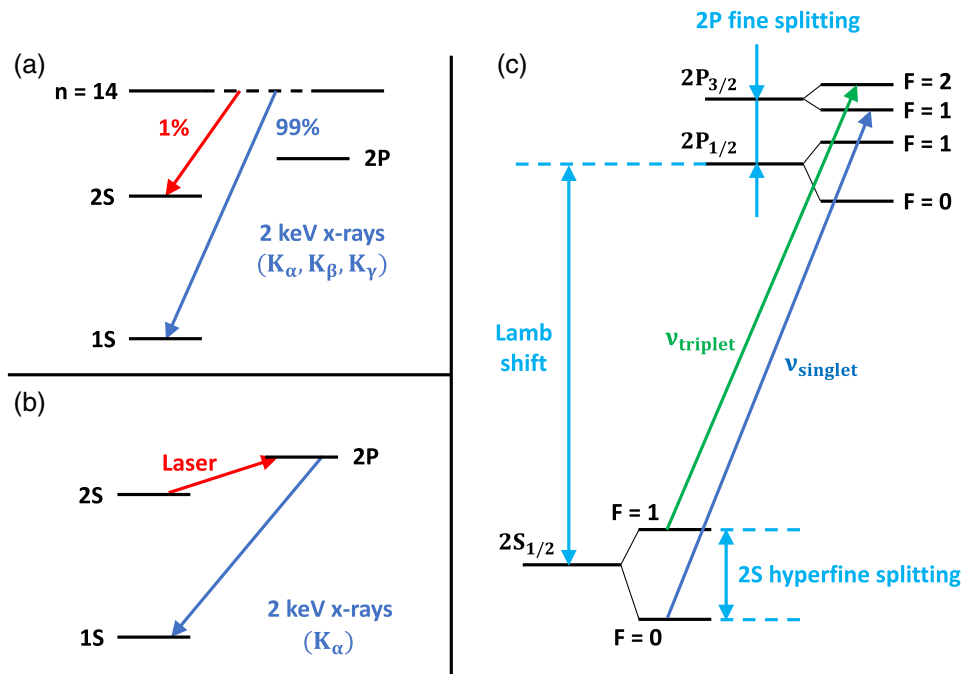
FIG. 20. Muonic hydrogen energy levels relevant to the proton charge radius measurement. From Jingyi Zhou.

the laser pulse as a function of the laser wavelength. A coincidence time window of 0.9 to 0.975 μs is chosen, i.e., 0.9 μs after the muons enter the H_2 target, and the 75-ns window corresponds to the confinement time of the laser light within the optics surrounding the target.

The resonance frequency for the transition between the $2S_{1/2}^{F=1}$ and $2P_{3/2}^{F=2}$ states was measured at 49 881.88(76) GHz (Pohl et al., 2010), which gave a proton charge radius value of $\langle r_{Ep}^2 \rangle^{1/2} = 0.841\,84(67)$ fm based on the state-of-the-art QED calculations. In a follow-up paper by the CREMA Collaboration (Antognini et al., 2013), the tunable laser wavelength was scanned from 5.5 to 6.0 μm and, in addition to the original transition between the $2S_{1/2}^{F=1}$ (triplet) and $2P_{3/2}^{F=2}$ states, a second transition between the $2S_{1/2}^{F=0}$ (singlet) and $2P_{3/2}^{F=1}$ states was also measured. The corresponding resonance frequencies were determined to be

$$\nu_t = 49\,881.35(57)_{\text{stat}}(30)_{\text{syst}} \text{ GHz},$$
$$\nu_s = 54\,611.16(1.00)_{\text{stat}}(30)_{\text{syst}} \text{ GHz}.$$

From these two transitions, the Lamb shift (LS) and the hyperfine splitting (HFS) can be independently determined, and they are

$$\Delta E_{\text{LS}}^{\text{exp}} = 202.3706(23) \text{ meV},$$
$$\Delta E_{\text{HFS}}^{\text{exp}} = 22.8089(51) \text{ meV}. \tag{74}$$

Relating the state-of-the-art theory calculations of the Lamb shift (Pachucki, 1996, 1999; Eides, Grotch, and Shelyuto, 2001; Karshenboim et al., 2010; Jentschura, 2011; Borie, 2012; Karshenboim, Ivanov, and Korzinin, 2012) to the proton $\langle r_{Ep}^2 \rangle$, one obtains (in meV)

$$\Delta E_{\text{LS}}^{\text{th}}(2P - 2S) = 206.0336(15) - 5.2275(10)\langle r_{Ep}^2 \rangle + \Delta E_{\text{TPE}}, \tag{75}$$

where the last term is due to the two-photon-exchange proton polarizability contribution discussed in Sec. IV. Using the estimate of Eq. (71) for the latter, the extracted value for the proton charge radius is

$$\langle r_{Ep}^2 \rangle^{1/2} = 0.840\,87(26)_{\text{exp}}(29)_{\text{th}} \text{ fm} = 0.840\,87(39) \text{ fm}. \tag{76}$$

Equation (76) not only is consistent with the earlier result from the muonic hydrogen spectroscopic measurement (Pohl et al., 2010) but also represents the most precise value for the proton charge radius. Both these results were included in the 2018 CODATA compilation (Tiesinga et al., 2021) and dominate its recommended value for the proton charge radius.

One notices from Eq. (71) that the uncertainty δ of the present TPE estimate for the muonic hydrogen $2P - 2S$ Lamb shift, $\delta(\Delta E_{\text{TPE}}) = 2.0$ μeV, is comparable to the present experimental Lamb shift precision, $\delta(\Delta E_{\text{LS}}^{\text{exp}}) = 2.3$ μeV; see Eq. (74). A further improvement on the proton charge radius extraction from muonic hydrogen spectroscopy results therefore hinges upon further improving the TPE estimates.

B. Ordinary hydrogen spectroscopic experiments

Since the release of the first muonic hydrogen spectroscopic determination of the proton charge radius (Pohl et al., 2010), there have been four atomic hydrogen spectroscopic measurements of the proton charge radius (Beyer et al., 2017; Fleurbaey et al., 2018; Bezginov et al., 2019; Grinin et al., 2020), with Bezginov et al. (2019) providing a direct measurement of the hydrogen Lamb shift.

Beyer et al. (2017) carried out a measurement of the $2S - 4P$ transition of ordinary hydrogen atoms using a cryogenic beam of H atoms. A major improvement over previous experiments in overcoming the limitation due to the electron-impact excitation used to produce atoms in the metastable $2S$ state is the use of the Garching $1S - 2S$ apparatus (Parthey et al., 2011; Matveev et al., 2013) as a well-controlled cryogenic source of 5.8-K cold $2S$ atoms. In this case, the $2S_{1/2}^{F=0}$ sublevel is almost exclusively populated via Doppler-free two-photon excitation without imparting additional momentum on the atoms. The line shifts due to quantum interference of neighboring atomic resonances and the first-order Doppler shift are the two remaining major systematic issues of this experiment. Apart from the use of a cryogenic H source that reduced the thermal velocity of atoms by a factor of 10 compared to prior experiments, Beyer et al. (2016) found that the employment of a specifically developed active fiber-based retroreflector allowed for a high level of compensation of the first-order Doppler shift: four parts in 10^6 of the full collinear shift. To suppress the quantum interference effect in order to determine the absolute $2S - 4P$ transition frequency, the experiment was designed to observe line shifts due to the quantum interference effect and to simulate the line shifts fully using an atomic line shape model. Finally the quantum interference effect is removed using the Fano-Voigt line shape to obtain the unperturbed transition frequency for both the $2S_{1/2}^{F=0} - 4P_{1/2}^{F=1}$ and $2S_{1/2}^{F=0} - 4P_{3/2}^{F=1}$ transitions. Combining this with previous precision measurements of the $1S - 2S$ transition by the same group (Parthey et al., 2011; Matveev et al., 2013), values for both the Rydberg constant and the proton charge radius were determined to be (Beyer et al., 2017)

$$R_\infty = 10\,973\,731.568\,076(96) \text{ m}^{-1},$$
$$\langle r_{Ep}^2 \rangle^{1/2} = 0.8335(95) \text{ fm}.$$

The uncertainty on the proton charge radius from this single experiment is comparable to the prior aggregate atomic hydrogen world data. This result is consistent with the muonic hydrogen results on the proton charge radius but 3.3 combined standard deviations smaller than the 2014 CODATA recommended value (Mohr, Newell, and Taylor, 2016) based on previous world data from ordinary hydrogen.

Fleurbaey et al. (2018) in Paris reported a result on the proton charge radius and the Rydberg constant in 2018 by combining their measurement of the $1S - 3S$ transition from ordinary atomic hydrogen with the $1S - 2S$ transition

measurement performed by the Garching group (Parthey *et al.*, 2011). The Paris experiment measured the $1S - 3S$ two-photon hydrogen transition frequency using a continuous-wave laser with a wavelength of 205 nm and through the Balmer-α $3S - 2P$ fluorescence detection. A room-temperature atomic hydrogen beam was used in the experiment and the main systematic effect of the experiment is the second-order Doppler effect due to the room-temperature atomic velocity distribution. The results presented included data taken during two different periods (2013 and 2016 to 2017) with improvements taking place between the two periods. The reported results are (Fleurbaey *et al.*, 2018)

$$R_\infty = 10\,973\,731.568\,53(14) \text{ m}^{-1},$$
$$\langle r_{Ep}^2 \rangle^{1/2} = 0.877(13) \text{ fm}.$$

While the extracted r_{Ep} value is consistent with the CODATA-2014 (Mohr, Newell, and Taylor, 2016) recommended value, it disagrees with the muonic hydrogen Lamb shift result (Antognini *et al.*, 2013) by 2.6 standard deviations. This experiment and the aforementioned experiment (Beyer *et al.*, 2017) used a similar measurement technique in which two transition frequencies are involved. Each transition is between two ordinary hydrogen energy levels, corresponding to two different principal quantum numbers n_1 and n_2, with at least one of them being an S state. We note that both the Rydberg constant and the proton charge radius determined from the Paris experiment (Fleurbaey *et al.*, 2018) disagree with those from the Garching experiment (Beyer *et al.*, 2017) at a level of about 2 standard deviations. It will be important to resolve such a discrepancy especially by repeating the same transition, either the $1S - 3S$ or the $2S - 4P$ transition.

To determine the proton charge radius from ordinary hydrogen spectroscopic measurements, one can also measure the Lamb shift (the $2S_{1/2} - 2P_{1/2}$ transition) directly, in which case the principal quantum numbers for the two states between the transition are the same, and as such the precision of the Rydberg constant from other experiments is sufficient and the Lamb shift measurement itself together with the state-of-the-art QED calculation is used to extract $\langle r_{Ep}^2 \rangle^{1/2}$. The most recent r_{Ep} determination (Bezginov *et al.*, 2019) from ordinary atomic hydrogen spectroscopy is such a measurement. In the experiment by Bezginov *et al.* (2019), a fast beam of hydrogen atoms was created by passing protons (which were accelerated to 55 keV) through a molecular hydrogen target chamber. About half of the protons were neutralized into hydrogen atoms from collisions with the molecules, and about 4% were created in the metastable $2S$ state. The experiment used two different radio frequency cavities to drive the $2S$ state away from the $F = 1$ substates so that only the $F = 0$ substate survives. The $2S_{1/2}(F = 0) \rightarrow 2P_{1/2}(F = 1)$ transition is the Lamb shift measured in this experiment using the experimental technique of a frequency-offset separated oscillatory field (Vutha and Hessels, 2015; Kato, Skinner, and Hessels, 2018), which is a modified Ramsey technique of separated oscillatory fields (Ramsey, 1949). The measured transition frequency of $2S_{1/2}(F = 0) \rightarrow 2P_{1/2}(F = 1)$ from this experiment is 909.8717(32) MHz. The Lamb shift

determined is 1057.8298(32) MHz after including the contribution from hyperfine structure, which is 147.9581 MHz (Horbatsch and Hessels, 2016b). The proton charge radius value deduced from this experiment is (Bezginov *et al.*, 2019)

$$\langle r_{Ep}^2 \rangle^{1/2} = 0.833(10) \text{ fm}, \tag{77}$$

which is consistent with the muonic hydrogen Lamb shift measurements (Pohl *et al.*, 2010; Antognini *et al.*, 2013), the 2017 ordinary hydrogen measurement (Beyer *et al.*, 2017), and the PRad result from electron scattering (Xiong *et al.*, 2019). It disagrees, however, with the Paris measurement (Fleurbaey *et al.*, 2018) at a level of about 2 standard deviations.

Most recently, a new result on $\langle r_{Ep}^2 \rangle^{1/2}$ from ordinary hydrogen spectroscopy has been published (Grinin *et al.*, 2020). This experiment measured the same $1S - 3S$ transition as that of Fleurbaey *et al.* (2018) but with significantly improved precision. Major improvements in reducing systematic uncertainties have been achieved by using a cold atomic beam and a two-photon direct frequency comb technique. The experiment also achieved an almost shot noise limited statistical uncertainty of 110 Hz. The unperturbed frequency for the $1S(F = 1) - 3S(F = 1)$ transition determined from this experiment is $2\,922\,742\,936\,716.72(72)$ kHz, and f_{1S-3S} (centroid) $= 2\,922\,743\,278\,665.79(72)$ kHz after subtracting the hyperfine shifts. Combing this new result on the $1S - 3S$ transition with the $1S - 2S$ transition frequency previously measured by the same group (Matveev *et al.*, 2013), Grinin *et al.* (2020) obtained

$$R_\infty = 10\,973\,731.568\,226(38) \text{ m}^{-1},$$
$$\langle r_{Ep}^2 \rangle^{1/2} = 0.8482(38) \text{ fm}.$$

This extracted Rydberg constant is in agreement with the latest CODATA-2018 (Tiesinga *et al.*, 2021) recommended value. The new proton charge radius result from Grinin *et al.* (2020) is more than a factor of 2 more precise but also 2.9 standard deviations smaller than the the CODATA-2014 recommended value from ordinary hydrogen spectroscopic measurements. It is more than a factor of 3 more precise but 2.1 standard deviations smaller than the Paris result (Fleurbaey *et al.*, 2018). Compared with muonic hydrogen results on $\langle r_{Ep}^2 \rangle^{1/2}$, this new result from the $1S - 3S$ transition is about 2 standard deviations larger. Figure 21 shows the results on $\langle r_{Ep}^2 \rangle^{1/2}$ from the four latest spectroscopic measurements using ordinary hydrogen atoms (Beyer *et al.*, 2017; Fleurbaey *et al.*, 2018; Bezginov *et al.*, 2019; Grinin *et al.*, 2020) together with the muonic hydrogen results (Pohl *et al.*, 2010; Antognini *et al.*, 2013). Also shown is the CODATA-2014 (Mohr, Newell, and Taylor, 2016) recommended value based on ordinary hydrogen spectroscopy. While major progress has been made in recent years and most of these recent measurements of the proton charge radius support a smaller value including the PRad result (Xiong *et al.*, 2019), the comparison of $\langle r_{Ep}^2 \rangle^{1/2}$ extractions between electronic versus muonic systems is not fully settled. This situation highlights the importance of future high-precision scattering experiments to improve on the result
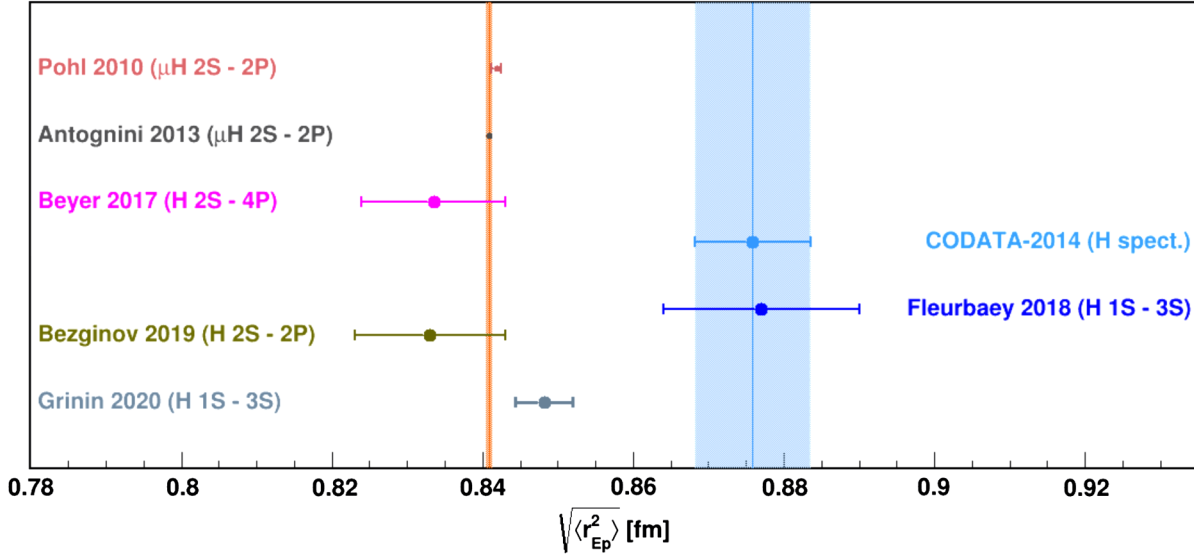
FIG. 21.   The latest proton charge radius results from ordinary hydrogen spectroscopic measurements together with muonic hydrogen results and the CODATA-2014 recommended value based on ordinary hydrogen spectroscopy. From Jingyi Zhou.

obtained by PRad. It is also highly desirable to have future spectroscopic measurements from ordinary hydrogen to achieve a comparable precision, i.e., a relative precision of 0.5% or better. The PRad-II and other ongoing and upcoming scattering experiments are discussed in Sec. VII.

Table IV provides a summary of the aforementioned spectroscopic measurements using both muonic and ordinary hydrogen published since 2010.

VII. ONGOING AND UPCOMING EXPERIMENTS

In this section we describe the current and planned experiments aimed at extracting the proton charge radius. Some of these plans were also discussed in a recent review by Karr, Marchand, and Voutier (2020).

A. The MUSE experiment at PSI

The muonic hydrogen spectroscopic results on the proton charge radius (Pohl *et al.*, 2010; Antognini *et al.*, 2013) also motivated lepton-proton-scattering measurements with muon beams. The MUon proton Scattering Experiment (MUSE) (Gilman *et al.*, 2013, 2017) at PSI is currently ongoing, in which measurements of lepton-proton elastic-scattering cross sections utilizing both the μ^+ and μ^- (muon) beams will be compared to those performed with electron and positron

beams. The MUSE experiment uses the PSI $\pi M1$ beam line with $e^\pm$, and $\mu^\pm$ beams at incident momentum values of 115, 153, and 210 MeV/c to allow for simultaneous measurements of the $\mu^\pm p$ and $e^\pm p$ elastic-scattering cross sections. The coverage of the scattering angle for the MUSE experiment is 20°–100°, corresponding to a Q^2 range of 0.0016 (with 115 MeV/c beam momentum) to 0.08 (GeV/c)^2 (210 MeV/c incident beam momentum). Because of the mass difference of $e^\pm$ and $\mu^\pm$, there is a small difference in the Q^2 coverage between the two. The lowest Q^2 value reached by MUSE is comparable to that of the Mainz experiment (Bernauer *et al.*, 2010) but much higher than that of the PRad experiment (Xiong *et al.*, 2019), 0.0002 (GeV/c)^2. In addition to the μ and e beam particles, there are also pions in the $\pi M1$ mixed beam. Therefore, beam-line detectors for identifying various beam particles, determining the beam particle momentum and trajectories into the target, and counting the beam particles are important for the MUSE experiment. The beam-line detectors include a beam hodoscope (fast scintillator array) measuring times relative to the accelerator rf to identify beam particle type, GEM detectors, a veto scintillator, a beam monitor, and a calorimeter. A liquid hydrogen target is the main target for the production data taking with two symmetric spectrometers each equipped with detectors consisting of two scattered particle scintillator (SPS) paddles and two straw-tube trackers (STT). A schematic setup

TABLE IV.   Summary of proton charge radius results from muonic and ordinary hydrogen spectroscopic measurements published since 2010.

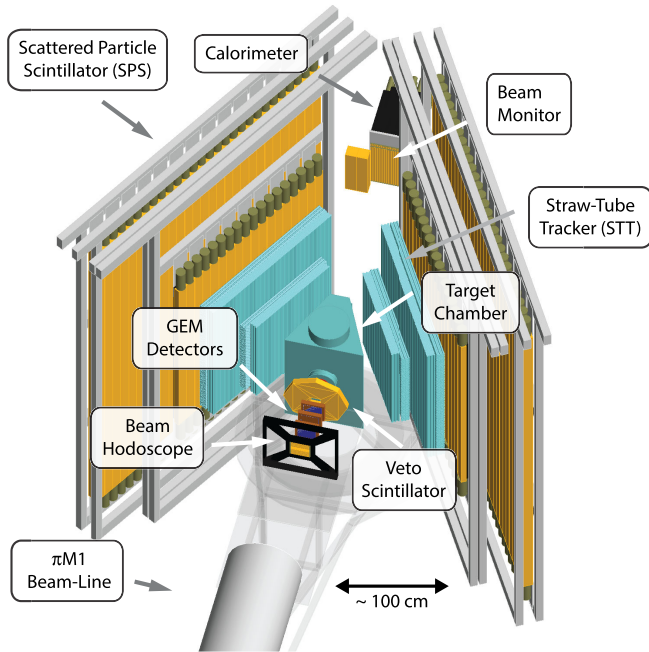| Experiment	Type	Transition(s)	$\sqrt{\langle r_{Ep}^2 \rangle}$ (fm)	r_∞ (m^{-1})
Pohl 2010	μH	$2S_{1/2}^{F=1} - 2P_{3/2}^{F=2}$	0.841 84(67)	
Antognini 2013	μH	$2S_{1/2}^{F=1} - 2P_{3/2}^{F=2} \; 2S_{1/2}^{F=0} - 2P_{3/2}^{F=1}$	0.840 87(39)	
Beyer 2017	H	$2S - 4P$ with $(1S - 2S)$	0.8335(95)	10 973 731.568 076 (96)
Fleurbaey 2018	H	$1S - 3S$ with $(1S - 2S)$	0.877(13)	10 973 731.568 53(14)
Bezginov 2019	H	$2S_{1/2} - 2P_{1/2}$	0.833(10)	
Grinin 2020	H	$1S - 3S$ with $(1S - 2S)$	0.8482(38)	10 973 731.568 226(38)

FIG. 22. Schematic of the MUSE experiment at PSI. From Steffen Strauch.

of the MUSE experiment is shown in Fig. 22. The uncertainties from the MUSE experiment in the proton charge radius separately determined with $\mu^+ p$, $\mu^- p$, $e^+ p$, and $e^- p$ are expected to be nearly the same, around 0.01 fm. In addition to the determination of the proton charge radius, the MUSE experiment will allow for tests of the two-photon-exchange effect in lepton scattering by comparing the $\mu^\pm p$ and $e^\pm p$ cross section to a direct test of lepton universality. More details about the MUSE experiment were given by Cline *et al.* (2021). The MUSE Collaboration is working toward commissioning the entire experiment, with production data taking expected to start in the fall of 2021.

B. The AMBER experiment at CERN

The COMPASS Collaboration proposed a precision measurement of elastic μp scattering at high energy and low Q^2 with the M2 beam line at CERN with AMBER (Dreisbach *et al.*, 2019). By carrying out muon-proton scattering at high energies (compared to low-energy lepton-proton scattering) the proposed experiment has different, and in some cases favorable, systematics. The AMBER measurement of the proton radius will use 100-GeV muons of the CERN M2 beam line. The hydrogen target will be an active target [a high-pressure time-projection chamber (TPC)] in which the recoil protons will be measured for proton energies of 0.5 to 20 MeV. For small-angle scattered muon detection, silicon detectors will be used for precision tracking. The triggers will be formed by scattered muons using the 200 μm SciFi stations, and the inner tracking and the ECAL of the COMPASS spectrometer will be used for measuring the scattered muons. The proposed experiment with 200 days of beam time will extract the proton electric form factor in a Q^2 range of 0.001 to 0.04 $(\text{GeV}/c)^2$ with relative point-to-point precision better than 0.001. The projected precision in the determination of the proton charge

radius is expected to be better than 0.01 fm. The experiment has been approved to run at CERN in the coming years. Figure 23 (top panel) shows the schematics of the AMBER setup for the proton charge radius measurement, including the time-projection chamber, scintillating-fiber hodoscope, and the silicon-pixel detectors. The entire setup in the AMBER spectrometer with relevant parts shown is illustrated in Fig. 23 (bottom panel).

C. The PRad-II experiment at Jefferson Lab

Following the PRad experiment (Xiong *et al.*, 2019), the PRad Collaboration proposed a new and upgraded experiment, PRad-II (Dutta, Gao, Gasparian, Gnanvo *et al.*, 2020; Gasparian *et al.*, 2020) to the Jefferson Lab program advisory committee (PAC). Leading the next generation of the proton charge radius measurements, PRad-II will use an electromagnetic calorimeter together with two planes of tracking detectors with several major upgrades and improvements over the PRad experiment. The experiment has been approved by the PAC with the highest scientific rating.

One important aspect of PRad-II relative to PRad is to reduce the statistical uncertainty of the electron-proton elastic-scattering cross-section measurement by a factor of 4. Furthermore, a number of upgrades will improve the precision in determining the proton electric form factor and the charge radius significantly by reducing systematic uncertainties. The upgrades include (i) adding a second tracking detector plane for improving the tracking capability and further suppressing the beam-line related background, (ii) upgrading the HyCal by replacing its outer-region lead glass modules with $PbWO_4$ crystals to improve the detector resolutions and uniformity and to suppress the inelastic contamination, (iii) adding a set of cross-shaped scintillator detectors in order to detect scattered electrons from ep at scattering angles as forward as 0.5° while still being cleanly separated from ee scattering, (iv) upgrading the HyCal readout to flash analog-to-digital converter to enhance the data taking rate, (v) adding a second beam halo blocker together with improved beam-line vacuum to further suppress the background, and (vi) further improved radiative correction calculations at the next-to-next-to-leading order for both ep and ee scattering. These upgrades and improvements will lead to the reduction of the overall experimental uncertainty in the radius determination by a factor of 3.8 compared to PRad. As the muonic hydrogen result with its unprecedented precision ($\sim$0.05%) dominates the CODATA value of the proton charge radius, it is critically important to help evaluate possible systematic uncertainties associated with muonic experiments using different experimental methods with high precision and different systematics. The PRad-II experiment, with its projected total uncertainty smaller than 0.5%, could potentially inform whether there is any systematic difference in the radius results between e-p-scattering and muonic hydrogen measurements. PRad-II will cover a Q^2 range of 4×10^{-6} to 2×10^{-2} $(\text{GeV}/c)^2$ [the first lepton-scattering experiment to reach below 10^{-4} $(\text{GeV}/c)^2$] with three proposed incident beam energies: 0.7, 1.4, and 2.1 GeV. Figure 24 shows the schematics of the proposed PRad-II setup. The proposed tracking detectors can be built based on the new μRWELL
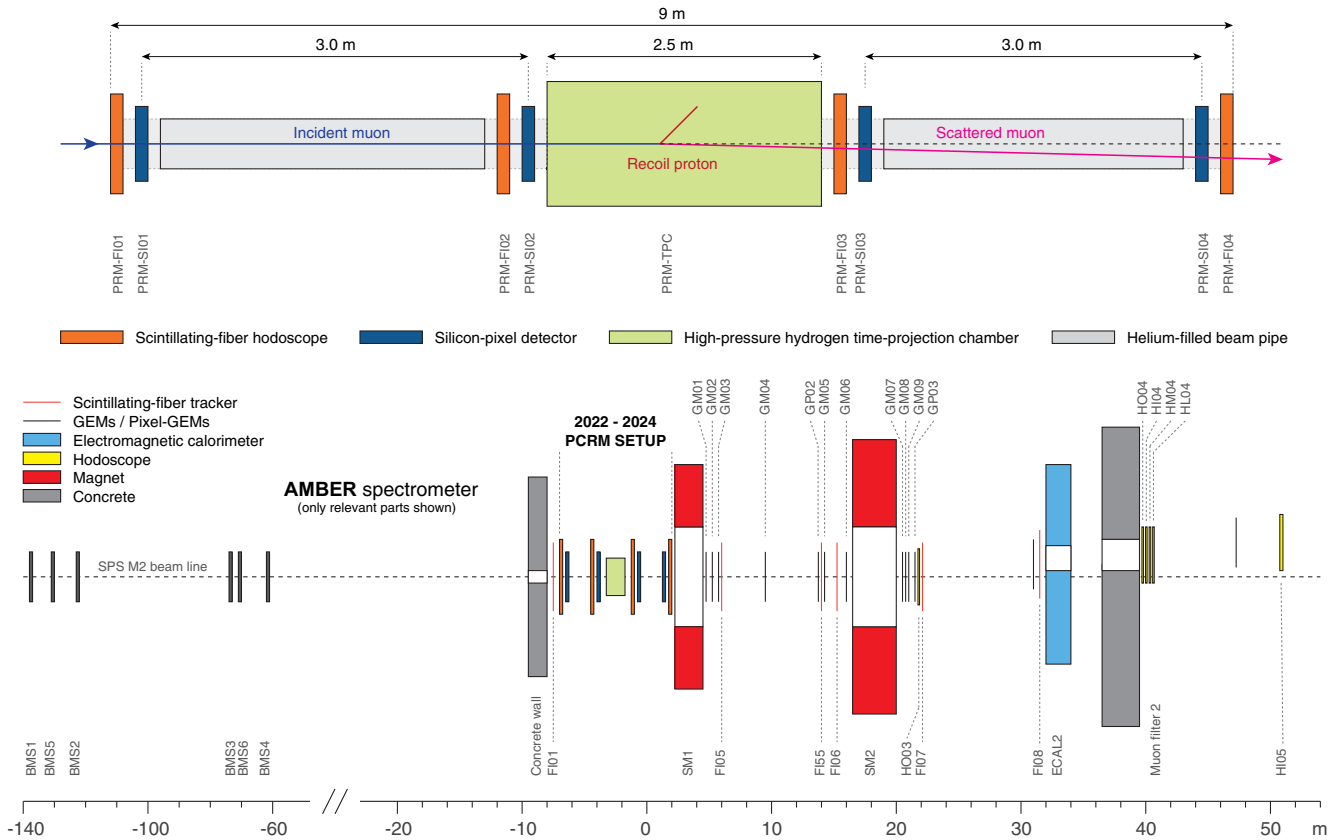
FIG. 23.   Top panel: schematics of the AMBER setup for the proton charge radius measurement. Bottom panel: entire setup in the AMBER spectrometer with relevant parts shown. From Christian Dreisbach, Technical University of Munich.

technology (Bencivenni *et al.*, 2015) or the GEM as used in the PRad experiment.

Figure 25 shows the projected radius measurement from PRad-II together with some of the most recent results on the proton radius, including the *e*-*p*-scattering results (Xiong *et al.*, 2019), the two muonic hydrogen results (Pohl *et al.*, 2010; Antognini *et al.*, 2013), and the three recent atomic hydrogen spectroscopic results (Beyer *et al.*, 2017; Bezginov *et al.*, 2019; Grinin *et al.*, 2020). Also shown is the CODATA-2018 (Tiesinga *et al.*, 2021) recommended value. The blue line and the band represent the weighted average of the $\langle r_{Ep}^2 \rangle^{1/2}$ value and its uncertainty for the three proton radius values (Beyer *et al.*, 2017; Bezginov *et al.*, 2019; Xiong *et al.*, 2019) from ordinary hydrogen spectroscopy and
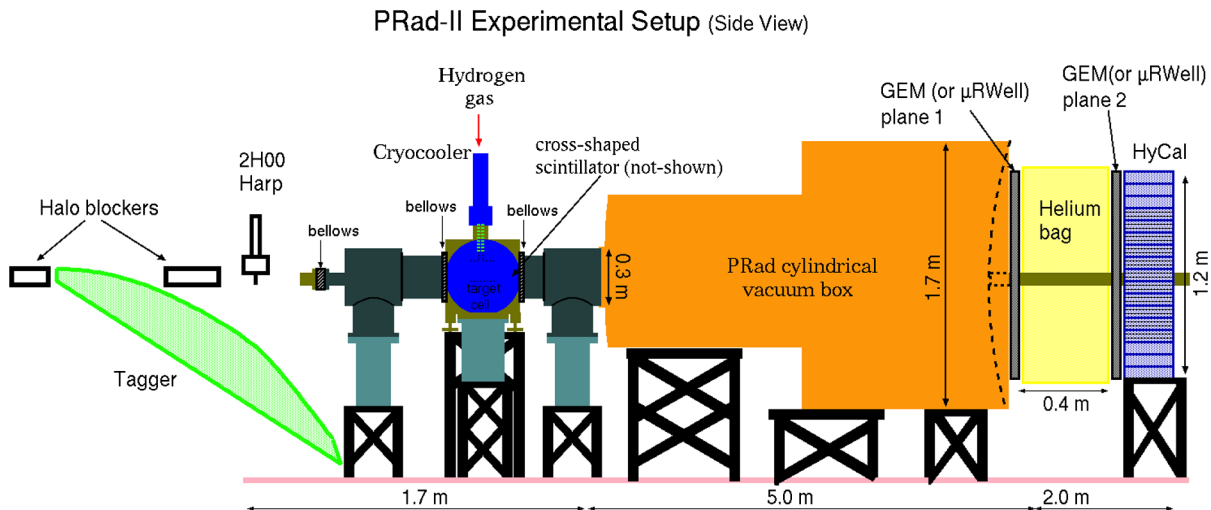
FIG. 24.   Schematic of the setup for the proposed PRad-II experiment. The incident electron beam progresses from left to right. From Dipangkar Dutta.
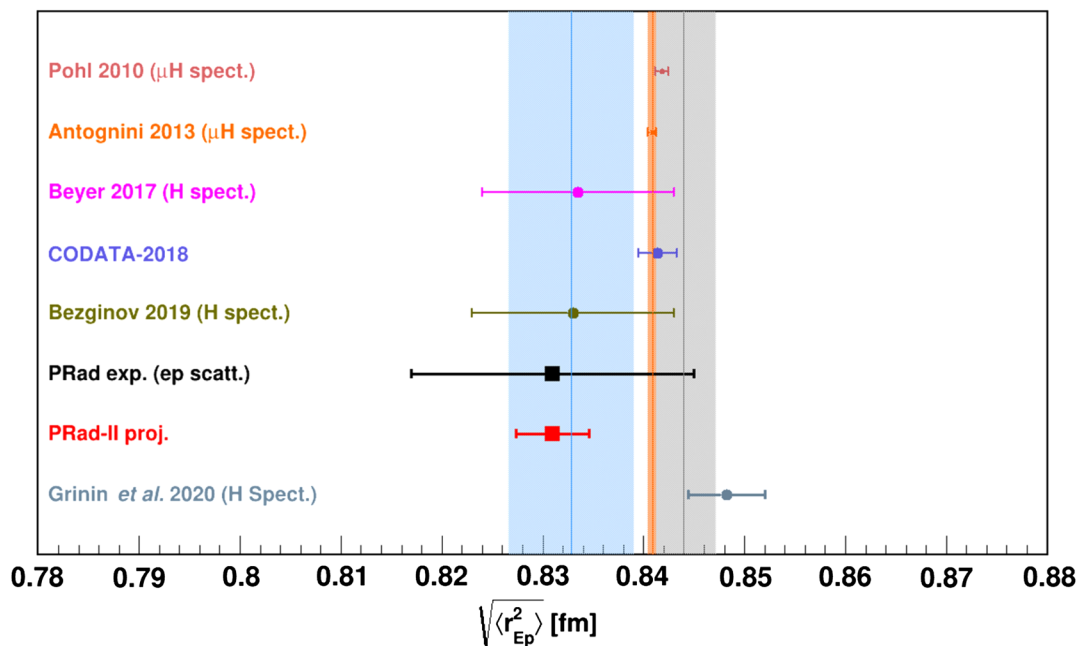
FIG. 25. PRad-II projection for $\langle r_{Ep}^2 \rangle^{1/2}$ with all proposed upgrades and improvements shown with a few selected results from other experiments and CODATA-2018 recommendations (see the text). From Jingyi Zhou.

electron-proton scattering. The gray line and band are the results from the weighted average of all four, including the result of Grinin *et al.* (2020). Figure 25 illustrates two points: (i) the importance of improving the precision of $\langle r_{Ep}^2 \rangle^{1/2}$ measurements from electronic systems, whether it be ordinary hydrogen spectroscopy or electron-proton scattering, and (ii) new measurements from ordinary hydrogen in addition to the results of Grinin *et al.* (2020) and the upcoming PRad-II will be essential for determining whether there is a difference between $\langle r_{Ep}^2 \rangle^{1/2}$ determined using the electronic versus the muonic system.

For the PRad-II projection, it is shown that with all proposed upgrades and improvements the projected overall uncertainty in the proton radius measurement will be 0.0036 fm, which is slightly smaller than the 0.0038 fm precision from the latest hydrogen spectroscopy result of Grinin *et al.* (2020), the most precise measurement from ordinary hydrogen atomic spectroscopy.

If the PRad $\langle r_{Ep}^2 \rangle^{1/2}$ value would prevail, the PRad-II result could signal a more than 2.7 standard deviation smaller value than the muonic hydrogen result. While it does not seem possible in the foreseeable future for lepton-scattering experiments to reach the precision of muonic hydrogen spectroscopic measurements, the improvement of PRad-II is significant and will have great potential to inform whether there is any systematic difference between muonic hydrogen results and results from electron scattering. The PRad-II measurement together with future improvements in ordinary hydrogen spectroscopic measurements will shed light on whether there is any systematic difference between the proton charge radius determined from electronic versus muonic systems. Therefore, interesting new physics such as the violation of lepton universality may be uncovered.

D. Electron-scattering experiments at Mainz University

There are two major new programs at Mainz University aimed at measuring the electron-proton elastic scattering at low Q^2 that will provide new results on the proton charge radius in the coming years.

The first is the PRES experiment (Vorobyev and Denig, 2017; Belostotski, Sagidova, and Vorobyev, 2019; Vorobyev, 2019) at the Microtron MAMI in the A2 experimental hall. In this experiment the polar angle of the scattered electron will be measured with high accuracy using a forward tracker. For the recoil proton the energy and the angle will be measured with a TPC. Therefore, the experiment will have overdetermined kinematics and will access e-p elastic scattering in a Q^2 region from 0.001 to 0.04 $(GeV/c)^2$. Compared to the other e-p-scattering experiments in which scattered electrons are commonly measured, the Mainz PRES experiment will have different systematics. The projected systematic error for the cross section will be controlled with an accuracy of 0.1% (relative) and 0.2% (absolute). The PRES experiment is projected to reach 0.5% statistical precision on $\langle r_{Ep}^2 \rangle^{1/2}$, with systematic errors $\leq 0.3\%$. The combination of the electron-scattering result from the PRES experiment and the muon scattering result from COMPASS$++$/AMBER will allow for a test of lepton universality in the proton charge radius, taking advantage of a similar experimental approach used in both measurements. In addition, PRES will provide crucial input for calibration of the TPC setup at COMPASS$++$/ AMBER, taking advantage of the high-quality electron beam delivered by MAMI.

A further test of the lepton universality in the proton charge radius extraction was proposed by Pauk and Vanderhaeghen (2015) through the photoproduction of a lepton pair on a
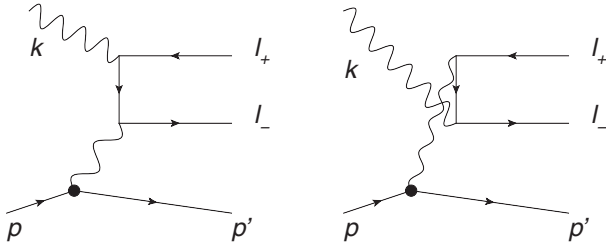
FIG. 26. Bethe-Heitler (left image) direct and (right image) crossed diagrams of the $\gamma p \to l^- l^+ p$ process, where the four-momenta of the external particles are k for the photon, p (p') for initial (final) protons, and l_-, l_+ for the lepton pair.
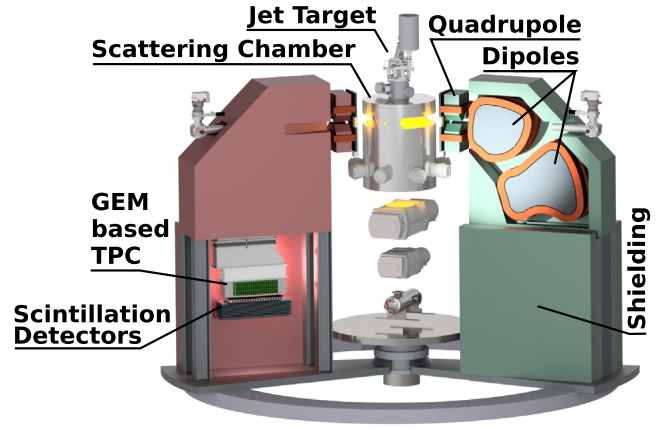

FIG. 27. The MAGIX high-resolution dual-spectrometer setup at the MESA accelerator. The gas-jet target in the center is also visible. From Schlimme *et al.*, 2021.

proton target in the limit of small momentum transfer, in which this reaction is dominated by the Bethe-Heitler process shown in Fig. 26. By detecting the recoiling proton in the $\gamma p \to l^- l^+ p$ reaction, it was shown that a measurement of a cross-section ratio of $e^- e^+ + \mu^- \mu^+$ vs $e^- e^+$, above versus below dimuon threshold, respectively, accesses the same information as muon versus electron-scattering experiments. Furthermore, such a measurement is free from hadronic background if one performs the measurement in the dilepton mass window between the dimuon thresholds and below the $\pi\pi$ threshold. It thus complements a comparison of elastic l-p-scattering data, as the overall normalization uncertainty due to the photon flux drops out of the dilepton photoproduction cross-section ratio. The feasibility of such experiment using a high-pressure TPC as an active target in combination with the Crystal Ball–TAPS setup at MAMI is currently under study (Sokhoyan, 2020).

The second program at Mainz consists of two parts. The first is A1@MAMI, an ongoing experiment (Bernauer, 2020) in the A1 experimental hall with the MAMI accelerator using a hydrogen gas-jet target to provide better control of a few systematic uncertainties associated with the original A1 experiment (Bernauer *et al.*, 2010), and also to investigate the systematic difference in the G_E^p results between the PRad (Xiong *et al.*, 2019) and A1 experiments. The second (MAGIX@MESA) is centered around the Mainz Superconducting Energy Recovery Linac (MESA), which is a new accelerator presently under construction at the University of Mainz (Hug *et al.*, 2020). MESA is designed as a recirculating superconducting linear accelerator that provides an external beam with high current and a high degree of polarization. In the energy recovery mode, MESA will deliver an electron beam with 20–105 MeV and a current of 1 mA, which is ideal for precision experiments. The Mainz Gas-Internal Target Experiment (MAGIX) experiment at MESA will consist of a quadrupole in front of two medium sized dipole magnets; see Fig. 27. The compact design of the spectrometers will allow for a relative momentum resolution of the order of 10^{-4}. A time-projection chamber with an open field cage and GEM readout is being developed for the focal-plane detector (Gülker *et al.*, 2019; Caiazza *et al.*, 2020). Finally, a windowless internal gas-jet target (Grieser *et al.*, 2018), which has already been commissioned at MAMI (Schlimme *et al.*, 2021), will be used.

With the MAGIX experiment at MESA, for the first time in hadron physics an experiment will be developed that

combines the advantages of an ultralight windowless gas target with the high intensity of an energy recovery linac accelerator. This combination of a high beam intensity and a target in which multiple scattering of the outgoing particles will be minimized will lead to competitive luminosities in the range of 10^{35} cm^{-2} s^{-1} while providing at the same time a clean experimental environment. With the low beam energies of MESA, it will be possible to reach Q^2 values in e-p scattering down to 10^{-4} (GeV/c)^2, and a relative precision on the proton electron form factor G_{Ep} down to 0.05%. It will also significantly improve the determination of the proton magnetic radius (Bernauer, 2020).

E. The ULQ^2 experiment at Tohoku University

The Ultra-Low Q^2 (ULQ^2) Collaboration (Suda, 2018) proposed carrying out an electron-scattering experiment at the Research Center for Electron-Photon Science at Tohoku University using its 60 MeV electron linac. This experiment will use the electron beam at energies from 20 to 60 MeV with a scattering angular range of 30° to 150°, corresponding to a Q^2 range of $0.0003 - 0.008$ (GeV/c)^2 for e-p elastic scattering, aiming at an absolute cross-section measurement with a precision of 0.1%. The ULQ^2 experiment will use a CH$_2$ target with elastic $e - {}^{12}$C as a reference reaction for normalization purposes. The root-mean-square charge radius of the ^{12}C nucleus is known to a relative precision of $\sim 3 \times 10^{-3}$. The proton electric form factor G_{Ep} will be extracted using the Rosenbluth separation technique. The proposed experimental setup will consist of two magnetic spectrometers for Rosenbluth separation measurements, and luminosity monitoring. To carry out this experiment, a new beam line and a high-resolution new spectrometer with single-sided silicon detectors (SSDs) have already been built and commissioned. The SSDs developed together with the J-PARC muon $g - 2$ and the neutron electric dipole moment experiments (Sato, 2017) are employed as the focal-plane detector. The second spectrometer for luminosity monitoring is under construction and will be commissioned in the near future. This experiment is aiming at a precision of $\sim$1% (relative) in determining the proton charge radius and is expected to start taking data in
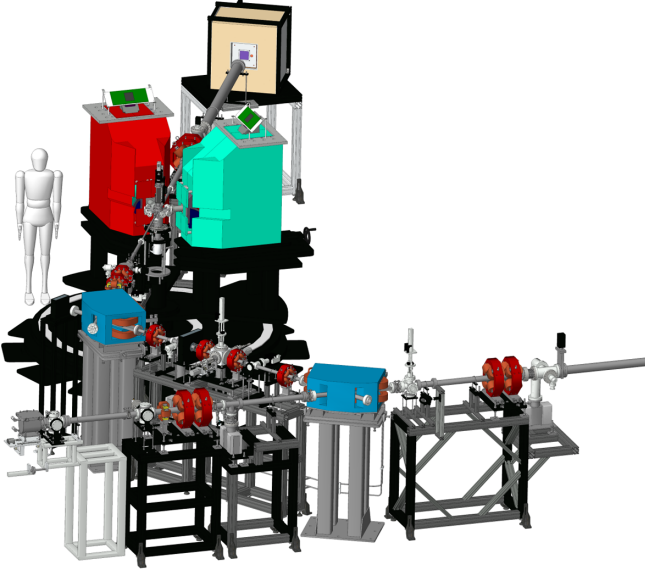
FIG. 28. Schematics of the ULQ^2 experimental setup. From Toshimi Suda.

2022. Figure 28 shows the schematics of the ULQ^2 experimental setup.

In Table V we provide a summary of these ongoing and future lepton-scattering experiments in terms of the beam type(s), the location, the Q^2 coverage, the projected precision in the proton charge radius determination when available, and the status of each experiment.

VIII. THE DEUTERON CHARGE RADIUS

A less well-known charge radius puzzle concerns the deuteron, the simplest nucleus in nature, which is loosely bound with a binding energy of 2.2 MeV. Like the proton, the deuteron charge radius can be determined by the extraction of the deuteron charge form factor $G_{Cd}(Q^2)$ at low values of Q^2 from electron-deuteron elastic scattering first, and the subsequent extrapolation of the measured $G_{Cd}(Q^2)$ to the unmeasured region in order to determine its slope at $Q^2 = 0$.

The unpolarized elastic e-d-scattering cross section is described in the one-photon-exchange picture as

$$\frac{d\sigma}{d\Omega}(E, \theta) = \sigma_{NS}\left\{A_d(Q^2) + B_d(Q^2)\tan^2\frac{\theta}{2}\right\}, \quad (78)$$

where σ_{NS} is the differential cross section for the elastic scattering from a pointlike and spinless particle at a scattering angle θ and an incident energy E. For a spin-1 object such as the deuteron, the electromagnetic structure can be described by three form factors: the charge G_{Cd}, the magnetic dipole G_{Md}, and the electric quadrupole G_{Qd}. The structure functions $A_d(Q^2)$ and $B_d(Q^2)$ are related to these form factors via (Jankus, 1956; Gourdin, 1963)

$$A_d(Q^2) = G_{Cd}^2(Q^2) + \tfrac{2}{3}\tau_d G_{Md}^2(Q^2) + \tfrac{8}{9}\tau_d^2 G_{Qd}^2(Q^2),$$
$$B_d(Q^2) = \tfrac{4}{3}\tau_d(1 + \tau_d)G_{Md}^2(Q^2), \quad (79)$$

with $\tau_d \equiv Q^2/4M_d^2$, where M_d is the deuteron mass. There are also the following additional relations:

$$G_{Cd}(0) = 1, \qquad G_{Md}(0) = \mu_d, \qquad G_{Qd}(0) = Q_d,$$

with μ_d the deuteron magnetic dipole moment (in units of $e/2M_d$) and Q_d the electric quadrupole moment (in units of e/M_d^2). With three form factors, one needs to carry out three measurements with independent combinations of the three form factors in order to separate them out for each Q^2 value. Carlson and Vanderhaeghen (2009) showed how these three form factors allow one to map out the transverse charge densities in a deuteron, in a state of helicity 0 or ±1, as viewed from a light front moving toward the deuteron. Furthermore, the charge densities for a transversely polarized deuteron are characterized by monopole, dipole, and quadrupole patterns.

At low values of Q^2 most relevant for the charge radius determination, in the range $10^{-2}-10^{-4}$ (GeV/c)^2 and with small scattering angles, the unpolarized e-d elastic-scattering cross section is dominated by the deuteron charge form factor. One can therefore extract G_{Cd} with negligible systematic uncertainties using data driven parametrizations for G_{Md}, and G_{Qd} (Zhou $et\ al.$, 2021) from a measured scattering cross section. The deuteron rms charge radius can then be determined by fitting the experimental G_{Cd} data as a function of Q^2 and calculating the slope of this function at $Q^2 = 0$ according to

$$\langle r_{Cd}^2\rangle \equiv -6\frac{dG_C^d(Q^2)}{dQ^2}\bigg|_{Q^2=0}, \quad (80)$$

in analogy with how $\langle r_{Ep}^2\rangle$ is obtained. Zhou $et\ al.$ (2021) demonstrated how one can extract r_d reliably using robust fitters.

TABLE V. Summary of ongoing and future lepton-scattering experiments on proton charge radius measurements.

Experiment	Beam	Laboratory	Q^2 [(GeV/c)^2]	δr_p (fm)	Status
MUSE	$e^\pm$, $\mu^\pm$	PSI	0.0015–0.08	0.01	Ongoing
AMBER	$\mu^\pm$	CERN	0.001–0.04	0.01	Future
PRad-II	e^-	Jefferson Lab	4×10^{-5}–6×10^{-2}	0.0036	Future
PRES	e^-	Mainz	0.001–0.04	0.6% (relative)	Future
A1@MAMI (jet target)	e^-	Mainz	0.004–0.085		Ongoing
MAGIX@MESA	e^-	Mainz	$\geq 10^{-4} - 0.085$		Future
ULQ^2	e^-	Tohoku University	3×10^{-4}–8×10^{-3}	$\sim$1% (relative)	Future

Like the proton charge radius, the deuteron r_d can be determined from atomic spectroscopic measurements using ordinary deuterium or muonic deuterium atoms. The CREMA Collaboration reported a deuteron charge radius value from a muonic spectroscopy-based measurement of three $2P \to 2S$ transitions in muonic deuterium atoms as [labeled as μD in Fig. 27 of Pohl *et al.* (2016)]

$$\langle r_{Cd}^2 \rangle^{1/2} = 2.125\,62 \pm 0.000\,78 \text{ fm}, \qquad (81)$$

which is 2.7 times more accurate than but 7.5 standard deviations smaller than the CODATA-2010 recommended value (Mohr, Taylor, and Newell, 2012). Newer values of $\langle r_{Cd}^2 \rangle^{1/2}$ based on the muonic deuterium spectroscopic measurement (Pohl *et al.*, 2016) with improved theoretical calculations are (Hernandez *et al.*, 2018)

$$\langle r_{Cd}^2 \rangle^{1/2} = 2.126\,16 \pm 0.000\,90 \text{ fm}$$

and (Pachucki, Patkóš, and Yerokhin, 2018; Kalinowski, 2019)

$$\langle r_{Cd}^2 \rangle^{1/2} = 2.127\,17 \pm 0.000\,82 \text{ fm}.$$

From the spectroscopic measurement of $1S \to 2S$ transitions from ordinary deuterium atoms (Parthey *et al.*, 2010), Pohl *et al.* (2017) extracted the deuteron radius value

$$\langle r_{Cd}^2 \rangle^{1/2} = 2.1415 \pm 0.0045 \text{ fm},$$

which is 3.5 standard deviations larger than the extracted value of Eq. (81) from muonic deuterium atoms.

Another spectroscopic method commonly used to extract the deuteron charge radius utilizes the isotope shift of the $1S \to 2S$ transition between atomic hydrogen and deuterium (Huber *et al.*, 1998; Parthey *et al.*, 2010), from which one can precisely determine the following difference between the squares of the deuteron and proton charge radii (Jentschura *et al.*, 2011):

$$\langle r_{Cd}^2 \rangle - \langle r_{Ep}^2 \rangle = 3.820\,07(65) \text{ fm}^2.$$

Combining the proton charge radius values with the isotope shift results, one can extract $\langle r_{Cd}^2 \rangle^{1/2}$. In fact, the CODATA-2010 recommended value

$$\langle r_{Cd}^2 \rangle^{1/2} = 2.1415(21) \text{ fm}$$

used the isotope shift results on the radii and the proton charge radius values from electron scattering.

From the electron-scattering side, all the elastic *e-d*-scattering measurements with large experimental uncertainties are not able to resolve the discrepancy between the $\langle r_{Cd}^2 \rangle^{1/2}$ values obtained from ordinary deuterium and muonic deuterium spectroscopic measurements. A reanalysis of the world *e-d* data gives (Sick and Trautmann, 1998)

$$\langle r_{Cd}^2 \rangle^{1/2} = 2.130 \pm 0.003(\text{stat}) \pm 0.009(\text{syst}) \text{ fm}.$$

With large overall uncertainty, this deuteron charge radius value from the reanalysis is consistent with both the muonic deuterium result and that from ordinary deuterium spectroscopic measurements.

A recent analysis (Hayward and Griffioen, 2020) gave a deuteron charge radius value that is consistent with muonic deuterium results with a larger statistical uncertainty as follows:

$$\langle r_{Cd}^2 \rangle^{1/2} = 2.092 \pm 0.019(\text{stat}) \text{ fm}.$$

Their analysis of the electron-proton-scattering data preferred a proton radius value that was consistent with muonic hydrogen results.

Therefore, a significantly improved $\langle r_{Cd}^2 \rangle^{1/2}$ determination from a new electron-deuteron-scattering experiment is needed to help resolve the current situation surrounding the deuteron charge radius. Figure 29 is a summary of results on the previously discussed deuteron charge radius including the CODATA-2014 value (Mohr, Newell, and Taylor, 2016), shown with the uncertainty as a band, and the CODATA-2018 recommended value (Tiesinga *et al.*, 2021). Also included is an extraction of the r_d using the isotope shift (Jentschura *et al.*, 2011) and the muonic hydrogen result of the
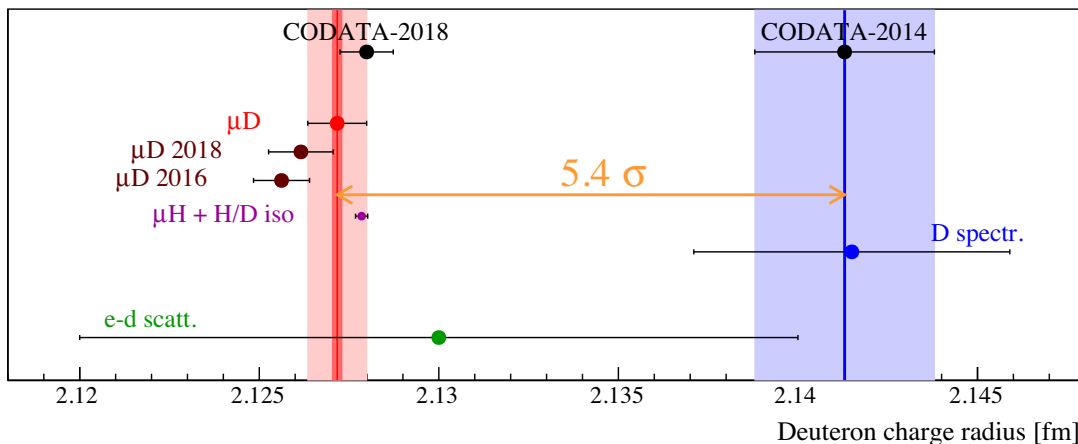

FIG. 29. Existing results on the deuteron charge radius $\langle r_{Cd}^2 \rangle^{1/2}$; see the text for details. From Randolf Pohl.

$\langle r_{Ep}^2 \rangle$ (Antognini *et al.*, 2013). The two latest extractions of the deuteron charge radius from the muonic deuterium measurement are labeled as μD 2018 (Hernandez *et al.*, 2018) and μD (Pachucki, Patkóš, and Yerokhin, 2018; Kalinowski, 2019), respectively, in Fig. 29.

The PRad Collaboration proposed a new electron-deuteron elastic-scattering experiment called DRad (Dutta, Gao, Gasparian, Higinbotham *et al.*, 2020) using an apparatus modified from that utilized for the proposed PRad-II experiment by installing a low-energy silicon-based recoil detector in a cylindrical shape inside the windowless gas flowing target to detect the recoil deuterons in coincidence with the scattered electrons. As demonstrated by the PRad experiment (Xiong *et al.*, 2019), the proposed DRad experiment will also employ a well-known QED process, Møller scattering, to control the systematic uncertainties associated with measurements of the absolute e-d cross section. The DRad experiment will aim for an overall precision that is 0.22% (relative) or better in the determination of r_d, in an essentially model-independent way.

An elastic e-d cross-section measurement (Schlimme *et al.*, 2016) was carried out at the Mainz Microtron several years ago in a momentum transfer squared range of $2.2 \times 10^{-3} - 0.28$ $(\text{GeV}/c)^2$ with the goal of extracting the deuteron charge form factor, and ultimately the deuteron charge radius. The data analysis is ongoing.

Furthermore, Carlson, Pauk, and Vanderhaeghen (2019) investigated the sensitivity of the cross section for lepton pair production off a deuteron target ($\gamma d \rightarrow e^+ e^- d$) to the deuteron charge radius. They demonstrated that for small momentum transfer this reaction is dominated by the Bethe-Heitler process, as shown in Fig. 26. They proposed measuring the deuteron at a fixed angle and scanning the momentum transfer (t) dependence of the $\gamma d \rightarrow e^+ e^- d$ cross-section ratio defined as

$$R(t, t_0) \equiv \frac{d\sigma/dt\, dM_{ll}^2(t)}{d\sigma/dt\, dM_{ll}^2(t_0)}, \qquad (82)$$
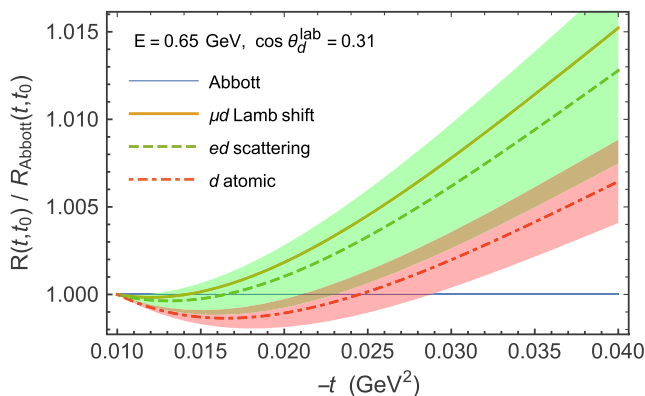

FIG. 30. Momentum transfer t dependence of the $\gamma d \rightarrow e^+ e^- d$ cross-section ratio $R(t, t_0)$, defined in Eq. (82), for reference value $t_0 = -0.01$ GeV^2, at fixed deuteron lab angle, and for beam energy 0.65 GeV. For convenience, the ratio is normalized to the result using the form factors of Abbott *et al.* (2000). The curves and associated error bands are for different extractions of the deuteron charge radius; see the text for details. From Carlson, Pauk, and Vanderhaeghen, 2019.

with $t = (p' - p)^2$ the momentum transfer, which is in a one-to-one relation with the recoil deuteron lab momentum, $|\vec{p}'|^{\text{lab}} = 2M_d\sqrt{\tau_d(1 + \tau_d)}$, with $\tau_d \equiv -t/4M_d^2$. Furthermore, in Eq. (82) M_{ll}^2 is the squared invariant mass of the dilepton pair, which at a fixed deuteron angle is a function of t, and the denominator in the ratio R is the cross section for the same deuteron-scattering angle and for a reference momentum transfer t_0. This ratio is shown in Fig. 30 for three extractions of the deuteron charge radius displayed in Fig. 29: the muonic deuterium Lamb shift value (Pohl *et al.*, 2016) (gold solid line, with uncertainty comparable to the width of the line), e-d elastic-scattering value (Sick and Trautmann, 1998) (green dashed line, with uncertainty limits indicated by the green band), and the deuterium atomic spectroscopy value (Pohl *et al.*, 2017) (red dot-dashed line, with uncertainty limits indicated by the red band). One sees in Fig. 30 that such a cross-section ratio measurement of about 0.1% relative accuracy could give a deuteron charge radius more accurate than the current e-d-scattering value (Sick and Trautmann, 1998), and sufficiently accurate to distinguish between the electronic and muonic atomic values.

IX. CONCLUSIONS

Here we reviewed the experimental progress toward the resolution of the proton charge radius puzzle over the past decade, as well as the related theoretical background and developments. In light of the latest precise determinations of the proton charge radius from ordinary atomic hydrogen spectroscopic measurements, the PRad electron-scattering experiment, and several improved reanalyses of electron-scattering data, some might be tempted to conclude that the puzzle has been resolved. We point out, however, that, while the recent experimental results prefer the CREMA value at about 0.84 fm, they are still within 3 standard deviations of the previously compiled value of about 0.88 fm. Furthermore, the most precisely determined value of r_{Ep} (Grinin *et al.*, 2020) from ordinary hydrogen spectroscopy (and also the most recent measurement) is about 2 standard deviations larger than the muonic hydrogen results. We believe more experiments, especially those with improved precision from electron scattering, and new results from muon scattering will be essential to fully resolve this puzzle. To answer a more provocative question, whether there is a difference in the proton charge radius determined from experiments involving electronic (e-p and ordinary hydrogen) versus muonic systems, significantly improved precision from lepton scattering and also measurements from ordinary hydrogen spectroscopy with precision comparable to that of Grinin *et al.* (2020) will be critical. Pushing the precision frontier has more than once proven to be the harbinger of new discoveries.

REFERENCES

Abbott, D., *et al.* (JLAB t20 Collaboration), 2000, "Phenomenology of the deuteron electromagnetic form factors," Eur. Phys. J. A **7**, 421–427.

Abrahamyan, S., *et al.* (HAPPEX and PREX Collaborations), 2012, "New Measurements of the Transverse Beam Asymmetry for Elastic Electron Scattering from Selected Nuclei," Phys. Rev. Lett. **109**, 192501.

Accardi, A., *et al.*, 2016, "Electron-Ion Collider: The next QCD frontier," Eur. Phys. J. A **52**, 268.

Adamuscin, C., S. Dubnicka, and A. Z. Dubnickova, 2012, "New value of the proton charge root mean square radius," Prog. Part. Nucl. Phys. **67**, 479–485.

Adikaram, D., *et al.* (CLAS Collaboration), 2015, "Towards a Resolution of the Proton Form Factor Problem: New Electron and Positron Scattering Data," Phys. Rev. Lett. **114**, 062003.

Afanasev, Andrei, Igor Akushevich, and N. P. Merenkov, 2002, "Nucleon Compton scattering with two space-like photons," in *Exclusive Processes at High Momentum Transfer*, edited by Paul Stoler and Anatoly Radyushkin (World Scientific, Singapore).

Ahmed, Jaseer, P. G. Blunden, and W. Melnitchouk, 2020, "Two-photon exchange from intermediate state resonances in elastic electron-proton scattering," Phys. Rev. C **102**, 045205.

Alarcón, J. M., D. W. Higinbotham, and C. Weiss, 2020, "Precise determination of the proton magnetic radius from electron scattering data," Phys. Rev. C **102**, 035203.

Alarcón, J. M., D. W. Higinbotham, C. Weiss, and Zhihong Ye, 2019, "Proton charge radius extraction from electron scattering data using dispersively improved chiral effective field theory," Phys. Rev. C **99**, 044303.

Alarcón, J. M., and C. Weiss, 2018, "Accurate nucleon electromagnetic form factors from dispersively improved chiral effective field theory," Phys. Lett. B **784**, 373–377.

Alarcón, Jose Manuel, Vadim Lensky, and Vladimir Pascalutsa, 2014, "Chiral perturbation theory of muonic hydrogen Lamb shift: Polarizability contribution," Eur. Phys. J. C **74**, 2852.

Alexandrou, C., S. Bacchio, M. Constantinou, J. Finkenrath, K. Hadjiyiannakou, K. Jansen, G. Koutsou, and A. Vaquero Aviles-Casco, 2019, "Proton and neutron electromagnetic form factors from lattice QCD," Phys. Rev. D **100**, 014509.

Alexandrou, Constantia, Kyriakos Hadjiyiannakou, Giannis Koutsou, Konstantin Ottnad, and Marcus Petschlies, 2020, "Model-independent determination of the nucleon charge radius from lattice QCD," Phys. Rev. D **101**, 114504.

Androić, D., *et al.* (G0 Collaboration), 2011, "Transverse Beam Spin Asymmetries at Backward Angles in Elastic Electron-Proton and Quasielastic Electron-Deuteron Scattering," Phys. Rev. Lett. **107**, 022501.

Androić, D., *et al.* (Q$_{weak}$ Collaboration), 2020, "Precision Measurement of the Beam-Normal Single-Spin Asymmetry in Forward-Angle Elastic Electron-Proton Scattering," Phys. Rev. Lett. **125**, 112502.

Anselmino, M., A. Mukherjee, and A. Vossen, 2020, "Transverse spin effects in hard semi-inclusive collisions," Prog. Part. Nucl. Phys. **114**, 103806.

Antognini, A., *et al.*, 2013, "Proton structure from the measurement of 2S-2P transition frequencies of muonic hydrogen," Science **339**, 417.

Antognini, Aldo, Franz Kottmann, Francois Biraben, Paul Indelicato, Francois Nez, and Randolf Pohl, 2013, "Theory of the $2S - 2P$ Lamb shift and $2S$ hyperfine splitting in muonic hydrogen," Ann. Phys. (N.Y.) **331**, 127–145.

Arbuzov, Andrej B., Eduard A. Kuraev, Nikolay P. Merenkov, and Luca Trentadue, 1998, "Hadronic cross sections in electron-positron annihilation with tagged photon," J. High Energy Phys. 12, 009.

Armstrong, David S., *et al.* (G0 Collaboration), 2007, "Transverse Beam Spin Asymmetries in Forward-Angle Elastic Electron-Proton Scattering," Phys. Rev. Lett. **99**, 092301.

Arnold, R., C. E. Carlson, and F. Gross, 1981, "Polarization transfer in elastic electron scattering from nucleons and deuterons," Phys. Rev. C **23**, 363.

Arrington, J, P. G. Blunden, and W. Melnitchouk, 2011, "Review of two-photon exchange in electron scattering," Prog. Part. Nucl. Phys. **66**, 782–833.

Arrington, J., W. Melnitchouk, and J. A. Tjon, 2007, "Global analysis of proton elastic form factor data with two-photon exchange corrections," Phys. Rev. C **76**, 035205.

Arrington, J., and I. Sick, 2015, "Evaluation of the proton charge radius from electron-proton scattering," J. Phys. Chem. Ref. Data **44**, 031204.

Ashman, J., *et al.*, 1988, "A measurement of the spin asymmetry and determination of the structure function g_1 in deep inelastic muon-proton scattering," Phys. Lett. B **206**, 364–370.

Atac, H., M. Constantinou, Z.-E. Meziani, M. Paolone, and N. Sparveris, 2021, "Charge radii of the nucleon from its flavor dependent Dirac form factors," Eur. Phys. J. A **57**, 65.

Aubert, B., *et al.* (*BABAR* Collaboration), 2004, "J/ψ production via initial state radiation in $e^+e^- \to \mu^+\mu^-\gamma$ at an e^+e^- center-of-mass energy near 10.6 GeV," Phys. Rev. D **69**, 011103.

Balaguer Rios, D., 2012, "Two-photon exchange and normal spin asymmetries in the A4 experiment," Nuovo Cimento Soc. Ital. Fis. **035N04C**, 198–202.

Barker, W. A., and F. N. Glover, 1955, "Reduction of relativistic two-particle wave equations to approximate forms. III," Phys. Rev. **99**, 317–324.

Belitsky, A. V., Xiangdong Ji, and Feng Yuan, 2004, "Quark imaging in the proton via quantum phase-space distributions," Phys. Rev. D **69**, 074014.

Belitsky, A. V., and A. V. Radyushkin, 2005, "Unraveling hadron structure with generalized parton distributions," Phys. Rep. **418**, 1–387.

Belostotski, S., N. Sagidova, and A. Vorobyev, 2019, "Proton radius reconstruction from simulated electron-proton elastic scattering cross sections at low transfer momenta," arXiv:1903.04975.

Bencivenni, G., R. De Oliveira, G. Morello, and M. Poli Lener, 2015, "The micro-resistive WELL detector: A compact spark-protected single amplification-stage MPGD," J. Instrum. **10**, P02008.

Berkeland, D. J., E. A. Hinds, and M. G. Boshier, 1995, "Precise Optical Measurement of Lamb Shifts in Atomic Hydrogen," Phys. Rev. Lett. **75**, 2470.

Bernauer, J. C., et al. (A1 Collaboration), 2010, "High-Precision Determination of the Electric and Magnetic Form Factors of the Proton," Phys. Rev. Lett. **105**, 242001.

Bernauer, J. C., et al. (A1 Collaboration), 2014, "Electric and magnetic form factors of the proton," Phys. Rev. C **90**, 015206.

Bernauer, Jan C., 2020, "The proton radius puzzle—9 years later," EPJ Web Conf. **234**, 01001.

Beyer, A., et al., 2016, "Active fiber-based retroreflector providing phase-retracing anti-parallel laser beams for precision spectroscopy," Opt. Express **24**, 17470–17485.

Beyer, Axel, et al., 2017, "The Rydberg constant and proton size from atomic hydrogen," Science **358**, 79–85.

Bezginov, N., T. Valdez, M. Horbatsch, A. Marsman, A. C. Vutha, and E. A. Hessels, 2019, "A measurement of the atomic hydrogen Lamb shift and the proton charge radius," Science **365**, 1007–1012.

Birse, M. C., and J. A. McGovern, 2012, "Proton polarisability contribution to the Lamb shift in muonic hydrogen at fourth order in chiral perturbation theory," Eur. Phys. J. A **48**, 120.

Blomqvist, K. I., et al., 1998, "The three-spectrometer facility at the Mainz microtron MAMI," Nucl. Instrum. Methods Phys. Res., Sect. A **403**, 263–301.

Bloom, Elliott D., et al., 1969, "High-Energy Inelastic e-p Scattering at 6° and 10°," Phys. Rev. Lett. **23**, 930–934.

Blunden, P. G., W. Melnitchouk, and J. A. Tjon, 2003, "Two-Photon Exchange and Elastic Electron-Proton Scattering," Phys. Rev. Lett. **91**, 142304.

Boffi, Sigfrido, and Barbara Pasquini, 2007, "Generalized parton distributions and the structure of the nucleon," Riv. Nuovo Cimento Soc. Ital. Fis. **30**, 387.

Borie, E., 2012, "Lamb shift in light muonic atoms: Revisited," Ann. Phys. (N.Y.) **327**, 733–763.

Borisyuk, Dmitry, 2010, "Proton charge and magnetic rms radii from the elastic ep scattering data," Nucl. Phys. **A843**, 59–67.

Borisyuk, Dmitry, and Alexander Kobushkin, 2009, "Perturbative QCD predictions for two-photon exchange," Phys. Rev. D **79**, 034001.

Borisyuk, Dmitry, and Alexander Kobushkin, 2015, "Two-photon exchange amplitude with πN intermediate states: Spin-1/2 and spin-3/2 channels," Phys. Rev. C **92**, 035204.

Borisyuk, Dmitry, and Alexander Kobushkin, 2020, "Reanalysis of low-energy electron-proton scattering data and proton radius," Nucl. Phys. **A1002**, 121998.

Bourzeix, S., B. de Beauvoir, F. Nez, M. D. Plimmer, F. de Tomasi, L. Julien, F. Biraben, and D. N. Stacey, 1996, "High Resolution Spectroscopy of the Hydrogen Atom: Determination of the 1S Lamb Shift," Phys. Rev. Lett. **76**, 384.

Breidenbach, Martin, Jerome I. Friedman, Henry W. Kendall, Elliott D. Bloom, D. H. Coward, H. C. DeStaebler, J. Drees, Luke W. Mo, and Richard E. Taylor, 1969, "Observed Behavior of Highly Inelastic Electron-Proton Scattering," Phys. Rev. Lett. **23**, 935–939.

Breit, G., 1929, "The effect of retardation on the interaction of two electrons," Phys. Rev. **34**, 553–573.

Breit, G., 1930, "The fine structure of HE as a test of the spin interactions of two electrons," Phys. Rev. **36**, 383–397.

Breit, G., 1932, "Dirac's equation and the spin-spin interactions of two electrons," Phys. Rev. **39**, 616–624.

Brodsky, Stanley J., Guy F. de Teramond, Hans Gunter Dosch, and Joshua Erlich, 2015, "Light-front holographic QCD and emerging confinement," Phys. Rep. **584**, 1–105.

Burkardt, M., 2000, "Impact parameter dependent parton distributions and off forward parton distributions for $\zeta 0$," Phys. Rev. D **62**, 071503; **66**, 119903(E) (2002).

Burkardt, M., 2003, "Impact parameter space interpretation for generalized parton distributions," Int. J. Mod. Phys. A **18**, 173–208.

Burkardt, M., 2006, "Hadron tomography," Int. J. Mod. Phys. A **21**, 926–929.

Caiazza, S. S., et al., 2020, "The MAGIX focal plane time projection chamber," J. Phys. Conf. Ser. **1498**, 012022.

Carlson, Carl E., 2015, "The proton radius puzzle," Prog. Part. Nucl. Phys. **82**, 59–77.

Carlson, Carl E., Vladyslav Pauk, and Marc Vanderhaeghen, 2019, "Dilepton photoproduction on a deuteron target," Phys. Lett. B **797**, 134872.

Carlson, Carl E., and Marc Vanderhaeghen, 2007, "Two-photon physics in hadronic processes," Annu. Rev. Nucl. Part. Sci. **57**, 171–204.

Carlson, Carl E., and Marc Vanderhaeghen, 2008, "Empirical Transverse Charge Densities in the Nucleon and the Nucleon-to-Δ Transition," Phys. Rev. Lett. **100**, 032004.

Carlson, Carl E., and Marc Vanderhaeghen, 2009, "Empirical transverse charge densities in the deuteron," Eur. Phys. J. A **41**, 1–5.

Carlson, Carl E., and Marc Vanderhaeghen, 2011, "Higher-order proton structure corrections to the Lamb shift in muonic hydrogen," Phys. Rev. A **84**, 020102.

Cates, G. D., C. W. de Jager, S. Riordan, and B. Wojtsekhowski, 2011, "Flavor Decomposition of the Elastic Nucleon Electromagnetic Form Factors," Phys. Rev. Lett. **106**, 252003.

Chen, Y. C., A. Afanasev, S. J. Brodsky, C. E. Carlson, and M. Vanderhaeghen, 2004, "Partonic Calculation of the Two-Photon Exchange Contribution to Elastic Electron-Proton Scattering at Large Momentum Transfer," Phys. Rev. Lett. **93**, 122301.

Christy, M. E., et al. (E94110 Collaboration), 2004, "Measurements of electron-proton elastic cross sections for $0.4 < Q^2 < 5.5$ $(\mathrm{GeV}/c)^2$," Phys. Rev. C **70**, 015206.

Chung, P. L., W. N. Polyzou, F. Coester, and B. D. Keister, 1988, "Hamiltonian light front dynamics of elastic electron deuteron scattering," Phys. Rev. C **37**, 2000–2015.

Cline, E., J. Bernauer, E. J. Downie, and R. Gilman, 2021, "MUSE: The MUon Scattering Experiment," SciPost Phys. Proc. **5**, 023.

Crawford, C., et al., 2007, "Measurement of the Proton's Electric to Magnetic Form Factor Ratio from ${}^1\vec{\mathrm{H}}(\vec{e}, e')$," Phys. Rev. Lett. **98**, 052301.

Cui, Zhu-Fang, Daniele Binosi, Craig D. Roberts, and Sebastian M. Schmidt, 2021, "Fresh extraction of the proton charge radius from electron scattering," arXiv:2102.01180.

De Rujula, A., J. M. Kaplan, and E. De Rafael, 1971, "Elastic scattering of electrons from polarized protons and inelastic electron scattering experiments," Nucl. Phys. **B35**, 365–389.

Diehl, M., 2002, "Generalized parton distributions in impact parameter space," Eur. Phys. J. C **25**, 223–232.

Diehl, M., 2003a, "Generalized parton distributions," Phys. Rep. **388**, 41–277.

Diehl, M., 2003b, "Generalized parton distributions in impact parameter space," Eur. Phys. J. C **31**, 277.

Djukanovic, D., T. Harris, G. von Hippel, P. M. Junnarkar, H. B. Meyer, D. Mohler, K. Ottnad, T. Schulz, J. Wilhelm, and H. Wittig, 2021, "Isovector electromagnetic form factors of the nucleon from lattice QCD and the proton radius puzzle," arXiv:2102.07460.

Donnelly, T. W., and A. S. Raskin, 1986, "Considerations of polarization in inclusive electron scattering from nuclei," Ann. Phys. (N.Y.) **169**, 247–351.

Dreisbach, Christian, et al. (COMPASS++/AMBER Working Group), 2019, "Measuring the proton radius in high-energy muon-proton scattering," Proc. Sci. DIS2019, 222.

Drell, S. D., and Tung-Mow Yan, 1970, "Connection of Elastic Electromagnetic Nucleon Form-Factors at Large Q^2 and Deep Inelastic Structure Functions Near Threshold," Phys. Rev. Lett. **24**, 181–185.

Dudek, J., et al., 2012, "Physics opportunities with the 12 GeV upgrade at Jefferson Lab," Eur. Phys. J. A **48**, 187.

Dutta, D., H. Gao, A. Gasparian, K. Gnanvo, D. Higinbotham, N. Liyanage, E. Pasyuk, and C. Peng, 2020, "PRad-II: A new upgraded high precision measurement of the proton charge radius," Jefferson Lab Proposal No. PR12-20-004.

Dutta, D., H. Gao, A. Gasparian, D. Higinbotham, N. Liyanage, and E. Pasyuk, 2020, "Precision deuteron charge radius measurement with elastic electron-deuteron scattering," Jefferson Lab Proposal No. PR12-20-006.

Dye, Steven, P. Matthew Gonderinger, and Gil Paz, 2016, "Elements of QED-NRQED effective field theory: NLO scattering at leading power," Phys. Rev. D **94**, 013006.

Eides, M. I., H. Grotch, and V. A. Shelyuto, 2001, "Theory of light hydrogenlike atoms," Phys. Rep. **342**, 63–261.

Ernst, F. J., R. G. Sachs, and K. C. Wali, 1960, "Electromagnetic form factors of the nucleon," Phys. Rev. **119**, 1105.

Fleurbaey, Hélène, Sandrine Galtier, Simon Thomas, Marie Bonnaud, Lucile Julien, François Biraben, François Nez, Michel Abgrall, and Jocelyne Guéna, 2018, "New Measurement of the $1S - 3S$ Transition Frequency of Hydrogen: Contribution to the Proton Charge Radius Puzzle," Phys. Rev. Lett. **120**, 183001.

Foldy, L. L., and S. A. Wouthuysen, 1950, "On the Dirac theory of spin 1/2 particles and its non-relativistic limit," Phys. Rev. **78**, 29–36.

Gao, H., 2003, "Nucleon electromagnetic form factors," Int. J. Mod. Phys. E **12**, 1–40.

Gao, H., et al., 2015, "Proton remains puzzling," Universe **3**, 18, https://www.osti.gov/biblio/1595179.

Gasparian, A., H. Gao, D. Dutta, N. Liyanage, E. Pasyuk, D. W. Higinbotham, C. Peng, K. Gnanvo, W. Xiong, and X. Bai (PRad Collaboration), 2020, "PRad-II: A new upgraded high precision measurement of the proton charge radius," arXiv:2009.10510.

Gayou, O., et al. (Jefferson Lab Hall A Collaboration), 2002, "Measurement of G_{E_p} / G_{M_p} in $\vec{e}p \to e\vec{p}$ to $Q^2 = 5.6$ GeV^2," Phys. Rev. Lett. **88**, 092301.

Gilman, R., et al. (MUSE Collaboration), 2013, "Studying the proton 'radius' puzzle with μp elastic scattering," arXiv:1303.2160.

Gilman, R., et al. (MUSE Collaboration), 2017, "Technical design report for the Paul Scherrer Institute Experiment R-12-01.1: Studying the proton 'radius' puzzle with μp elastic scattering," arXiv:1709.09753.

Goeke, K., Maxim V. Polyakov, and M. Vanderhaeghen, 2001, "Hard exclusive reactions and the structure of hadrons," Prog. Part. Nucl. Phys. **47**, 401–515.

Gorchtein, M., Pierre A. M. Guichon, and M. Vanderhaeghen, 2004, "Beam normal spin asymmetry in elastic lepton-nucleon scattering," Nucl. Phys. **A741**, 234–248.

Gou, B., et al., 2020, "Study of Two-Photon Exchange via the Beam Transverse Single Spin Asymmetry in Electron-Proton Elastic Scattering at Forward Angles over a Wide Energy Range," Phys. Rev. Lett. **124**, 122003.

Gourdin, M., 1963, "Deuteron electromagnetic form factors," Nuovo Cimento **28**, 533.

Graczyk, Krzysztof M., and Cezary Juszczak, 2014, "Proton radius from Bayesian inference," Phys. Rev. C **90**, 054334.

Gramolin, Alexander V., and Rebecca L. Russell, 2021, "Transverse charge density and the radius of the proton," arXiv:2102.13022.

Grieser, S., D. Bonaventura, P. Brand, C. Hargens, B. Hetz, L. Leßmann, C. Westphälinger, and A. Khoukaz, 2018, "A cryogenic supersonic jet target for electron scattering experiments at MAGIX@MESA and MAMI," Nucl. Instrum. Methods Phys. Res., Sect. A **906**, 120–126.

Griffioen, K., C. Carlson, and S. Maddox, 2016, "Consistency of electron scattering data with a small proton radius," Phys. Rev. C **93**, 065207.

Grinin, Alexey, Arthur Matveev, Dylan C. Yost, Lothar Maisenbacher, Vitaly Wirthl, Randolf Pohl, Theodor W. Hänsch, and Thomas Udem, 2020, "Two-photon frequency comb spectroscopy of atomic hydrogen," Science **370**, 1061–1066.

Gryniuk, Oleksii, Sylvester Joosten, Zein-Eddine Meziani, and Marc Vanderhaeghen, 2020, "Υ photoproduction on the proton at the Electron-Ion Collider," Phys. Rev. D **102**, 014016.

Gryniuk, Oleksii, and Marc Vanderhaeghen, 2016, "Accessing the real part of the forward J/ψ-p scattering amplitude from J/ψ photoproduction on protons around threshold," Phys. Rev. D **94**, 074001.

Guichon, Pierre A. M., and Marc Vanderhaeghen, 2003, "How to Reconcile the Rosenbluth and the Polarization Transfer Method in the Measurement of the Proton Form Factors," Phys. Rev. Lett. **91**, 142303.

Guidal, Michel, Hervé Moutarde, and Marc Vanderhaeghen, 2013, "Generalized parton distributions in the valence region from deeply virtual Compton scattering," Rep. Prog. Phys. **76**, 066202.

Gülker, P., et al., 2019, "Development of large area focal plane detectors for MAGIX," arXiv:1906.05900.

Guo, Yuxun, Xiangdong Ji, and Kyle Shiells, 2021, "Novel twist-three transverse-spin sum rule for the proton and related generalized parton distributions," Nucl. Phys. **B969**, 115440.

Guttmann, Julia, Nikolai Kivel, Mehdi Meziane, and Marc Vanderhaeghen, 2011, "Determination of two-photon exchange amplitudes from elastic electron-proton scattering data," Eur. Phys. J. A **47**, 77.

Hafidi, K., X. Qian, N. Sparveris, Z.-E. Meziani, and Z. W. Zhao, 2012, "Near threshold electroproduction of J/Ψ at 11 GeV," Jefferson Lab Proposal No. E12-12-006.

Hagelstein, Franziska, 2017, "Exciting nucleons in Compton scattering and hydrogen-like atoms," arXiv:1710.00874.

Hagelstein, Franziska, Rory Miskimen, and Vladimir Pascalutsa, 2016, "Nucleon polarizabilities: From Compton scattering to hydrogen atom," Prog. Part. Nucl. Phys. **88**, 29–97.

Hagelstein, Franziska, and Vladimir Pascalutsa, 2019, "Lower bound on the proton charge radius from electron scattering data," Phys. Lett. B **797**, 134825.

Hagley, E. W., and F. M. Pipkin, 1994, "Separated Oscillatory Field Measurement of Hydrogen $2S_{1/2}$-$2P_{3/2}$ Fine Structure Interval," Phys. Rev. Lett. **72**, 1172.

Hand, L. N., D. G. Miller, and Richard Wilson, 1963, "Electric and magnetic form factors of the nucleon," Rev. Mod. Phys. **35**, 335.

Hasan, Nesreen, Jeremy Green, Stefan Meinel, Michael Engelhardt, Stefan Krieg, John Negele, Andrew Pochinsky, and Sergey Syritsyn, 2018, "Computing the nucleon charge and axial radii directly at $Q^2 = 0$ in lattice QCD," Phys. Rev. D **97**, 034504.

Hasell, D., R. G. Milner, R. P. Redwine, R. Alarcon, H. Gao, M. Kohl, and J. R. Calarco, 2011, "Spin-dependent electron scattering from polarized protons and deuterons with the BLAST experiment at MIT-Bates," Annu. Rev. Nucl. Part. Sci. **61**, 409.

Hatta, Yoshitaka, and Di-Lun Yang, 2018, "Holographic J/ψ production near threshold and the proton mass problem," Phys. Rev. D **98**, 074003.

Hayward, Timothy B., and Keith A. Griffioen, 2020, "Evaluation of low-Q^2 fits to ep and ed elastic scattering data," Nucl. Phys. **A999**, 121767.

Henderson, B. S., et al. (OLYMPUS Collaboration), 2017, "Hard Two-Photon Contribution to Elastic Lepton-Proton Scattering: Determined by the OLYMPUS Experiment," Phys. Rev. Lett. **118**, 092501.

Hernandez, O. J., A. Ekström, N. Nevo Dinur, C. Ji, S. Bacca, and N. Barnea, 2018, "The deuteron-radius puzzle is alive: A new analysis of nuclear structure uncertainties," Phys. Lett. B **778**, 377–383.

Higinbotham, Douglas W., Al Amin Kabir, Vincent Lin, David Meekins, Blaine Norum, and Brad Sawatzky, 2016, "Proton radius from electron scattering data," Phys. Rev. C **93**, 055207.

Hill, Richard J., Gabriel Lee, Gil Paz, and Mikhail P. Solon, 2013, "NRQED Lagrangian at order $1/M^4$," Phys. Rev. D **87**, 053017.

Hill, Richard J., and Gil Paz, 2010, "Model-independent extraction of the proton charge radius from electron scattering," Phys. Rev. D **82**, 113005.

Hill, Richard J., and Gil Paz, 2011, "Model Independent Analysis of Proton Structure for Hydrogenic Bound States," Phys. Rev. Lett. **107**, 160402.

Hoferichter, M., B. Kubis, J. Ruiz de Elvira, H. W. Hammer, and U. G. Meißner, 2016, "On the $\pi\pi$ continuum in the nucleon form factors and the proton radius puzzle," Eur. Phys. J. A **52**, 331.

Hoferichter, Martin, Jacobo Ruiz de Elvira, Bastian Kubis, and Ulf-G. Meißner, 2016, "Roy-Steiner-equation analysis of pion-nucleon scattering," Phys. Rep. **625**, 1–88.

Hofstadter, R., and R. W. McAllister, 1955, "Electron scattering from the proton," Phys. Rev. **98**, 217.

Horbatsch, M., and E. A. Hessels, 2016a, "Evaluation of the strength of electron-proton scattering data for determining the proton charge radius," Phys. Rev. C **93**, 015204.

Horbatsch, M., and E. A. Hessels, 2016b, "Tabulation of the bound-state energies of atomic hydrogen," Phys. Rev. A **93**, 022513.

Horbatsch, Marko, 2020, "Properties of the Sachs electric form factor of the proton on the basis of recent e-p scattering experiments and hydrogen spectroscopy," Phys. Lett. B **804**, 135373.

Horbatsch, Marko, Eric A. Hessels, and Antonio Pineda, 2017, "Proton radius from electron-proton scattering and chiral perturbation theory," Phys. Rev. C **95**, 035203.

Hoyer, Paul, 2009, "Bound states at lowest order in hbar," arXiv:0909.3045.

Huber, A., Th. Udem, B. Gross, J. Reichert, M. Kourogi, K. Pachucki, M. Weitz, and T. W. Hänsch, 1998, "Hydrogen-Deuterium $1S - 2S$ Isotope Shift and the Structure of the Deuteron," Phys. Rev. Lett. **80**, 468–471.

Hug, Florian, Kurt Aulenbacher, Simon Friederich, Philipp Heil, Robert Heine, Ruth Kempf, Christoph Matejcek, and Daniel Simon, 2020, "Status of the MESA ERL project," in *Proceedings of the 63rd ICFA Advanced Beam Dynamics Workshop on Energy Recovery Linacs, Berlin, 2019*, https://doi.org/10.18429/JACoW-ERL2019-MOCOXBS02.

Jaffe, Robert L., 2021, "Ambiguities in the definition of local spatial densities in light hadrons," Phys. Rev. D **103**, 016017.

Jang, Yong-Chull, Rajan Gupta, Huey-Wen Lin, Boram Yoon, and Tanmoy Bhattacharya, 2020, "Nucleon electromagnetic form factors in the continuum limit from $(2 + 1 + 1)$–flavor lattice QCD," Phys. Rev. D **101**, 014507.

Jankus, V. Z., 1956, "Calculation of electron-deuteron scattering cross sections," Phys. Rev. **102**, 1586–1591.

Jarvinen, M., 2005, "The hydrogen atom in relativistic motion," Phys. Rev. D **71**, 085006.

Jentschura, U. D., 2011, "Lamb shift in muonic hydrogen—I. Verification and update of theoretical predictions," Ann. Phys. (N.Y.) **326**, 500–515.

Jentschura, U. D., A. Matveev, C. G. Parthey, J. Alnis, R. Pohl, Th. Udem, N. Kolachevsky, and T. W. Hänsch, 2011, "Hydrogen-deuterium isotope shift: From the $1S - 2S$-transition frequency to the proton-deuteron charge-radius difference," Phys. Rev. A **83**, 042505.

Ji, X., 2003, "Viewing the Proton through 'Color' Filters," Phys. Rev. Lett. **91**, 062001.

Ji, Xiangdong, 1995, "QCD Analysis of the Mass Structure of the Nucleon," Phys. Rev. Lett. **74**, 1071–1074.

Ji, Xiangdong, Feng Yuan, and Yong Zhao, 2020, "Proton spin after 30 years: What we know and what we don't," arXiv:2009.01291.

Ji, Xiang-Dong, 1997a, "Deeply virtual Compton scattering," Phys. Rev. D **55**, 7114–7125.

Ji, Xiang-Dong, 1997b, "Gauge-Invariant Decomposition of Nucleon Spin," Phys. Rev. Lett. **78**, 610–613.

Jones, M. K., et al. (Jefferson Lab Hall A Collaboration), 2000, "G_{E_p} / G_{M_p} Ratio by Polarization Transfer in Polarized $\vec{e}p \to e\vec{p}$," Phys. Rev. Lett. **84**, 1398–1402.

Kalinowski, Marcin, 2019, "Deuteron charge radius from the Lamb-shift measurement in muonic deuterium," Phys. Rev. A **99**, 030501.

Karr, J. P., D. Marchand, and E. Voutier, 2020, "The proton size," Nat. Rev. Phys. **2**, 601–614.

Karshenboim, S. G., E. Korzinin, V. G. Yu Ivanov, and V. A. Shelyuto, 2010, "Contribution of light-by-light scattering to energy levels of light muonic atoms," JETP Lett. **92**, 8–14.

Karshenboim, Savely G., Vladimir G. Ivanov, and Evgeny Yu. Korzinin, 2012, "Relativistic recoil corrections to the electron-vacuum-polarization contribution in light muonic atoms," Phys. Rev. A **85**, 032509.

Kato, K., T. D. G. Skinner, and E. A. Hessels, 2018, "Ultrahigh-Precision Measurement of the $n = 2$ Triplet P Fine Structure of Atomic Helium Using Frequency-Offset Separated Oscillatory Fields," Phys. Rev. Lett. **121**, 143002.

Kelly, J. J., 2004, "Simple parametrization of nucleon form factors," Phys. Rev. C **70**, 068202.

Kharzeev, D., H. Satz, A. Syamtomov, and G. Zinovjev, 1999, "J/ψ photoproduction and the gluon structure of the nucleon," Eur. Phys. J. C **9**, 459–462.

Kivel, N., and M. Vanderhaeghen, 2013, "Two-photon exchange corrections to elastic electron-proton scattering at large momentum transfer within the SCET approach," J. High Energy Phys. 04 029.

Kivel, Nikolai, and Marc Vanderhaeghen, 2009, "Two-Photon Exchange in Elastic Electron-Proton Scattering: QCD Factorization Approach," Phys. Rev. Lett. 103, 092004.

Kogut, J. B., and D. Soper, 1970, "Quantum electrodynamics in the infinite-momentum frame," Phys. Rev. D 1, 2901.

Kraus, E., K. E. Mesick, A. White, R. Gilman, and S. Strauch, 2014, "Polynomial fits and the proton radius puzzle," Phys. Rev. C 90, 045206.

Kuhn, S., J.-P. Chen, and E. Leader, 2009, "Spin structure of the nucleon—Status and recent results," Prog. Part. Nucl. Phys. 63, 1–50.

Kumar, K. S., Sonny Mantry, W. J. Marciano, and P. A. Souder, 2013, "Low energy measurements of the weak mixing angle," Annu. Rev. Nucl. Part. Sci. 63, 237–267.

Kumericki, Kresimir, Simonetta Liuti, and Herve Moutarde, 2016, "GPD phenomenology and DVCS fitting: Entering the high-precision era," Eur. Phys. J. A 52, 157.

Larin, I., et al. (PrimEx Collaboration), 2011, "New Measurement of the π^0 Radiative Decay Width," Phys. Rev. Lett. 106, 162303.

Larin, I., et al. (PrimEx Collaboration), 2020, "Precision measurement of the neutral pion lifetime," Science 368, 506–509.

Lee, Gabriel, John R. Arrington, and Richard J. Hill, 2015, "Extraction of the proton radius from electron-proton scattering data," Phys. Rev. D 92, 013013.

Lensky, Vadim, Franziska Hagelstein, Vladimir Pascalutsa, and Marc Vanderhaeghen, 2018, "Sum rules across the unpolarized Compton processes involving generalized polarizabilities and moments of nucleon structure functions," Phys. Rev. D 97, 074012.

Lin, Yong-Hui, Hans-Werner Hammer, and Ulf-G Meißner, 2021, "High-precision determination of the electric and magnetic radius of the proton," Phys. Lett. B 816, 136254.

Lorcé, C., 2009, "Electromagnetic properties for arbitrary spin particles: Natural electromagnetic moments from light-cone arguments," Phys. Rev. D 79, 113011.

Lorcé, C., 2018, "On the hadron mass decomposition," Eur. Phys. J. C 78, 120.

Lorcé, C., and B. Pasquini, 2011, "Quark Wigner distributions and orbital angular momentum," Phys. Rev. D 84, 014015.

Lorcé, C., B. Pasquini, and M. Vanderhaeghen, 2011, "Unified framework for generalized and transverse-momentum dependent parton distributions within a 3Q light-cone picture of the nucleon," J. High Energy Phys. 05 041.

Lorcé, C., B. Pasquini, X. Xiong, and F. Yuan, 2012, "The quark orbital angular momentum from Wigner distributions and light-cone wave functions," Phys. Rev. D 85, 114006.

Lorcé, Cédric, 2020, "Charge Distributions of Moving Nucleons," Phys. Rev. Lett. 125, 232002.

Lorenz, I. T., H.-W. Hammer, and Ulf-G. Meissner, 2012, "The size of the proton: Closing in on the radius puzzle," Eur. Phys. J. A 48, 151–156.

Lorenz, I. T., Ulf-G. Meißner, H.-W. Hammer, and Y.-B. Dong, 2015, "Theoretical constraints and systematic effects in the determination of the proton form factors," Phys. Rev. D 91, 014023.

Lorenz, I. T., and Ulf-G. Meissner, 2014, "Reduction of the proton radius discrepancy by 3σ," Phys. Lett. B 737, 57–59.

Maas, F. E., et al., 2005, "Measurement of the Transverse Beam Spin Asymmetry in Elastic Electron Proton Scattering and the Inelastic Contribution to the Imaginary Part of the Two-Photon Exchange Amplitude," Phys. Rev. Lett. 94, 082001.

Matveev, Arthur, et al., 2013, "Precision Measurement of the Hydrogen $1S - 2S$ Frequency via a 920-km Fiber Link," Phys. Rev. Lett. 110, 230801.

Maximon, L. C., 1969, "Comments on radiative corrections," Rev. Mod. Phys. 41, 193.

McAllister, R. W., and R. Hofstadter, 1956, "Elastic scattering of 188-MeV electrons from the proton and the alpha particle," Phys. Rev. 102, 851.

Meissner, S., A. Metz, M. Schlegel, and K. Goeke, 2008, "Generalized parton correlation functions for a spin-0 hadron," J. High Energy Phys. 08, 038.

Meissner, S., A. Metz, and M. Schlegel, 2009, "Generalized parton correlation functions for a spin-1/2 hadron," J. High Energy Phys. 08, 056.

Melnikov, K., and T. van Ritbergen, 2000, "Three-Loop Slope of the Dirac Form Factor of the 1S Lamb Shift in Hydrogen," Phys. Rev. Lett. 84, 1673.

Metz, Andreas, Barbara Pasquini, and Simone Rodini, 2020, "Revisiting the proton mass decomposition," Phys. Rev. D 102, 114042.

Meziane, M., et al. (GEp2γ Collaboration), 2011, "Search for Effects beyond the Born Approximation in Polarization Transfer Observables in $\vec{e}p$ Elastic Scattering," Phys. Rev. Lett. 106, 132501.

Mihovilovič, M., et al., 2017, "First measurement of proton's charge form factor at very low Q^2 with initial state radiation," Phys. Lett. B 771, 194–198.

Mihovilovič, M., et al., 2021, "The proton charge radius extracted from the initial-state radiation experiment at MAMI," Eur. Phys. J. A 57, 107.

Miller, G. A., 2019, "Defining the proton radius: A unified treatment," Phys. Rev. C 99, 035202.

Miller, Gerald A., 2007, "Charge Density of the Neutron," Phys. Rev. Lett. 99, 112001.

Mo, L. W., and Y.-S. Tsai, 1969, "Radiative corrections to elastic and inelastic ep and μp scattering," Rev. Mod. Phys. 41, 205.

Mohr, P. J., B. N. Taylor, and D. B. Newell, 2008, "CODATA recommended values of the fundamental physical constants: 2006," Rev. Mod. Phys. 80, 633–730.

Mohr, P. J., B. N. Taylor, and D. B. Newell, 2012, "CODATA recommended values of the fundamental physical constants: 2010," Rev. Mod. Phys. 84, 1527.

Mohr, Peter J., David B. Newell, and Barry N. Taylor, 2016, "CODATA recommended values of the fundamental physical constants: 2014," J. Phys. Chem. Ref. Data 45, 043102.

Müller, Dieter, D. Robaschik, B. Geyer, F.-M. Dittes, and J. Hořejši, 1994, "Wave functions, evolution equations and evolution kernels from light ray operators of QCD," Fortschr. Phys. 42, 101–141.

Murphy, J. J., Y. M. Shin, and D. M. Skopik, 1974a, "Erratum: Proton form factor from 0.15 to 0.79 fm^{-2}," Phys. Rev. C 10, 2111–2111.

Murphy, J. J., Y. M. Shin, and D. M. Skopik, 1974b, "Proton form factor from 0.15 to 0.79 fm^{-2}," Phys. Rev. C 9, 2125–2129; 10, 2111(E) (1974).

Pachucki, Krzysztof, 1996, "Theory of the Lamb shift in muonic hydrogen," Phys. Rev. A 53, 2092–2100.

Pachucki, Krzysztof, 1999, "Proton structure effects in muonic hydrogen," Phys. Rev. A 60, 3593–3598.

Pachucki, Krzysztof, Vojtěch Patkóš, and Vladimir A. Yerokhin, 2018, "Three-photon-exchange nuclear structure correction in hydrogenic systems," Phys. Rev. A 97, 062511.

Paolone, M., et al. (E03-104 Collaboration), 2010, "Polarization Transfer in the ^{4}He$(\vec{e}, e'\vec{p})^3$H Reaction at $Q^2 = 0.8$ and 1.3 (GeV/c)^2," Phys. Rev. Lett. 105, 072001.

Parthey, Christian G., Arthur Matveev, Janis Alnis, Randolf Pohl, Thomas Udem, Ulrich D. Jentschura, Nikolai Kolachevsky, and Theodor W. Hänsch, 2010, "Precision Measurement of the Hydrogen-Deuterium $1S - 2S$ Isotope Shift," Phys. Rev. Lett. **104**, 233001.

Parthey, Christian G., et al., 2011, "Improved Measurement of the Hydrogen $1S - 2S$ Transition Frequency," Phys. Rev. Lett. **107**, 203001.

Pasquini, B., and M. Vanderhaeghen, 2004, "Resonance estimates for single spin asymmetries in elastic electron-nucleon scattering," Phys. Rev. C **70**, 045206.

Pauk, Vladyslav, and Marc Vanderhaeghen, 2015, "Lepton Universality Test in the Photoproduction of $e^- e^+$ versus $\mu^- \mu^+$ Pairs on a Proton Target," Phys. Rev. Lett. **115**, 221804.

Perdrisat, C. F., V. Punjabi, and M. Vanderhaeghen, 2007, "Nucleon electromagnetic form factors," Prog. Part. Nucl. Phys. **59**, 694–764.

Peset, Clara, and Antonio Pineda, 2014, "The two-photon exchange contribution to muonic hydrogen from chiral perturbation theory," Nucl. Phys. **B887**, 69–111.

Pierce, J., et al., 2021, "The PRad windowless gas flow target," arXiv:2103.01749.

Pineda, Antonio, 2003, "Leading chiral logs to the hyperfine splitting of the hydrogen and muonic hydrogen," Phys. Rev. C **67**, 025201.

Pohl, R., et al., 2010, "The size of the proton," Nature (London) **466**, 213–216.

Pohl, Randolf, Ronald Gilman, Gerald A. Miller, and Krzysztof Pachucki, 2013, "Muonic hydrogen and the proton radius puzzle," Annu. Rev. Nucl. Part. Sci. **63**, 175–204.

Pohl, Randolf, et al., 2016, "Laser spectroscopy of muonic deuterium," Science **353**, 669–673.

Pohl, Randolf, et al., 2017, "Deuteron charge radius and Rydberg constant from spectroscopy data in atomic deuterium," Metrologia **54**, L1–L10.

Puckett, A. J. R., et al., 2010, "Recoil Polarization Measurements of the Proton Electromagnetic Form Factor Ratio to $Q^2 = 8.5$ GeV^2," Phys. Rev. Lett. **104**, 242301.

Punjabi, V., et al., 2005, "Proton elastic form-factor ratios to $Q^2 = 3.5 - $GeV^2 by polarization transfer," Phys. Rev. C **71**, 055202; **71**, 069902(E) (2005).

Rachek, I. A., et al., 2015, "Measurement of the Two-Photon Exchange Contribution to the Elastic $e^\pm p$ Scattering Cross Sections at the VEPP-3 Storage Ring," Phys. Rev. Lett. **114**, 062005.

Radyushkin, A. V., 1996, "Scaling limit of deeply virtual Compton scattering," Phys. Lett. B **380**, 417–425.

Ramsey, Norman F., 1949, "A new molecular beam resonance method," Phys. Rev. **76**, 996–996.

Rimal, D., et al. (CLAS Collaboration), 2017, "Measurement of two-photon exchange effect by comparing elastic $e^\pm p$ cross sections," Phys. Rev. C **95**, 065201.

Rinehimer, Jared, A., and Gerald A. Miller, 2009, "Connecting the Breit frame to the infinite momentum light front frame: How G_E turns into F_1," Phys. Rev. C **80**, 015201.

Riordan, Michael, 1992, "The discovery of quarks," Science **256**, 1287.

Ron, G., et al., 2011, "Low-Q^2 measurements of the proton form factor ratio $\mu_p GE/GM$," Phys. Rev. C **84**, 055204.

Rosenbluth, M. N., 1950, "High energy elastic scattering of electrons on protons," Phys. Rev. **79**, 615.

Sachs, R. G., 1962, "High-energy behavior of nucleon electromagnetic form factors," Phys. Rev. **126**, 2256.

Sato, Yutaro, 2017, "Muon $g - 2$/EDM experiment at J-PARC," Proc. Sci. KMI2017, 006.

Schlimme, B. S., et al., 2016, "Deuteron form factor measurements at low momentum transfers," EPJ Web Conf. **113**, 04017.

Schlimme, B. S., et al., 2021, "Operation and characterization of a windowless gas jet target in high-intensity electron beams," arXiv:2104.13503.

Schwob, C., L. Jozefowski, B. de Beauvoir, L. Hilico, F. Nez, L. Julien, F. Biraben, O. Acef, J.-J. Zondy, and A. Clairon, 1999, "Optical Frequency Measurement of the $2S - 12D$ Transitions in Hydrogen and Deuterium: Rydberg Constant and Lamb Shift Determinations," Phys. Rev. Lett. **82**, 4960.

Shifman, M. A., A. I. Vainshtein, and V. I. Zakharov, 1978, "Remarks on Higgs-boson interactions with nucleons," Phys. Lett. B **78**, 443–446.

Shintani, Eigo, Ken-Ichi Ishikawa, Yoshinobu Kuramashi, Shoichi Sasaki, and Takeshi Yamazaki, 2019, "Nucleon form factors and root-mean-square radii on a $(10.8$ fm$)^4$ lattice at the physical point," Phys. Rev. D **99**, 014510; **102**, 019902(E) (2020).

Sick, Ingo, 2018, "Proton charge radius from electron scattering," Atoms **6**, 2.

Sick, Ingo, and Dirk Trautmann, 1998, "On the rms radius of the deuteron," Nucl. Phys. **A637**, 559–575.

Sick, Ingo, and Dirk Trautmann, 2017, "Reexamination of proton rms radii from low-q power expansions," Phys. Rev. C **95**, 012501.

Simon, G. G., Ch. Schmitt, F. Borkowski, and V. H. Walther, 1980, "Absolute electron-proton cross sections at low momentum transfer measured with a high pressure gas target system," Nucl. Phys. **A333**, 381–391.

Sokhoyan, Vahe, 2020 (private communication).

Soper, D., 1977, "Parton model and the Bethe-Salpeter wave function," Phys. Rev. D **15**, 1141–1149.

Suda, T., 2018, "Elastic electron scattering off proton using 60 MeV electron linac of Tohoku University" (unpublished).

Sufian, Raza Sabbir, Guy F. de Téramond, Stanley J. Brodsky, Alexandre Deur, and Hans Günter Dosch, 2017, "Analysis of nucleon electromagnetic form factors from light-front holographic QCD: The spacelike region," Phys. Rev. D **95**, 014011.

Tiesinga, Eite, Peter J. Mohr, David B. Newell, and Barry N. Taylor, 2021, "CODATA recommended values of the fundamental physical constants: 2018," Rev. Mod. Phys. **93**, 025010.

Tomalak, O., B. Pasquini, and M. Vanderhaeghen, 2017a, "Two-photon exchange corrections to elastic e^--proton scattering: Full dispersive treatment of πN states at low momentum transfers," Phys. Rev. D **95**, 096001.

Tomalak, Oleksandr, Barbara Pasquini, and Marc Vanderhaeghen, 2017b, "Two-photon exchange contribution to elastic e^--proton scattering: Full dispersive treatment of πN states and comparison with data," Phys. Rev. D **96**, 096001.

van Wijngaarden, A., F. Holuj, and G. W. Drake, 1998, "Lamb-shift measurement in hydrogen by the anisotropy method," Can. J. Phys. **76**, 95.

Volotka, A. V., V. M. Shabaev, G. Plunien, and G. Soff, 2005, "Zemach and magnetic radius of the proton from the hyperfine splitting in hydrogen," Eur. Phys. J. D **33**, 23–27.

Vorobyev, A. A., 2019, "Precision measurement of the proton charge radius in electron proton scattering," Phys. Part. Nucl. Lett. **16**, 524–529.

Vorobyev, A. A., and A. Denig, 2017, "proposal: High precision measurement of the ep elastic cross section at small Q^2," MAMI A2 report.

Vutha, A. C., and E. A. Hessels, 2015, "Frequency-offset separated oscillatory fields," Phys. Rev. A **92**, 052504.

Weis, M., 2003, "Elektroproduktion neutraler pionen und entwicklung eines steuerungssystems für die drei-spektrometer-anlage am Mainzer Mikrotron," Ph.D. thesis (Johannes Gutenberg-Universitaet Mainz).

Weitz, M., A. Huber, F. Schmidt-Kaler, D. Leibfried, and T. W. Hänsch, 1994, "Precision Measurement of the Hydrogen and Deuterium $1S$ Ground State Lamb Shift," Phys. Rev. Lett. **72**, 328.

Wells, S., et al. (SAMPLE Collaboration), 2001, "Measurement of the vector analyzing power in elastic electron proton scattering as a probe of double photon exchange amplitudes," Phys. Rev. C **63**, 064001.

Xiong, W., et al., 2019, "A small proton charge radius from an electron-proton scattering experiment," Nature (London) **575**, 147–150.

Xiong, Weizhi, 2020, "A high precision measurement of the proton charge radius at JLab," Ph.D. thesis (Duke University).

Yan, X., D. W. Higinbotham, D. Dutta, H. Gao, A. Gasparian, M. A. Khandaker, N. Liyanage, E. Pasyuk, C. Peng, and W. Xiong, 2018, "Robust extraction of the proton charge radius from electron-proton scattering data," Phys. Rev. C **98**, 025204.

Ye, Zhihong, John Arrington, Richard J. Hill, and Gabriel Lee, 2018, "Proton and neutron electromagnetic form factors and uncertainties," Phys. Lett. B **777**, 8–15.

Zhan, X., et al., 2011, "High-precision measurement of the proton elastic form factor ratio G_E/G_M at low Q^2," Phys. Lett. B **705**, 59–64.

Zhang, Y. W., et al., 2015, "Measurement of the Target-Normal Single-Spin Asymmetry in Quasielastic Scattering from the Reaction ${}^3\text{He}^{\uparrow}(e, e')$," Phys. Rev. Lett. **115**, 172502.

Zhou, Jingyi, et al., 2021, "Advanced extraction of the deuteron charge radius from electron-deuteron scattering data," Phys. Rev. C **103**, 024002.

Zhou, Shuang, P. Giulani, J. Piekarewicz, Anirban Bhattacharya, and Debdeep Pati, 2019, "Reexamining the proton-radius problem using constrained Gaussian processes," Phys. Rev. C **99**, 055202.

Zyla, P. A., et al. (Particle Data Group), 2020, "Review of particle physics," Prog. Theor. Exp. Phys. 083C01.